EFFECT OF HEAT TREATMENT ON MEMBRANE ELECTRODE ASSEMBLY PERFORMANCE

By

BAMATO JONATHAN ITOTA

Thesis submitted in fulfillment of the requirements for the degree

Master of Engineering in Chemical Engineering

In the Faculty of Engineering and the Built Environment

At the

Cape Peninsula University of Technology

Bellville Campus
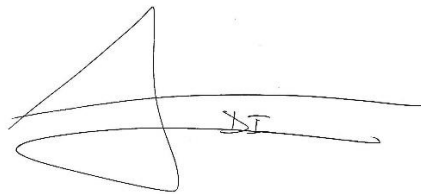
November 2021

Supervisors:

Dr. Mahabubur Chowdhury (CPUT) & Dr. Jessica Chamier (UCT)

DECLARATION

I, Bamato Jonathan Itota, declare that the contents of this thesis represent my own unaided work, and that the thesis has not previously been submitted for academic examination towards any qualification. Furthermore, it represents my own opinions and not necessarily those of the Cape Peninsula University of Technology.

Signature:

Bamato Jonathan Itota

Date: 01 April 2021

Abstract

Polymer electrolyte membrane fuel cells (PMFCs) are promising power converters which have received attention in microelectronics, automotive and stationary applications. The heart of a PEMFC is its catalyst layers where hydrogen oxidation and oxygen reduction occur. The constitutive materials of the catalyst layers are the platinum catalyst dispersed on a carbon support and a proton conducting material (the ionomer). These solid materials interact and form active sites where electrochemical reactions take place. The interactions between the supported catalyst and the ionomer are initiated during the catalyst slurry preparation. The catalyst slurries are coated onto membranes to form membrane electrode assemblies (MEAs). The current catalyst slurry preparation method produces MEAs with benchmark performance yet requires a thermal treatment step which is time and energy consuming. Therefore, this study aimed to optimize the manufacturing time by determining the impact of thermal drying on the ionomer-supported catalyst interactions. Herein, the catalyst slurry preparation methods were varied as well as the catalyst support (Graphitized Vulcan and Vulcan) to determine how these variables impact the interactions and the resulting performance.

Four methods of catalyst slurry preparation were used: thermal drying, no drying, freeze-drying and air-spray drying. The freeze-drying method isolated the impact of heat during catalyst slurry preparation and the air-spray drying method aimed to decrease the process time. Physical characterizations such as Raman spectroscopy was used to study the surface properties of the supported catalysts, scanning electron microscopy to determine the thicknesses of the catalyst layers, mercury intrusion porosimetry and atomic force microscopy to study the pore structure and the aggregates in the catalyst layers, respectively. MEA performance tests were done in-situ and consisted of current-potential polarization curve, cyclic voltammetry to calculate the electrochemical surface area, and electrochemical impedance spectroscopy to determine the charge transfer resistance. Accelerated stress tests to investigate carbon corrosion were conducted ex-situ in a half-MEA cell.

The mechanism of ionomer attachment onto the supported catalyst was independent on the catalyst slurry preparation method and highly depended on the surface properties of the catalyst support. The hydrophilic side-chain of the ionomer showed preference to the platinum catalyst and the less hydrophobic support (Vulcan) and the hydrophobic backbone of the ionomer interacted with the more hydrophobic support (graphitized Vulcan (GV)). The pore structure of the catalyst layers and the ionomer distribution varied with the catalyst slurry preparation methods. Slow-drying rate methods such as thermal drying and freeze-drying

methods produced thin GV40 (40% of Pt supported on graphitized Vulcan) catalyst layers with large intrusion volume pores and optimal ionomer distribution which improved the mass transport properties and increased ionomer-supported catalyst interfaces, respectively. These resulted in benchmark performance, larger electrochemical surface areas and lower charge transfer resistances. While the no drying and the air-spray drying methods produced thick GV40 catalyst layers with small ionomer-supported catalyst interfaces which decreased the protonic connectivity in the catalyst layers. These GV40 MEAs showed high potential losses, low electrochemical surface areas and high charge transfer resistances.

Similar catalyst layer structure and electrochemical properties were observed between V40 (40% of Pt supported on Vulcan) MEAs prepared by the thermal drying and no drying methods, this was likely due to the surface properties of Vulcan which facilitated the interactions with the ionomer to form large interfaces. However, the air spray drying method resulted in small ionomer-supported catalyst interfaces which lowered the performance of the MEAs.

It was concluded that optimal GV40 catalyst layer structure and performance were functions of the drying rate (and not heat) during the catalyst slurry preparation. And no drying step was required during V40 catalyst slurry preparation to achieve similar performance

Acknowledgements

Now let me wish it like Aime Cesaire:

" Maintenant vas mon oeuvre, vas ou le destin te mene"

Contents

List of Figures

List of Tables

Abbreviations

Abbreviation	Description
AFM	Atomic force microscopy
ASDM	Air-spray drying method
AST	Accelerated stress test
CCM	Catalyst coated membrane
CV	Cyclic voltammetry
DLC	Double-layer capacitance
ECSA	Electrochemical surface area
EIS	Electrochemical impedance spectroscopy
FDM	Freeze-drying method
FTIR	Fourier transform infrared spectroscopy
GDE	Gas diffusion electrode
GDL	Gas diffusion layer
MEA	Membrane electrode assembly
MIP	Mercury intrusion porosimetry
NDM	No drying method
PEM	Proton exchange membrane
PEMFC	Polymer electrolyte membrane fuel cells
TDM	Thermal drying method
TPB	Three-phase boundary

Introduction

Low temperature polymer electrolyte membrane fuel cells (PEMFCs) produce electricity from the oxidation and reduction of hydrogen and oxygen gas, respectively. Platinum is the most active hydrogen oxidation and oxygen reduction reaction catalyst. Due to its high cost, platinum is deposited on an electron-conductive support, such as carbon, to decrease its loading while increasing its electrochemical surface area. The membrane electrode assembly (MEA) is the heart of the PEMFCs which contains the supported Pt in two catalyst layers, a proton exchange membrane and two gas diffusion layers.

The electrochemical reactions (H_2 oxidation and O_2 reduction) occur in the catalyst layers at what is called, the three-phase boundary (TPB). TPB is only obtained at the interface of ionomer and supported catalyst agglomerates which are accessible to reagents (H_2 and O_2).

These catalyst layers are coated on both sides of a proton exchange membrane using a catalyst ink slurry to form the electrodes. The catalyst ink slurry contains the supported catalyst and ionomer dispersed in an aqueous/organic liquid. The interface between ionomer and supported catalyst is formed during catalyst slurry preparation. During catalyst slurry preparation the ionomer molecule reconfigures itself on the supported catalyst in a manner which is determined by the fabrication method, the surface properties of the support and the dispersing medium. The adsorption of ionomer molecules onto the supported catalyst during catalyst slurry preparation, influences the catalyst accessibility. High ionomer content obstructs catalyst accessibility and decreases the utilization of the catalyst, while low ionomer content causes deficiency in proton connectivity which affects TPB sites and results in poor fuel cell performance.

Current proven processes for manufacturing high performing MEAs include heat-treatment during catalyst slurry preparation. Experimentally it was found that the optimal ionomer-catalyst-support contact is achieved when thermal drying is applied in the preparation of the catalyst slurry. This drying process, however, presented limitations in both time and energy consumption.

These limitations hinder mass production of MEAs and signified the knowledge gap between the effect of the drying during catalyst slurry preparation, the ionomer-catalyst-support interactions and fuel cell performance. Those limitations raised questions such as:

What is the impact of thermal drying during the preparation of catalyst slurry? Can the catalyst slurry be prepared with no drying process? How can the catalyst slurry preparation be optimised?

This research project therefore aims to provide a deeper understanding of the impact of heat-treatment during the preparation of catalyst slurry on MEA performance. The supporting objectives are therefore to:

- Study the ionomer-catalyst-support interactions made in varying ink preparation methods and using varying carbon supports.
- Determine the impact of catalyst slurry preparation method and the support interactions on the physical and electrochemical properties of the resulting MEAs.

With the new understanding, the catalyst slurry preparation method can be optimized to produce MEAs within a shorter timeframe which can match or outperform current fuel cell benchmarks. The following is the outlay used to structure the thesis:

Chapter 1: Literature Review

The first chapter introduces a background study of fuel cell technologies. It describes the different components of PEMFCs and their respective functions. The electrode reactions and the interactions of the solids in the catalyst layer are explained in this chapter. An introduction of the electrochemical techniques used in this study is included.

Chapter 2: Methodology

This chapter consists of the experimental procedures used to prepare the catalyst ink slurries and the resulting MEAs. The physical and the electrochemical characterizations (in-situ and half-MEA) techniques, protocols and procedures are also provided.

Chapter 3: MEA characterization

The third chapter presents the physical characterizations of the MEA such as: the degree of graphitization of the supported catalysts, the ionomer attachment and orientation onto the supported catalysts, the thicknesses, and the pore size distribution of the catalyst layers.

Chapter 4: In-situ electrochemical evaluation

This chapter shows the MEAs performances studied with polarization and power curves under various relative humidity conditions, their beginning of life electrochemical surface area, and their charge transfer resistances.

Chapter 5: Ex-situ electrochemical evaluation with the half MEA

This chapter presents accelerated stress tests (ASTs) done on catalyst layers (cathodes) prepared by varying catalyst slurry preparation methods in a Half MEA. Using a half-MEA cell

bridges the gap between ex-situ and in-situ electrochemical evaluations. EIS was included during AST to investigate the impact of carbon corrosion on the ionomer in the catalyst layer.

Chapter 6: Conclusions and recommendations

The final chapter presents the answers to the research questions raised during the course of this research project, the conclusions of the results presented and discussed in the previous chapters. Recommendations for future research on the topic and techniques are also included.

Chapter 1 Literature review

1.1.   Fuel cells

Fuel cells date back from the 19th century and can be defined as devices that convert chemical energy to electricity with low pollutant emission and high efficiency (Carrette *et al.*, 2001). The system is attributed to Sir William Grove while the principle is claimed to be discovered by the German Swiss Professor Christian Friedrich Schönbein. Fuel cells emerged due to the increasing demand for electricity in the 20th century. The increasing World population and the need for clean energy urged the development of fuel cells which can function as decentralized power plants. Improved overall efficiency is expected from decentralized power plants due to co-generation of electricity and heat (Carrette *et al.*, 2001).

1.2.1 Fuel cell principles

Fuel cells are composed of two electrodes: anode (positive electrode) and cathode (negative electrode), an electrolyte and an external circuit. Oxidation occurs at the anode where a substance loses electrons. While reduction takes place at the cathode, where a substance is an electron acceptor. Electrons produced during oxidation move through an external circuit to the cathode and generate electricity. While the electrolyte serves as an ion conducting medium from one electrode to the other.

In fuel cells, the free energy of the overall chemical reaction is converted to electrical energy. The former is related to the equilibrium cell potential under standard conditions in the following manner:

Equation 1-1: Gibbs free energy as a function equilibrium potential (Carrette *et al.*, 2001)

$$\Delta G = nF\Delta Uo$$

Where n and F (96485.33 C.mol^{-1}) are the number of electrons involved in the electrochemical reaction and Faraday constant, respectively. ΔG is the Gibbs free energy of the overall chemical reaction and ΔU_o is the equilibrium cell potential determined by the difference between the equilibrium voltages of the anode and cathode.

The Nernst equation is used to determine the thermodynamic equilibrium potential, however experimental equilibrium potential (open circuit potential) is lower than the Nernstian potential due to mixed potential formation and parasitic processes (Carrette *et al.*, 2001). The observed difference in the equilibrium potential when current flows, is mainly due to the finite rate of

reaction that occurs at the electrode, the potential difference is referred to as overpotential (η). Therefore, overpotential can be considered as the driving potential; positive overpotential generates anodic current and negative overpotential generates cathodic current.

Equation 1-2: Overpotential equation (Carrette *et al.,* 2001)

$$\eta = U - Ue$$

Where U and U_e are the applied potential and equilibrium potential at the electrode, respectively.

Current as flux is lowered due to resistances caused by the electrolyte and mass transport of reagents to active sites of the electrode. Three potential losses are observed during the conversion of chemical energy to electricity in a fuel cell (Carrette *et al.*, 2001):

- Activation losses: caused by charge transfer kinetics which occur in the low current density region.
- Ohmic losses: due to the electrolyte resistance to electron flow.
- Mass transport losses: insufficient transport of reagents to active sites of the electrode. These losses are dominant at high current density.

2.2.1 Types of fuel cells

Two parameters are considered when grouping the types of fuel cells: the electrolyte and the operating temperature. There are therefore high and low-temperature fuel cells. High-temperature fuel cells operate in the range of 600-1000°C. Molten carbonate fuel cell (MCFC) and solid oxide fuel cell (SOFC) are examples of high temperature fuel cells. Low-temperature fuel cells such as polymer electrolyte membrane fuel cell (PEMFC), alkaline fuel cell (AFC), direct methanol fuel cell (DMFC) and phosphoric acid fuel cell (PAFC) are operated in the range of 60-200°C (Carrette *et al.*, 2001).

1. **Molten carbonate fuel cells**: operate at high temperature range of 600-700°C. NiO catalyst is used at the cathode for oxygen reduction reaction (ORR) and Ni-Al or Ni-Cr metals are used as anode catalyst. Molten carbonates such as Li_2CO_3 and K_2CO_3 are used as electrolyte. MCFCs are used for stationary decentralized systems and in transportation (trains, boats, etc.).
2. **Solid oxide fuel cells**: use solid oxide materials (ZrO_2) as electrolytes. $LaSrMnO_3$ is used as cathode catalyst while Ni-cermet materials are employed as anode catalyst. SOFCs operate in a temperature range of 800-1000°C and are used for stationary decentralized systems and in transportation (trains, boats etc.) (Carrette *et al.*, 2001).

3. **Polymer electrolyte membrane fuel cells**: operate between 60-120°C and use a proton exchange membrane as electrolyte. Carbon supported platinum (Pt/C) catalyst is used for both cathode and anode. They have applications in stationary decentralized systems, transportation, space, military and energy storage systems (Carrette *et al.*, 2001) .

4. **Direct methanol fuel cells**: have applications in transportation, space, military, and energy storage systems. They are operated in the same temperature range as PEMFCs and use a proton exchange membrane as electrolyte. Pt/C and Pt-Ru/C are used as cathodic and anodic catalysts respectively with methanol as the oxidising agent (Carrette *et al.*, 2001).

5. **Phosphoric acid fuel cells**: operate in the temperature range of 120-220°C and use phosphoric acid as liquid electrolyte. As in the case of PEMFCs, Pt/C catalyst is used for both hydrogen oxidation and oxygen reduction reaction in the anode and cathode, respectively. PAFCs are the most advanced system for commercial development and have applications in combined heat and power for decentralized stationary power system (Carrette *et al.*, 2001).

6. **Alkaline fuel cells**: produce the highest electrical efficiencies and use potassium hydroxide (KOH) as electrolyte. Ni based catalyst activated with Pt is used for both anode and cathode while Pt/C gas diffusion electrodes may as well be used. AFCs have operating temperature below 100°C and are used in transportation, space, military and energy storage systems (Carrette *et al.*, 2001).

This present project was strictly focussed on low-temperature polymer electrolyte membrane fuel cells used in stationary and portable applications. The operating temperature considered in this study was 80°C.

1.2. Proton exchange membrane fuel cells

PEMFCs produce electricity from the oxidation and reduction of hydrogen and oxygen, respectively. Electrons are produced from hydrogen oxidation reaction (HOR) in the anode, which move to the cathode via an external circuit, generating current. Protons generated from the HOR migrate to the cathode via the proton exchange membrane (PEM) which serves as the electrolyte. Air (21 mol% O_2 and 79 mol% N_2) is fed to the cathode where the oxygen reduction reaction (ORR) occurs to generate water and heat. PEMFCs are therefore considered a clean electrical energy conversion systems as they produce electricity with heat and water as the only by-products (Kunusch *et al.*, 2012).

As described by Wee *et al.*, (2007); PEMFCs attract attention due to the following features:

- Low-operating temperature (60 - 120°C)
- Low weight
- Sustained operation at high current density
- Compactness
- Fast start-ups
- Suitability for discontinuous operation
- Potential for low cost and volume

The efficiency of PEMFCs can be high since the output impedance has a nonlinear dependency on operating conditions such as temperature, electric current, partial pressures, and humidity of gas reactants. The ideal equilibrium cell voltage can be estimated from the following equation:

Equation 1-3: Equilibrium cell voltage (Carrette *et al.*, 2001).

$$\Delta U_o = \frac{\Delta G}{nF}$$

Where ΔG is the Gibbs free energy change of the overall chemical reaction:

$$H_2 + \frac{1}{2}O_2 \rightarrow H_2O \quad -237 \text{ KJ/mol}$$
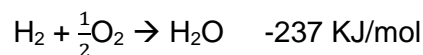
Due to the dependency of the change in the process Gibbs free energy on the fuel cell temperature and reagents partial pressures, the equilibrium cell voltage varies from its ideal value of 1.23V as in Equation 1-4, which explains the value of the open circuit voltage (OCV) being lower:

Equation 1-4: Equation of real equilibrium cell voltage in PEMFC.

$$\Delta U_o = 1.23 - 0.85 \times 10^{-3} (T_{FC} - 298.15) + 4.3 \times 10^{-5} T_{FC}[\ln (P_{H_2}) - \frac{1}{2}\ln (P_{O_2})]$$

The three forms of potential losses observed during PEMFCs operation are described in the previous section: activation, ohmic and mass transport losses.

1.2.1 Components of a PEMFC

Single PEMFCs are composed of a membrane electrode assembly (MEA) which is compressed between two flow field plates. A MEA consists of two catalyst layers (anode and cathode) coated on both sides of a PEM respectively, which is sandwiched between two gas diffusion layers (GDLs). Figure 1.1 illustrates the physical components of a single PEMFC.
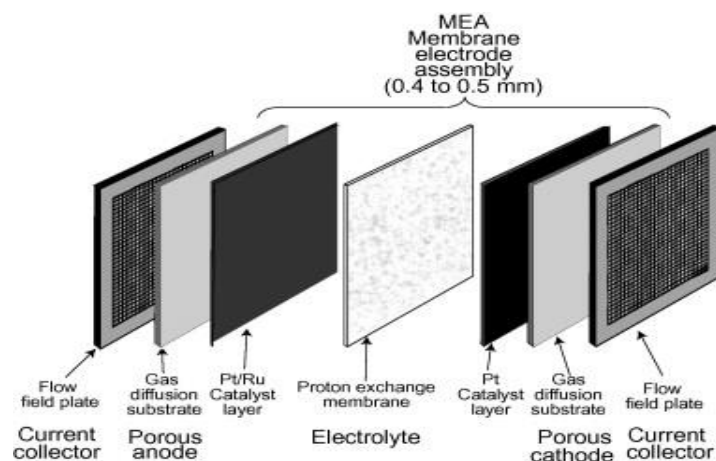
Figure 1.1: Structure of PEMFC (Rosa, 2013)

1.2.1.1. *Gas diffusion layer*

Gas diffusion layers ensure effective transport and diffusion of reagents to the catalyst layers as well as the removal of exhaust gases and water. As PEMFCs require humid conditions, GDLs play a key role in draining liquid water through the flow channels and forming an electronic connection between the catalyst layers and the current collectors (Cindrella *et al.*, 2009). GDLs consist of two layers:

- **Microporous layers**: are composed of carbon black powder and provide an appropriate surface pore size. This layer is hydrophobic and prevents flooding of the MEA while enhancing the electrical contact between the GDL and the catalyst layer interface.
- **Macroporous layer:** also referred to as gas diffusion backing (GDB), consists of a carbon paper or cloth. The macroporous layer provides electron conduction, elasticity, and structure to the MEA.

The balanced hydrophobic and hydrophilic properties of GDLs ensure water management in the fuel cell. Ideal GDLs should have properties such as good gas diffusion with optimum

bending stiffness, high porosity, good surface contact angle, air permeability, water vapor diffusion, electrical conductivity, crack free surface morphology, high mechanical integrity and enhanced oxidative stability. GDLs also need to be durable under various operating conditions including freezing (Cindrella *et al.*, 2009).

1.2.1.2. *Polymer electrolyte membrane*

A proton exchange membrane (PEM) is used as the electrolyte in PEMFCs transporting protons generated from the HOR to the cathode. Its chemical structure consists of a hydrophobic backbone; polytetrafluoroethylene (PTFE) and a hydrophilic side-chain; perfluoro sulfonic acid (PFSA). The proton conductivity and mobility through the PEM depend on the strength of its acid (or acid content expressed as ion-exchange capacity) and water uptake (Holdcroft, 2014). PEM possesses significantly low gas permeability to prevent gas crossover as this lowers the operating voltage of a fuel cell (Holdcroft, 2014).

PEM material cost and performance contribute to the major challenges to PEMFCs commercial progress. To increase its performance, research is focussed on improving its proton conductivity under low relative humidity conditions, on decreasing its water uptake in automotive application and increasing its operating temperature under low relative humidity (Mathias, 2005).

1.2.1.3. *Catalyst layer*

The catalyst layers are the core of a MEA. Catalyst layers facilitate the electrochemical reactions which convert chemical energy to electrical energy. These reactions include HOR and ORR at the anode and the cathode, respectively.

The catalyst layers are generally fabricated from a catalyst slurry which is a dispersion of supported catalyst; platinum nanoparticles supported on large-surface area carbon, and ionomer dispersion in a water-alcohol solvent. Two coating methods are predominantly used to deposit catalyst layers on both sides of the membrane; direct spraying method and the decal transfer method (Wang *et al.*, 2015).

An optimal electrode has a porous structure containing a fine dispersion of ionomer thin film over the catalyst. The thickness of the ionomer film is engineered low enough for wide protonic network and good electronic conductivity via tunnelling effect (Andersen, 2016). The catalyst may be coated directly on the membrane or on GDLs and they are referred to as catalyst coated membrane (CCM) and gas diffusion electrode (GDE) respectively.

In the catalyst layers, solid ionomer interacts with the supported catalyst in the presence of water molecules to maximise the three-phase boundary (TPB) (Berg *et al.*, 2006) by:

a) Forming pores in the catalyst layer through which gaseous reagents are supplied and water (water vapour and liquid water) is contained.
b) Transporting water in the ionomer film and providing proton conductivity in the catalyst layer.
c) Forming catalyst support agglomerates which provide electron conductivity and porosity in the catalyst layer.

TPB sites are active sites where the HOR and ORR can occur. The ionomer-supported catalyst layer structure form TPB sites in which the catalyst support provides electronic connectivity and protonic connectivity is provided by the hydrated ionomer. Mass transport of the reactant gasses to the active sites are provided through the porosity of the catalyst layer (Kim *et al.*, 2016). The illustration of TPB sites in the catalyst layer is shown in Figure 1.2.
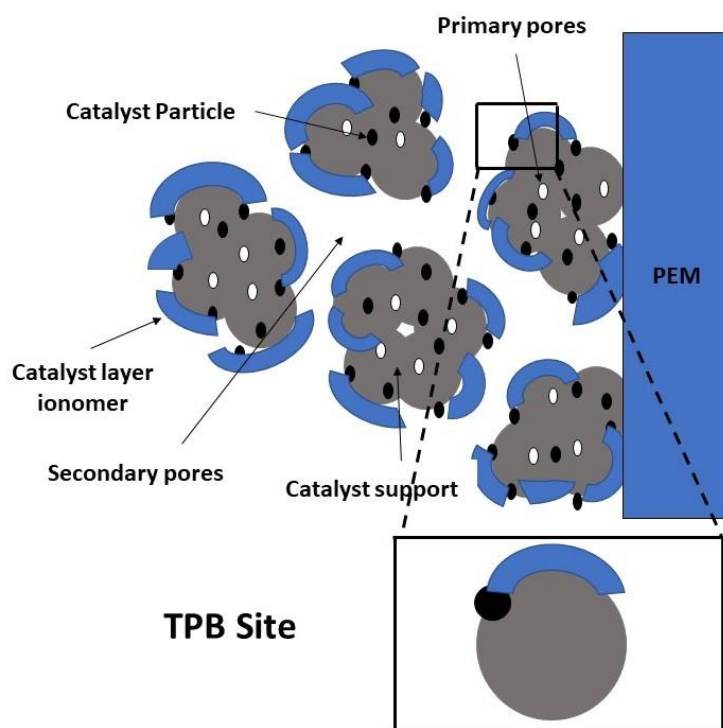
Figure 1.2: Schematic overview of the three-phase boundary.

The dispersing medium (catalyst slurry solvent) controls the formation and morphology of the catalyst layer structure and the amount of TPB sites due to their dielectric constants (measure of solvent polarity; ability to separate ions) (Kim *et al.*, 2016). Dispersing media with high ionomer main-chain mobility produce catalyst layers with deeper penetration of small ionomer clusters into supported catalyst agglomerates resulting in increased TPB sites (Kim *et al.*, 2016).

Ionomer.

The most common used ionomer in PEMFCs is a copolymer of tetrafluoroethylene (main-chain) and perfluoro (3,6-dioxa-4-methyl-7acetone) sulfonic acid (side-chain) (PFSA). PFSA based polymers are preferred in the catalyst layer due to their high protonic conductivity, its good mechanical, gas permeability, chemical stability and low electronic conductivity (Andersen *et al.*, 2014). The ionomer in the catalyst slurry ensures the transport of protons within the catalyst layer and between the catalyst layer and the membrane.

The sulfonic acid in PFSA side chain gives it hydrophilic properties which allows the ionomer to retain moisture and prevent dehydration of the membrane. The ionomer is used as a binding material between the supported catalyst and the PEM to impart the mechanical stability (Kim *et al.*, 2010).

The incorporation of ionomer during catalyst slurry has proven to extend TPB sites and to increase catalyst utilization (Holdcroft, 2014). The ionomer content in the catalyst layer has a huge impact on fuel cell performance; excess ionomer retains excess water, flooding gas transport-pores and results in low accessibility to platinum nanoparticles and reduces catalyst utilization. Deficient ionomer content causes poor contact between the supported catalyst and the ionomer, reducing TPB sites which results in low platinum utilization and poor fuel cell performance. Therefore, the utilization of the platinum catalyst and MEA performance are highly dependent on the ionomer content (Kim *et al.*, 2010).

Supported catalyst.

The kinetics of the HOR and ORR are relatively fast on Pt catalyst (Carrette *et al.*, 2001). Despite the high cost of Pt, essential characteristics such as high activity, selectivity, stability and poisoning resistance make Pt the most suitable catalyst for both the HOR and ORR (Holton and Stevenson, 2013). The activity of Pt catalyst is highly dependent on its particle size, surface property, electronic structure, and support structure.

Carbon is the most used catalyst support to prevent Pt particles agglomeration and to maximize the contact area to increase Pt utilization. It provides electron connectivity in the catalyst layer and its porosity enhances the mass transport of reagents to the catalytic sites (Sevjidsuren *et al.*, 2010).

To form catalyst layers, different catalyst loadings are targeted for various applications, in this project for stationary application, the anode and cathode consisted of 0.1 mg_{Pt}. cm^{-2} and 0.4 mg_{Pt}. cm^{-2}, respectively. With these targeted loadings, benchmark performances of 0.91 W/cm^2 at 0.65V have been achieved, which approximately corresponds to catalyst costs of $18/KW assuming $35 per Pt/C gram (Mathias, 2005).

Hydrogen oxidation and oxygen reduction reactions

Two key reactions take place in PEMFCs: hydrogen oxidation reaction (HOR) and oxygen reduction reaction (ORR) at the anode and cathode, respectively. Three steps are ascribed to the kinetics of electrode reactions:

- Mass transport of reactants to active sites
- Electron transfer during electrochemical reactions
- Mass transport of products

In PEMFCs, hydrogen molecules (gas phase) diffuse through the gas diffusion layer, into the catalyst layer (anode) to the active sites where atomic adsorption and oxidation occur on the Pt surface in the following electrochemical reaction:

$$H_{ads} \rightarrow H^+ + e^-$$
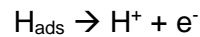
And the overall hydrogen oxidation is:

$$H_2 \rightarrow 2H^+ + 2e^-$$
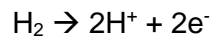
The electrons produced from HOR are conducted by the support and GDL to the external circuit. The protons are transported by the hydrated ionomer in the catalyst layer and then through the membrane to the cathode catalyst layer.

Oxygen molecules (from air feed) fed to the cathode take up the electrons and react with the protons to produce water. The water is removed through the macropores in the catalyst layer towards the GDL.

$$O_2 + 4H^+ + 4e^- \rightarrow 2H_2O$$
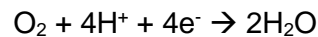
HOR is nearly spontaneous with a standard potential of 0.00V vs SHE in aqueous solution. The ORR is sluggish with a standard potential of 1.23V vs SHE, requiring a higher platinum loading on the cathode. The rates of H_2 oxidation and O_2 reduction (which are both surface reactions) solely depend on the Pt catalyst. The overall rate of reaction is primarily dependent on the catalyst layers; electrode materials such as Pt catalyst (for HOR and ORR), carbon support (electronic connectivity), the ionomer (protonic connectivity) and their interactions. The overall reaction rate, however, also depends on the operating conditions and the cell components properties.

1.3.   Ionomer-supported catalyst interactions

The interactions between the ionomer and supported catalyst occur during catalyst slurry preparation. The catalyst slurry consists of a suspension of solid ionomer and supported catalyst in an alcohol-water solvent. The latter defines the clustering of ionomer molecules, the agglomeration of supported catalyst and their interactions (Holdcroft, 2014).

Due to its amphiphilic property, the ionomer forms two types of clusters depending on the dispersing medium (Holdcroft, 2014):

a) Rod-like clusters are formed and are referred to as primary ionomer agglomeration, this is attributed to the interactions between the hydrophobic backbone of the ionomer.
b) The secondary ionomer agglomeration is caused by the electrostatic attractive force between the hydrophilic side-chain and results in larger ionomer clusters.

Supported catalyst agglomerates interact with ionomer clusters to form heterogeneous agglomerates during catalyst slurry preparation. These interactions are governed by the dielectric constant of the dispersing medium and the surface property of the support. (Holdcroft, 2014).

The surface property of the support such as hydrophobicity or hydrophilicity influences the agglomeration of support particles in the catalyst layer. During catalyst slurry preparation, support particles agglomerate in a bimodal manner forming mesopores and macropores (Holdcroft, 2014). The latter are the pores between support agglomerates and the former are the pores within the support agglomerates. The ionomer clusters interact with these support agglomerates to form TPB sites.

Two mechanisms are ascribed to ionomer adsorption unto supported catalyst; the first mechanism consists of forming a compact hydrophobic surface by the adsorption of the ionomer backbone unto hydrophobic carbon support. The second mechanism results in a compact hydrophilic surface by the adsorption of ionomer sulfonic group unto less hydrophobic carbon surface and Pt surface (Andersen *et al.*, 2014).
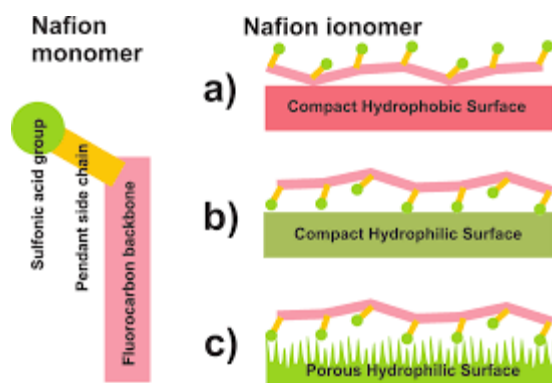
Figure 1.3: Nafion adsorption on surfaces of different wetting properties and porosity (Andersen *et al.*, 2014).

The ionomer-support-catalyst interactions play a key role in:

- **The formation of TPB sites**: the self-organization of ionomer and supported catalyst aggregates to form a porous structure.
- **The electrocatalytic efficiency**: which refers to the availability of the catalyst active sites (catalyst utilization).
- **The protonic and electronic connectivity**: provided by the ionomer and the carbon support, respectively.

1.3.1. Porosity in the catalyst layer

A porous catalyst layer structure can enhance the mass transport of reagents and products.

Ionomer-supported catalyst agglomerates present in the catalyst layer are composed of ionomer clusters and supported catalyst aggregates which exhibit a bimodal pore size distribution (Holdcroft, 2014). Two types of pores are formed on the catalyst layer (as observed in Figure 1.3):

1) Primary pores: formed within the supported catalyst agglomerates and ranging from 2 – 20 nm (Holdcroft, 2014).
2) Secondary pores: formed between supported catalyst agglomerates and possess a diameter > 20 nm (Holdcroft, 2014).

Primary pores on the support increase the surface area for further distribution of Pt particles and prevents agglomeration of Pt therefore, increased vacant sites. Primary pores provide a pathway for gaseous reagents to active sites where reactions take place. While the secondary pores channel water across the catalyst layer providing proton conductivity.

The microstructure of the catalyst layer is initiated during catalyst slurry preparation. The drying process, the dispersion method and the dispersing medium govern the self-organization of supported catalyst and ionomer (Holdcroft, 2014).

1.4.   Catalyst slurry preparation

Currently, the preparation of catalyst slurry consists of two stages: ink pre-preparation (mixing of ionomer and supported catalyst) and preparation of catalyst ink.

1) **Ink pre-preparation**: the ionomer solution is dispersed in water to reduce the clustering of ionomer molecules. Ultrasonic energy is used to disperse ionomer solution in water and to elongate ionomer molecules. The supported catalyst is added and dispersed in the ionomer-water dispersion to allow ionomer-interactions. The final step consists of removing water at a temperature below the glass transition temperature of the ionomer.

2) **Catalyst ink:** This stage consists of dispersing dried solids in a water-alcohol solvent to obtain catalyst ink which enables coating. Prior to mixing, the dried solids are pulverized by a mortar and pestle which reduce the solids to fine and uniform particles.

Benchmark performance is achieved when catalyst slurry is prepared by the described method. However, the drying process remains the most time and energy consuming, limiting mass production of MEAs using this method.
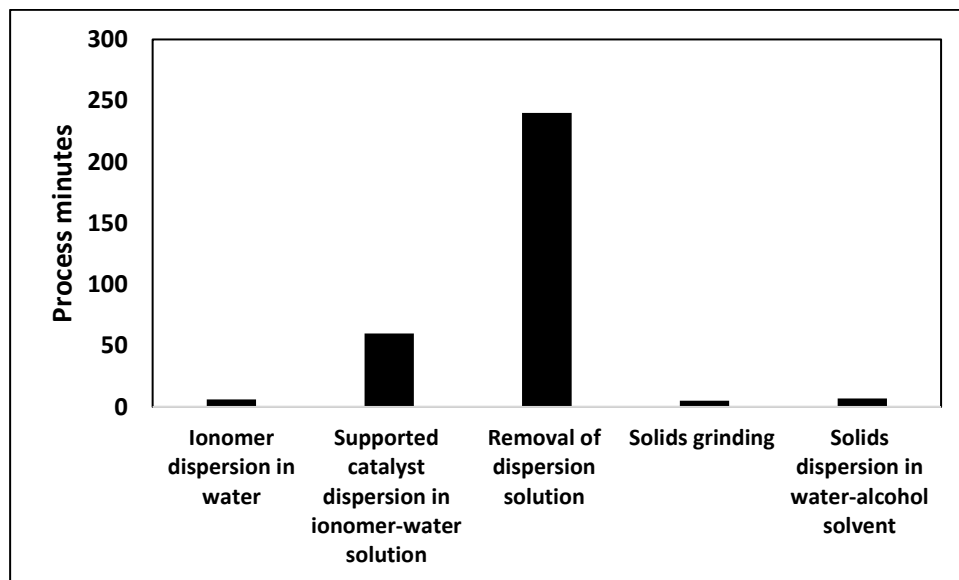
Figure 1.4: Process steps of catalyst slurry preparation

The drying process takes up more than 70% of the total ink production time, yet performance results indicate that the drying process is key to optimal MEA production. The nature of the ionomer-supported catalyst interactions due to the catalyst slurry preparation method is the identified gap knowledge. The focus of this study addresses this knowledge gap by providing answers to the following questions:

1. What is the impact of thermal on the ionomer-supported catalyst interactions during the preparation of catalyst slurry?
2. How can the catalyst slurry possibly be prepared with no drying process and maintain performance?

1.5. Drying process

The removal of liquid is referred to as drying. During catalyst slurry preparation, the drying step enables optimal contact for physical and chemical interactions between the ionomer, the catalyst (Pt) and the carbon support.

As a process, drying can be a batch or continuous process. During a batch drying process, the wet material is exposed to the heat and moisture is removed with time, while in a continuous drying process; there is a continuous inlet of wet materials and a continuous outlet of dried materials (Christie John, 1993). Three physical conditions are employed in which heat is applied, and moisture is removed which categorize the drying process:

- Heat is applied by direct contact with heated air at ambient pressure and water vapor is removed by air. The heat transfer is governed by Newton's cooling law of convection.
- Heat is added by direct contact with a solid material wall while wet materials are kept in a vacuum to increase the evaporation rate of the solvent. The heat transfer is governed by Fourier's law of conduction.
- Freeze-drying which consists of removing heat until wet materials are frozen, and moisture is removed by sublimation with the aid of mechanical vacuum pumps.

The following are the process units used to dry wet process materials:

Table 1-1: Instruments used in drying processes (Christie John, 1993)

Process units	Type of drying process
Tray dryers	Batch
Vacuum-shelf indirect dryers	Batch
Continuous tunnel dryers	Continuous
Rotary dryers	Continuous
Drum dryers	Continuous
Spray dryers	Continuous
Freeze dryers	Batch

During a drying process, the water content of a wet material decreases with time in two parts; a linear decrease from initial moisture to critical moisture followed by a non-linear decrease to equilibrium moisture. This decrease in water content per time can be related to the drying rate which shows two significant regions (Christie John, 1993):

- **Drying in the constant-rate period**: this consists of the evaporation of liquid films on the surface and the pores (from pores to the surface by capillary action or diffusion) of

the solid material. This free moisture is referred to as unbound water and its evaporation is independent of the solid material. Initial moisture is decreased to critical moisture during the constant-rate period.

- **Drying in the falling-rate period**: where evaporation recedes from the surface of the material, the heat transfer is governed by Fourier's law of conduction, as the temperature on the material surface is approximately that of heated air. Water vapor moves through the solid material by creating channels into the air stream and the critical moisture decreases to equilibrium moisture. The falling-rate period takes longer although larger amount of water is removed during the constant-rate period.

The carbon support in the catalyst slurry is a porous material. The moisture movements in these solids follow the theory of capillary movements during drying in the falling-rate period. The unbound water, in form of water vapor, therefore moves through and from the pores and voids to the surface of the solid by capillary action caused by the intermolecular forces between water and the solid material (Christie John, 1993). Derivations of mass transport and heat transfer equations which govern different types of dryers and different drying-rate periods are beyond the scope of this project. Understanding of drying processes is, however, necessary to predict the physical structure of the dried solid materials and its resulting impact on MEA performance. The morphology of the ionomer-supported catalyst structure formed during catalyst slurry preparation, affect the mass transport properties of the catalyst layer, the proton connectivity, platinum utilization and the electrochemical kinetics of a fuel cell (Holdcroft, 2014).

The electrochemical reactions that take place in the catalyst layers of PEMFCs and the electrochemical properties of the catalyst layers are studied by means of electrochemical properties such as polarization curve, cyclic voltammetry, and electrochemical impedance spectroscopy.

1.6. Electrochemical characterization

Electrochemical characterization may be done in-situ or ex-situ. In-situ tests consist of studying the electrochemical properties of a catalyst layer in a single cell while ex-situ tests consist of studying the electrochemical properties of a catalyst by using a three-electrode cell or half MEA design.

A three-electrode is constituted of a working electrode (where measurements are taken), counter electrode (used to close the current circuit in the cell), and a reference electrode which possesses a steady and well-known potential against which the measurements are taken. A liquid electrolyte is used as an ion conducting medium. Three-electrode cell is mostly used to study the activity of a catalyst because of its simple design, independence of temperature, pressure, and humidity as well as having no mass transport limitation (Pletcher, 2019).

While a single cell, used in fuel cell testing, is more complex and employs MEAs which consist of two electrodes: the anode and the cathode on a PEM sandwiched between two gas diffusion electrode. The measurements are influenced not only by the catalyst layers but by the operating conditions (cell temperature, compression force, relative humidity, back pressures, reagents flow rates, etc.) and the cell components properties. Ex-situ measurements provide actual electrochemical properties of the catalyst layers.

The following electrochemical techniques are used in this project.

1.6.1. Cyclic voltammetry

Cyclic Voltammetry (CV) is used to determine the electrochemical surface area (ECSA) in a catalyst layer. ECSA is the available Pt sites which facilitate HOR and ORR at the anode and cathode, respectively.

CV consists of measuring the current response to applied potentials. Three regions are observed during CV of carbon supported platinum (Pt/C) (Yadav, 2013) which are illustrated in Figure 1.5:

- **Hydrogen adsorption and desorption**: these reactions occur at lower voltage (0.05 – 0.4V), two pairs of redox peaks are observed at 0.27V and 0.12V and are attributed to strong and weak H-atoms adsorption and desorption to the surface of platinum with (100) and (110) orientations, respectively.
- **Double layer region (0.4 – 0.75V)**: where constant current response is observed, it is suggested that no electrochemical reactions occur at that region and it is referred as the non-faradaic region.

- **Formation and reduction of platinum hydroxide and oxide** are observed by a pair of redox peaks at high voltage (0.8 – 0.85V) as shown in Figure 1.5.
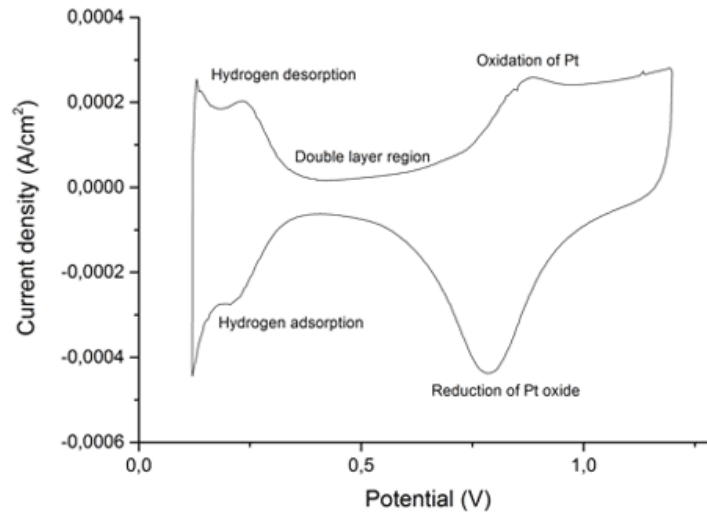
Figure 1.5: Cyclic voltammogram of Pt/C (Yadav, 2013)

The adsorption of hydrogen onto platinum surface indicates the availability of electrochemically active platinum surface area which are referred to as catalyst active sites. The charge generated from hydrogen adsorption can be determined by CV and it is directly proportional to the ECSA for a thin film of catalyst. The inverse of the specific charge required to oxidize a monolayer of hydrogen on a platinum surface is used as a constant of proportionality. A mathematical relation can be written as:

Equation 1-5: ECSA of Pt/c based catalyst layer (Pozio *et al.*, 2002)

$$\text{ECSA} = \frac{Q(Ads)}{[Pt] \times Q(s)}$$

Where $Q_{(s)}$ is the specific charge (210 $\mu C/cm^2$) and [Pt] is the platinum loading in g cm^{-2} on the working electrode (catalyst layer of interest). The charge generated from hydrogen adsorption (Q_{Ads}) is inversely proportional to the potential scan rate, the more rapidly the potential is applied, the lower the current response, which leads to low charge and consequently lower ECSA.

During fuel cell operation, hydrogen molecules may move to the cathode by diffusion, this phenomenon is referred to as hydrogen crossover. The hydrogen molecules react with oxygen in the cathode which yields peroxide radicals. Peroxide formation reduces the cathode potential below the open circuit potential. Additionally, hydrogen crossed over to the cathode generates current. Consequently, the effective ECSA is estimated when hydrogen crossover is taken into consideration.

1.6.2. Electrochemical impedance spectroscopy

Electrochemical impedance spectroscopy (EIS) measures the impedance by applying AC potential and measuring the current response. The latter and the former are both sinusoidal functions when plotted against time (Orazem and Tribollet, 2017).

Like resistance, impedance is the measure of a circuit's ability to resist the flow of electrons but it does not obey Ohm's law at all current and voltage. The impedance depends on frequency and the current response may not be in phase with applied voltage (Orazem and Tribollet, 2017).

EIS results are often represented in Nyquist plot (Figure 1.6) which consists of plotting the real part of impedance ($Z_o \cos \phi$) on the x-axis and the imaginary part ($Z_o \sin \phi$) on the y-axis. As impedance increases, the frequency decreases. Four types of resistance are observed in a cell; ohmic resistances (constituted of contact resistance and membrane resistance), resistances due to anode and cathode activations and resistance caused by mass transport (Aksakal and Sisman, 2018).
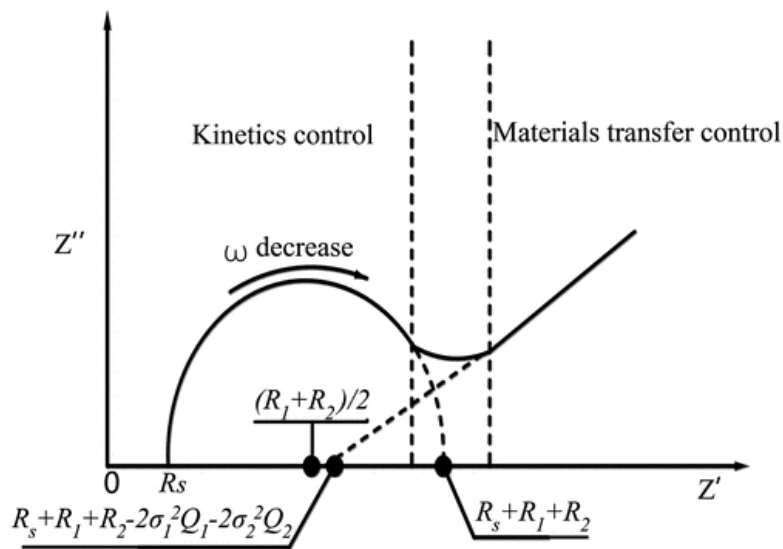
Figure 1.6: Nyquist plot (Tan *et al.*, 2019)

Figure 1.6 can be represented as an electrical circuit (Randles circuit) in which each component of the cell is represented as a circuit attribute such as resistor, capacitor, and inductor (Jang *et al.*, 2009).

1.6.3. Polarization curve

A polarization curve plots the voltage output for an applied current density. Polarizing an electrode consists of forcing the cell potential away from the open circuit potential (OCP). The polarization curve is used as a representation of a cell performance. During polarization tests,

hydrogen flows to the anode where oxidation occurs, and air is fed to the cathode where the ORR occurs.

Three significant losses are observed in polarization curves:

a) Ohmic losses which are caused by contact losses, ionic conductivity losses and membrane resistances.
b) Activation losses which are due to the energy required to initiate the electrochemical reactions (low current density).
c) And mass transport losses which are observed at high current density due to insufficient transport of reactants (air and hydrogen) to the catalyst layer.

The total potential loss is readily observed on the polarization curve. For a given equivalent open circuit potential, the MEA with the lowest potential loss is likely the best performing (Sedaghat *et al.*, 2013). Figure 1.7 illustrates the current-voltage polarization curve.
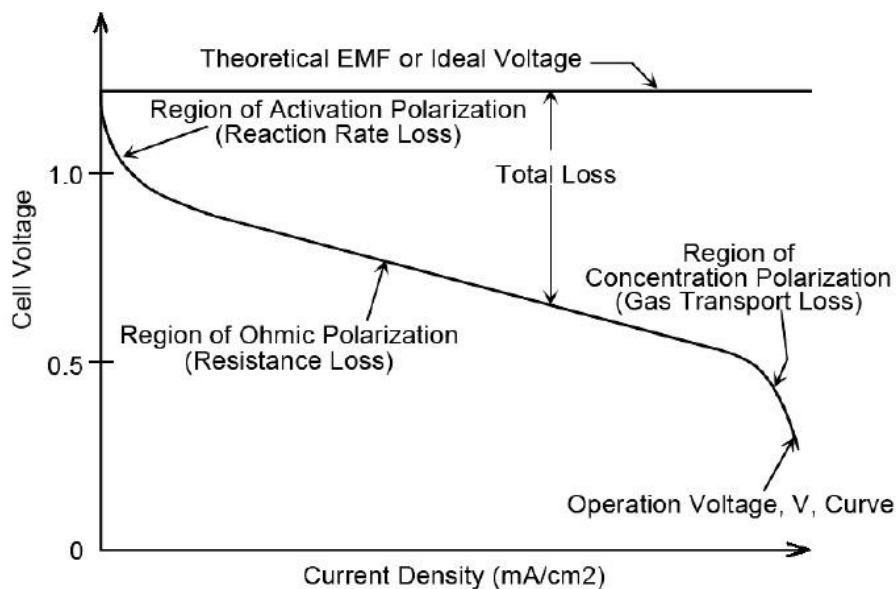
Figure 1.7: Polarization curve (Sedaghat *et al.*, 2013)

Performance tests are highly dependent on the testing conditions which include the cell temperature, reagent relative humidity, the reagent flow rates, the stoichiometry ratio of the reactants and the back pressures exerted on both electrodes (anode and cathode) to remove water and exhaust.

1.6.4. Support corrosion

During fuel cell shutdown and start-up, air diffuses from the cathode to the anode and forms an air-hydrogen boundary which divides the MEA into four distinct regions, two on both anode

and cathode sides. Due to the H_2 oxidation and O_2 reduction which now occur on the anode, the potential of one of the regions on the cathode side will be nearly double the open circuit voltage (OCV = 1.0V) and will experience water electrolysis and carbon corrosion (Tang *et al.*, 2006).

$$2H_2O \rightarrow O_2 + 4H^+ + 4e^-$$

$$C + 2H_2O \rightarrow CO_2 + 4H^+ + 4e^-$$

$$C + O_2 \rightarrow CO_2$$
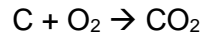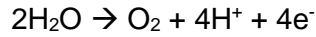
The rate of carbon corrosion depends on the catalytic activity of Pt and the surface property of the carbon support such as its degree of graphitization. Sp^{-3}-hybridized carbon (one *s*-orbital and three *p*-orbitals) shows little resistance to oxidize while Sp^{-2}-hybridized carbon (one *s*-orbital and two *p*-orbitals) shows resistance to carbon corrosion.

In the case of incomplete combustion, carbon monoxide is produced and adsorbed on Pt surface at potentials below 0.55V. With the aid of Pt catalyst, CO is converted to CO_2 at higher potentials (Tang *et al.*, 2006). Carbon corrosion is undesirable in PEMFCs since the carbon support prevents Pt nanoparticles agglomeration and provides electronic connectivity. Detachment of Pt particles and their agglomeration cause losses in TPB sites and ECSA which results in low performance.

Therefore, carbon support corrosion is studied by the accelerated stress tests in a nitrogen atmosphere which consist of modulating the potential between 1.0 – 1.5V for a large number of cycles and measuring the ECSA (by CV) intermediately.

Summary

Thermal treatment during catalyst slurry preparation produces MEAs which achieve benchmark performance for stationary application. However, no current study explains the impact of the drying step, during catalyst slurry preparation, on the formation of the ionomer-supported catalyst structure and how that effects MEA performance. This study employed physical and electrochemical characterizations to better understand the ionomer-supported catalyst interactions and the impact of the drying step. Different catalyst slurry preparation methods would be used; varying the drying rate, physical conditions used to add heat and to remove water:

1) Thermal drying method.
2) No drying method.
3) Air-spray drying method.
4) Freeze-drying method.

Physical characterizations would be used to study physical properties of the catalyst layer such as: thickness, specific surface area and porosity, the support's degree of graphitization, ionomer attachment on supported catalyst and ionomer-supported catalyst agglomerates size distribution. While electrochemical characterizations would consist of performance tests, determining ECSA, MEA resistances and durability studies.

The results obtained from physical and electrochemical characterizations, would provide insight on the impacts of the drying step as well as the support's degree of graphitization on the ionomer-supported catalyst interactions and ultimately MEA performance.

Objective

This study aimed to elucidate the impact of thermal drying on the ionomer-supported catalyst interactions. With this understanding, the goal would then be to devise a catalyst slurry preparation method which reduces MEA fabrication time. To achieve the project aim, the following objectives were set:

- Studying and understanding the adsorption of ionomer molecules onto the supported catalyst by several physical characterization and electrochemical techniques.
- Determining the influence and significance of thermal drying on ionomer-catalyst interactions and their physical structure after the drying process.
- Optimizing the preparation of catalyst slurry to be time and energy efficient.

The surface property of the support such as its degree of graphitization was varied to elucidate the ionomer-supported catalyst interactions. Three additional preparation methods were included to isolate the effect of batch thermal drying on the ionomer-supported catalyst interactions. And they consist of:

1. Catalyst slurry preparation with no drying step.
2. Catalyst slurry preparation with air-spray drying step, which aimed to reduce the process time.
3. Catalyst slurry preparation with freeze drying step.

Chapter 2 Methodology

This chapter explains the experimental procedures and techniques used to prepare and characterize the catalyst slurries as well as the resulting MEAs. Four slurry preparation techniques using two different catalyst supports we investigated.

Two primary tasks constituted the methodology of this study:

- **Experimental procedures**: catalyst slurry preparation and membrane electrode assembly (MEA) fabrication.
- **Material characterizations**: physical characterizations and electrochemical characterizations.

2.1.   Experimental procedures

2.1.1. Catalyst slurry preparation

2.2.1.1.   Materials

Two supported catalysts were used; graphitized Vulcan supported platinum (GV40) and Vulcan supported platinum (V40) from Mintek. The platinum loading in both supported catalysts was 40 wt% and their carbon supports differed in their degrees of graphitization. The ionomer solution of Aquivion® D72-25BS (Sigma-Aldrich) contained 26.53 wt% of solid Aquivion. Deionized water and isopropanol (Sigma-Aldrich) were used as dispersing media. The proton exchange membrane (PEM) and gas diffusion layer (GDL) used in this study were MF740 Gore membrane and AvCarb, respectively from *Fuel Cell Store*.

2.2.1.2.   Ink pre-preparation

Two principal methods were utilized in this study: thermal drying method (TDM) and no drying method (NDM). Two additional methods were introduced to isolate the impacts of drying rate and heat: air-spray drying method (ASDM) and freeze-drying method (FDM).

Aquivion was dispersed in deionized water in a beaker in an ultra-sonic bath under ambient conditions for 20 minutes. The supported catalyst (GV40 or V40) was added and dispersed (using ultra-sonication) in the ionomer-water solution for:

a) 1 hour at room temperature (20-25°C): in the case of TDM, FDM and ASDM.
b) 2 hours at 60°C (bath temperature): in the NDM.

c) ADSM slurries were further dispersed by high-shear stirring for 10 minutes at 9000 rpm.

Thermal drying method

The ionomer-supported catalyst dispersion was thermally dried in a tray dryer at a constant temperature of 75°C. The duration of the drying step depended on the batch size: 4 hours for 60g catalyst slurry batch. A dry percentage range of 99 – 101% was permitted. The latter was estimated by equation 2.1.

Equation 2-1: Dry percentage equation

$$Dry\% = \frac{dried\ solid\ ionomer\ and\ supported\ catalyst\ (g)}{Solid\ ionomer + supported\ catalyst\ mass\ before\ drying\ (g)}$$

To avoid contamination, the ionomer-supported catalyst dispersion was contained in a glass beaker and covered by poked aluminium foil during drying.

Freeze drying method

Virtis benchtop K freeze dryer was used to dry the ionomer-supported catalyst dispersion at the temperature at which water sublimation occurs for more than 24 hours (depending on batch size) to reach 100% dry. The dry percentage was calculated by equation 2.1.

Air-spray drying method

The ionomer-supported catalyst dispersion was air-spray dried (Buchi Mini Spray Drier B290) at the flow rate and air temperature of 10 ml/min and 75°C, respectively. Synthetic air was fed at a constant flow rate of 4 NLPM.

The ionomer-supported catalyst dispersion was thin to avoid pipe blockage therefore, the amount of water was increased fourfold before air drying (as in Table 2.1). The dry percentage was estimated by equation 2.1.

2.2.1.3. Catalyst ink

The process steps for catalyst ink preparation and agitation were used for all pre-preparation methods. A mixture of deionized water and isopropanol was used as the dispersing medium; dispersion took place in three stages in an ice-bath to prevent exothermic dehydrogenation of isopropanol on Pt:

- Magnetic stirring at 350 rpm for 2 minutes.
- High-shear stirring at 9000 rpm for 5 minutes.

Tables 2.1 contained the mass composition of the catalyst slurry:

Materials	NDM	TDM, FDM, ASDM
	Weight %	Weight %
Aquivion	3.50	3.50
Supported catalyst	3.10	3.10
Water (before drying step)	10.3	10.3
Iso-propanol	36.2	36.2
Water	36.5	46.9

2.1.2. MEA fabrication

The catalyst ink was coated onto the PEM sandwiched between GDLs to form a MEA. Catalyst coated membranes (CCMs) were fabricated by ultrasonic spraying of the catalyst slurry on both sides of the PEM (MF740 Gore). Pt loading targeted for anode and cathode were 0.1 mg of Pt cm^{-2} and 0.4 mg of Pt cm^{-2}, respectively and were verified by measuring the membrane mass before and after spraying.

To increase the mechanical strength of CCMs, sub-gaskets were hot-pressed on the anode and cathode at 78.9°C and 3 bar for a minute. Two PET layers were attached to frame the active areas on each side of the membrane and the silicon layer was only added on the cathode side. The gasketed CCM (shown in Figure 2.1) was sandwiched between GDLs (AvCarb) forming a MEA.
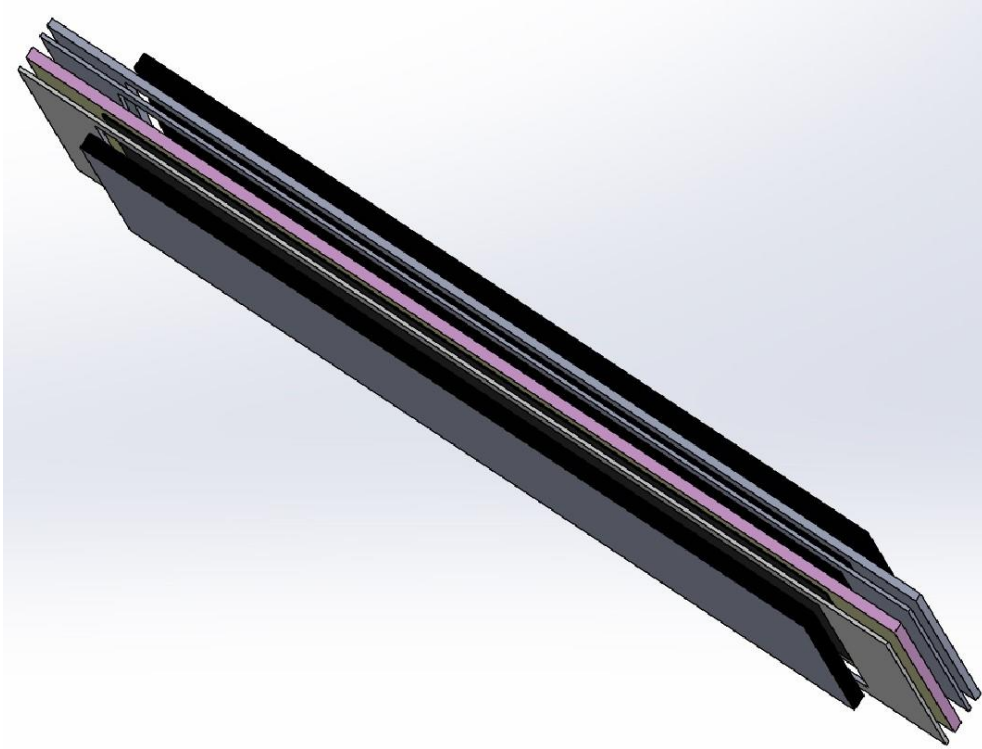
Figure 2.1: Gasketed catalyst coated membrane: outer layers in black (GDLs); one thick silicon layer in grey; two thin layers in grey (PET layers); layer in purple (PEM).

2.2. Material characterization

2.2.1. Physical characterization

Physical characterizations consisted of:

- Raman spectroscopy: to determine the degree of graphitization of the carbon support.
- Fourier transform infrared spectroscopy (FTIR): to study the ionomer attachment on the supported catalyst layer.
- Scanning electron microscopy (SEM): to study the surface and the cross-section of the coated catalyst layers.
- Mercury intrusion porosimetry (MIP): to determine the pore size distribution and the total intrusion volume of the catalyst layers.
- Atomic force microscopy (AFM): to determine the ionomer-supported catalyst agglomerates size distribution on catalyst layers.

2.2.1.1. Raman spectroscopy

Raman spectroscopy consists of determining vibrational modes of molecules. Carbon Raman spectra consist of two major bands which are readily observed at the wavenumber region of 1350 cm^{-1} and 1590 cm^{-1} and are referred to as D-band and G-band, respectively as illustrated in Figure 2.2. D-band and G-band are assigned to Sp^{-3}-hybridized carbon (one *s*-orbital and three *p*-orbitals) and Sp^{-2}-hybridized carbon (one *s*-orbital and two *p*-orbitals) respectively (Hodkiewicz, 2010).
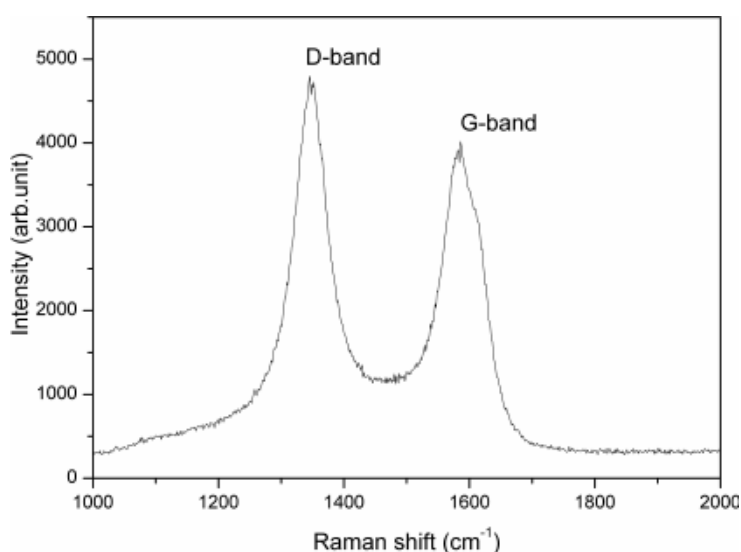
Figure 2.2: Raman spectrum of carbon (Dychalska *et al.*, 2015)

The order of defect is calculated by the ratio of D-band intensity to G-band intensity (Equation 2.3) and is indirectly proportional to the degree of graphitization (Hodkiewicz and Scientific, 2010).

Equation 2-2: Order of defect (Hodkiewicz and Scientific, 2010)

$$\text{OD} = \frac{I(D{-}band)}{I(G{-}band)}$$

The Witec Confocal Raman Microscope (alpha300) was used to determine the degree of graphitization of V40 and GV40.

2.2.1.2.   Fourier transform infrared spectroscopy

FTIR uses infrared spectrum and measures the amount of infrared spectrum which is absorbed by a chemical species. FTIR spectra consist of absorbance and wavenumber as y-axis and x-axis, respectively.

Three distinctive functional groups are present in Aquivion, the ionomer used in the current study; sulfonate anions (SO^{-3}), ether group (C-O-C) in the side chain and carbon monofluoride (CF_2) in the perfluoro backbone (Hanawa *et al.*, 2012). These functional groups can be seen in Figure 2.3 and the bands are assigned in Table 2-2.
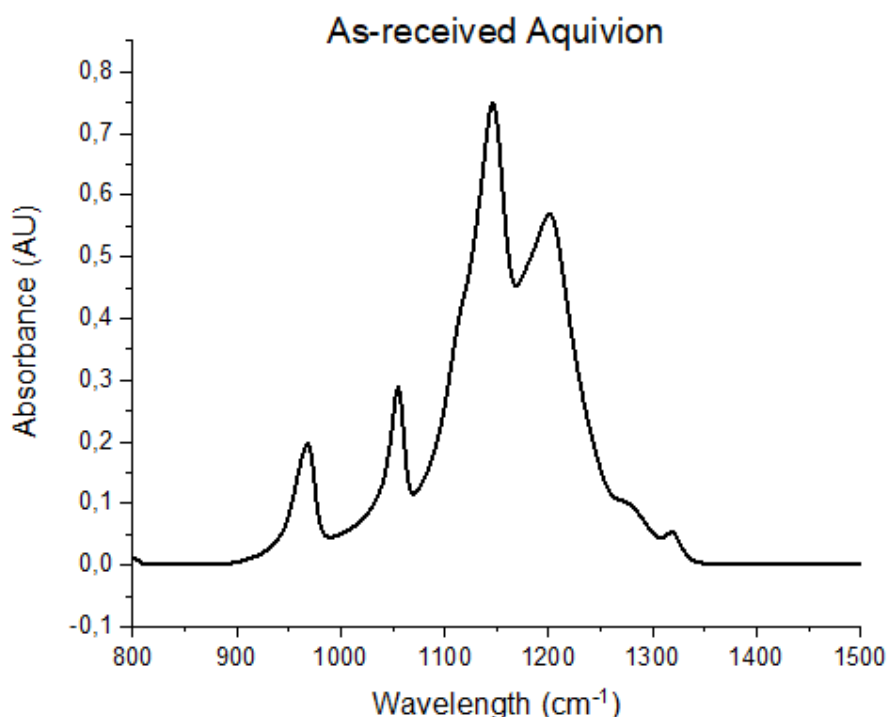
Figure 2.3: FTIR spectra of Aquivion in the range of 700-1500 cm^{-1} (Danilczuk et al., 2011)

Table 2-2: FTIR band assignment for Aquivion (Danilczuk *et al.*, 2011)

Wavenumber (cm^{-1})	Band assignment
1320	$V_{as}(CF_3)$
1301	V_s(C-F)
1280	$V_{as}(SO_3^-)$
1199	$V_{as}(CF_2)$
1143	$V_s(CF_2)$
1134	V_{as}(C-O-C)
1056	$V_s(SO_3^-)$
969	V_s(C-O-C)
806	V_s(C-S)

FTIR spectrophotometer (Perkin-Elmer Spectrum One FT-IR Spectrometer using Attenuated Total Reflectance) was used to study ionomer (Aquivion) attached to the supported catalyst.

Sample preparation consisted of:

1. Separating the ink solids (ionomer-catalyst agglomerates) from the water-isopropanol solvent. The separation was achieved by centrifuging at 14000 rpm until solid precipitates and clear solvent were observed.
2. Drying the solid precipitates at 60°C.

2.2.1.3. Scanning electron microscopy

A high-resolution Field Emission SEM, combining low kV imaging Nova NanoSEM was used to study the surface of catalyst layers. While the cross-sectional area and thicknesses of catalyst layers were studied under Tescan MIRA3 RISE SEM.

The sample preparation consisted of submerging a CCM in liquid nitrogen for a minute and the frozen CCM was cut by a clean blade to avoid contaminants deposition on the cross-section.

2.2.1.4. Mercury intrusion porosimetry

The pore size distribution and intrusion volume of the catalyst coated membranes were acquired with a AutoPore IV 9500 V1.09 (University of Western Cape).

2.2.1.5. Atomic force microscopy

The aggregates in the catalyst layers were analysed with Tosca series atomic force microscopy by Anton Paar.

2.3. Electrochemical characterization

The electrochemical characterizations were performed in-situ and with a half-MEA setup. In-situ tests consisted of evaluating the beginning of life (BoL) MEA performance, the electrochemical surface area and the charge transfer resistances. The half-MEA setup was used to systematically study and perform an accelerated stress test on the cathode catalyst layer.

2.3.1. In-situ electrochemical evaluation with a full MEA

In-Situ electrochemical tests were run in a Pragma single cell by using FuelCon evaluator. Pragma fuel cell is constituted of:

- Monopolar plates with selected flow-fields design.
- Gold plated current collectors.
- Stainless steel compression plates with guiding pins.
- Integrated heating cartridges.
- Type-k thermocouple.
- Voltage sense pins.
- Gas connectors.
- Set of nuts, rods, washers.
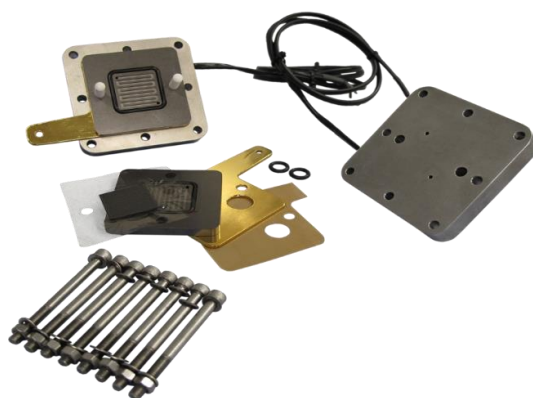
Figure 2.4: Pragma single cell

The 25 cm^{-2} MEAs were compressed inside the Pragma single cell at 4.8 bar.

2.3.1.1. Cell conditioning
The cell conditioning consisted of:

1. Initial cell conditions: nitrogen gas flowed in the anode and cathode at 25 NLPM, the feed lines temperatures were constant at 50°C and the bubblers temperatures were

set at 52°C (65 RH). The anode and cathode back pressures were 1.5 bar and the cell temperature was raised to 80°C.

2. Potential cycling between open circuit (or 1.0V) and 0.3V: with hydrogen and air flowing in the anode and cathode, respectively. The potential was held at 0.8 for 30 seconds and at 0.3 for 30 minutes. The number of 1.0V – 0.3V cycles for break-in and re-conditioning was 12.

2.3.1.2. Performance test

The performance of the MEAs was determined by current-voltage polarization curve at a specific relative humidity. Table 2-3 summarises the parameter set for different humidity conditions.

Table 2-3: Testing conditions for 25 cm^{-2} MEAs.

Parameters	100% RH	74% RH	65% RH
Cell temperature (˚C)	80	80	80
Line temperature (˚C)	90	90	90
Bubbler temperature (˚C) Cat/Anod	80/75	59/59	52/52
Back pressure (Bar)	2	1.3	1.5
Stoichiometry cat/Anod	2/1.5	2/1.5	2/2
Hydrogen flow (NLPM)	0.15	0.15	0.11
Air flow (NLPM)	0.30	0.30	0.30

2.3.1.3. Cyclic voltammetry

The BoL electrochemical surface area (ECSA) of catalyst layers was calculated by the charge produced by hydrogen adsorption during CV.

Prior to performing CV, the cathode was purged with nitrogen for 30 minutes at 30 NLPH to remove traces of oxygen. This was to prevent Pt-oxide formation at high voltage. The set parameters during the CV measurement are summarized in Table 2-4.

Table 2-4: Cyclic voltammetry settings to determine the ECSA.

Parameter	Parameter Setting
Upper votex potential (V)	0.9
Lower votex potential (V)	0.04
Scanrate (mV/s)	50
Cell temperature °C	80
Bubble temperature °C	80/75
Hydrogen flow (NLPM)	0.5
Number of cycles	15

Equation 1.5 was used to determine the ECSA of the MEA.

2.3.1.4. Hydrogen crossover

Hydrogen crossover consisted of increasing voltage stepwise from 0.2V to 1.0V collecting current at each voltage in 200ms intervals. Current generated by hydrogen crossover was subtracted from CV current to estimate an accurate ECSA.

2.3.1.5. Electrochemical impedance spectroscopy

Two protocols were followed to determine the charge transfer resistance of ORR and HOR.

1. The charge transfer resistance of ORR and HOR was determined by performing EIS frequency sweep from 20KHz to 0.1Hz at 20 mA/cm^2. The hydrogen and oxygen flowrates were set at 0.2 NLPM and 0.5 NLPM, respectively.
2. These EIS results were fitted in a Randle's circuit by using ZView.

Further studies of the electrochemical properties of catalyst layers required a half-MEA setup. The half-MEA facilitated the systematic study of only one electrode and enabled analysis of only catalytic sites with proton connectivity through the ionomer. The half-MEA was therefore, a tool used to study the ionomer-supported catalyst interactions and their electrochemical impact on performance and durability.

2.3.2. Ex-situ electrochemical evaluation with a half-MEA cell

A half-MEA setup is a combination of a single cell and a three-electrode cell where the working electrode is the catalyst layer and the protons are provided by an acid electrolyte through a PEM. A half-MEA facilitates the systematic study of only one electrode, it is stable and offers insights into the catalytically active TPB sites in the catalyst layer. It is unrestricted to gas diffusion limits and the results are independent of the counter and reference electrode used (Sharma and Andersen, 2018).

A half-MEA setup was designed and assembled in-house. It consisted of a half cell with two gas streams (inlet and outlet), a cupper current collector and a parallel flow field plate. The half MEA electrode consisted of a gas diffusion layer, and a catalyst layer (cathode) of 10 cm^2 on a PEM. One side of the MEA was clamped to a Teflon (acid resistant) pool of 3.5 cm high with a hole of 10 cm^2, which contained the electrolyte,1.0 M H_2SO_4. A silver chloride (Ag/Cl) and carbon rod were immersed in the electrolyte and served as the reference and counter electrodes, respectively. To ensure proton conductivity; the acid electrolyte was in direct contact with the PEM while nitrogen flowed through the catalyst layer (working electrode). The reagent was bubbled through water at 25°C for humidification.
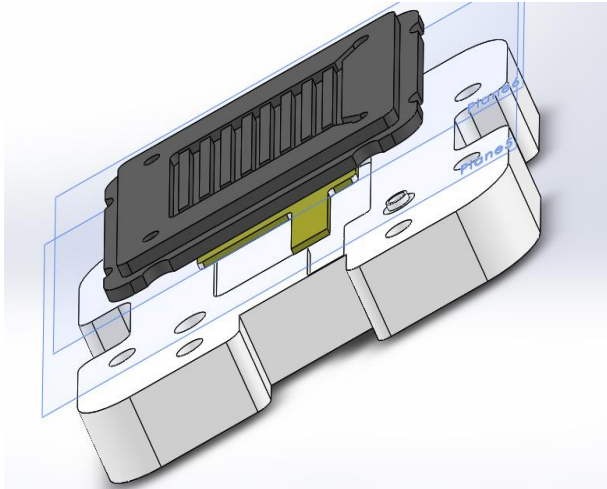
Figure 2.5: : Half-MEA setup design on SolidWork; flow field plate in grey, gold plated current collector in yellow.
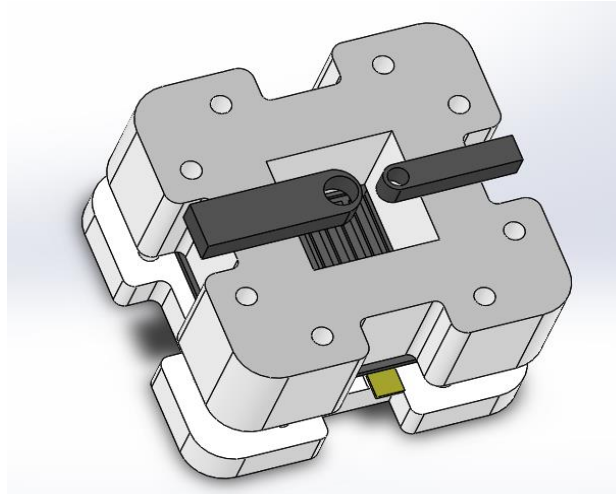
Figure 2.6: Half-MEA setup design on SolidWork; Top-view of the half-MEA setup with the electrolyte pool. Counter and reference electrodes holders in grey.
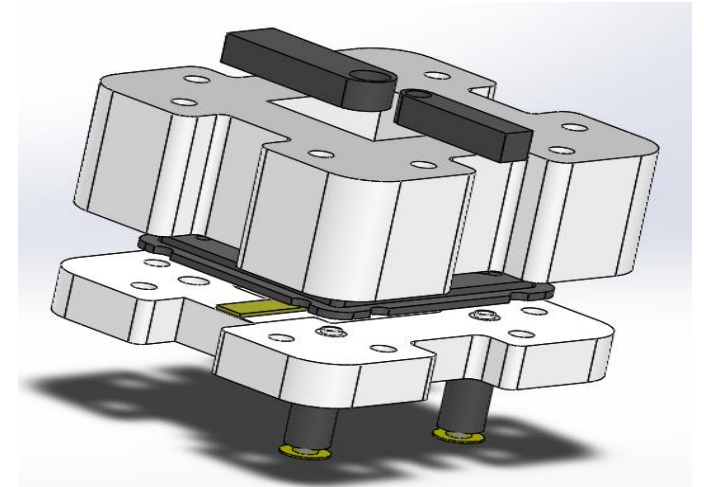
Figure 2.7: Half-MEA setup design on SolidWork; Side-view of the half-MEA setup

2.3.2.1.   Cyclic voltammetry

Prior to CV measurements, the half-cell was conditioned by initially purging with N_2 for 15 minutes and potential cycling between 0.05 – 1.2 V Vs RHE for 500 cycles at 100 mV/s in a N_2 atmosphere.

A series of CV was employed to study the changes in ECSA and double-layer capacitance (DLC) which represented the ionomer-catalyst interactions and ionomer-support interactions, respectively.

The ECSA was estimated by the charge generated from hydrogen adsorption during CV as in Equation 1.5. The DLC was determined as the difference in the cathodic and anodic scans in the non-faradaic region of the CV. A potential range of 0.05 – 1.20 V and scan rate of 10 mV/s were used.

2.3.2.2.   Accelerated stress test

AST performed in the half-MEA setup allowed the study of the degradation mechanisms of the catalyst layer by observing the changes in ECSA and DLC. These changes in ECSA and DLC were used to isolate the effect of the catalyst slurry preparation method on the ionomer-catalyst and ionomer-support interactions respectively (Sharma and Andersen, 2018).

AST consisted of 7000 cycles of linear sweep voltammetry (LSV) within a potential range of 1.0 - 1.5 V (Sharma and Andersen, 2018). This specific potential range was selected to allow support corrosion. The ECSA and DLC were determined after 0, 20, 100, 200, 300, 400, 500, 600, 800, 1000, 2000, 3000, 4000, 5000, 6000 and 7000 stress cycles. The ECSA was determined by CV, within a potential range of 0.05 – 1.20 V and with a scan rate of 50 mV/s. The DLC was determined by analysing the non-Faradaic region of CV (0.4 - 0.75).

Chapter 3 MEA material characterization

This chapter provides the results and discussion on the material characterization of the MEAs made using various catalyst slurry preparation methods. <mark>Due to time and material limitations, no V40 MEAs were prepared by the freeze drying method, nevertheless the impact of heat during catalyst slurry preparation was elucidated with GV40 TDM and GV40 FDM MEAs.</mark> Herein, the physical structure of the MEAs i.e., the catalyst layer thickness, catalyst layer porosity, particle size distribution, ionomer-supported catalyst interactions and the degree of graphitization of the supported catalysts were studied.

3.1. Raman spectroscopy

Raman spectroscopy was used to determine the degree of graphitization of the as-received supported catalysts and their respective supports. Two bands were observed at the region of 1350 cm^{-1} and 1590 cm^{-1}. The bands are referred to as D-band and G-band, respectively. D-band represents sp^3-hybridized carbon (one s-orbital and three p-orbitals) and G-band represent sp^2-hybridized carbon (one s-orbital and two p-orbitals), both with characteristic angles of 109.5° and 120° respectively. When assembled in one crystal; sp^3-hybridized carbon atoms form the typical diamond structure (three-dimensional) with a band gap of 5eV like an insulator, hence poor electron conductivity (Peschel, 2011). A typical graphite structure is obtained when sp^2-hybridized carbon atoms are assembled and due to the connection of its valence and conduction bands, graphite is a good electron conductor (Peschel, 2011). The Raman spectrum of the supports used in this project; Vulcan and graphitized Vulcan (GV) are presented in Figure 3.1.
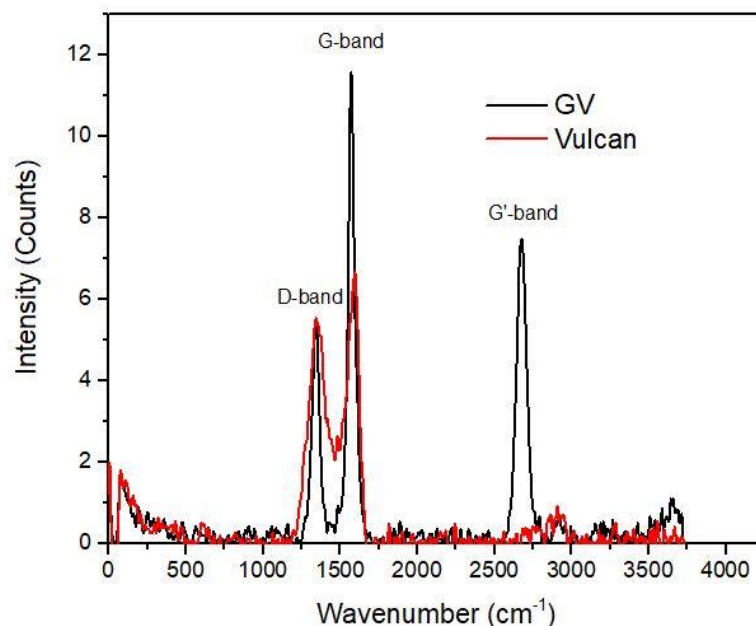
Figure 3.1: Raman spectra of Vulcan and GV.

The D-band and G-band were observed on both Vulcan and GV spectra, but an additional band was observed in the GV spectrum around 2690 cm^{-1} and is indicative of the interactions of the stacked graphene layers in graphite which tend to shift the bands to higher frequency (Hodkiewicz and Scientific, 2010). This third band (around 2690 cm^{-1}) was referred to as the G'-band. The order of defect was estimated using Equation 2-2.

Vulcan had a higher order of defect (0.999) as shown in Figure 3.2 B, consequently it had a lower degree of graphitization compared to GV (0.479). Therefore, GV had a higher electron conductivity compared to Vulcan which was richer in sp^{-3}-hybridized carbon. Andersen *et al.*, 2014 reported that carbon supports with a high degree of graphitization showed the highest water contact angle, indicating less water wetting properties and stronger hydrophobicity. Vulcan could be considered as less hydrophobic than GV.

From the Raman spectra of GV40 (40 wt% of Pt) and GV in Figure 3.2 C and A, respectively, it was evident that the deposition of platinum compromised the degree of graphitization of the pristine support surface. The effect of Pt deposition on the support was observed with an increase in the order of defect most likely due to surface oxidation. However, the presence of the indicative G'-band confirmed interactions of graphene layers which remained characteristics of a graphite structure. Therefore, the order of defect alone was inadequate to determine the supported catalysts degree of graphitization after Pt deposition as shown in Figure 3.2 D (0.999 and 1.003 for V40 and GV40, respectively).
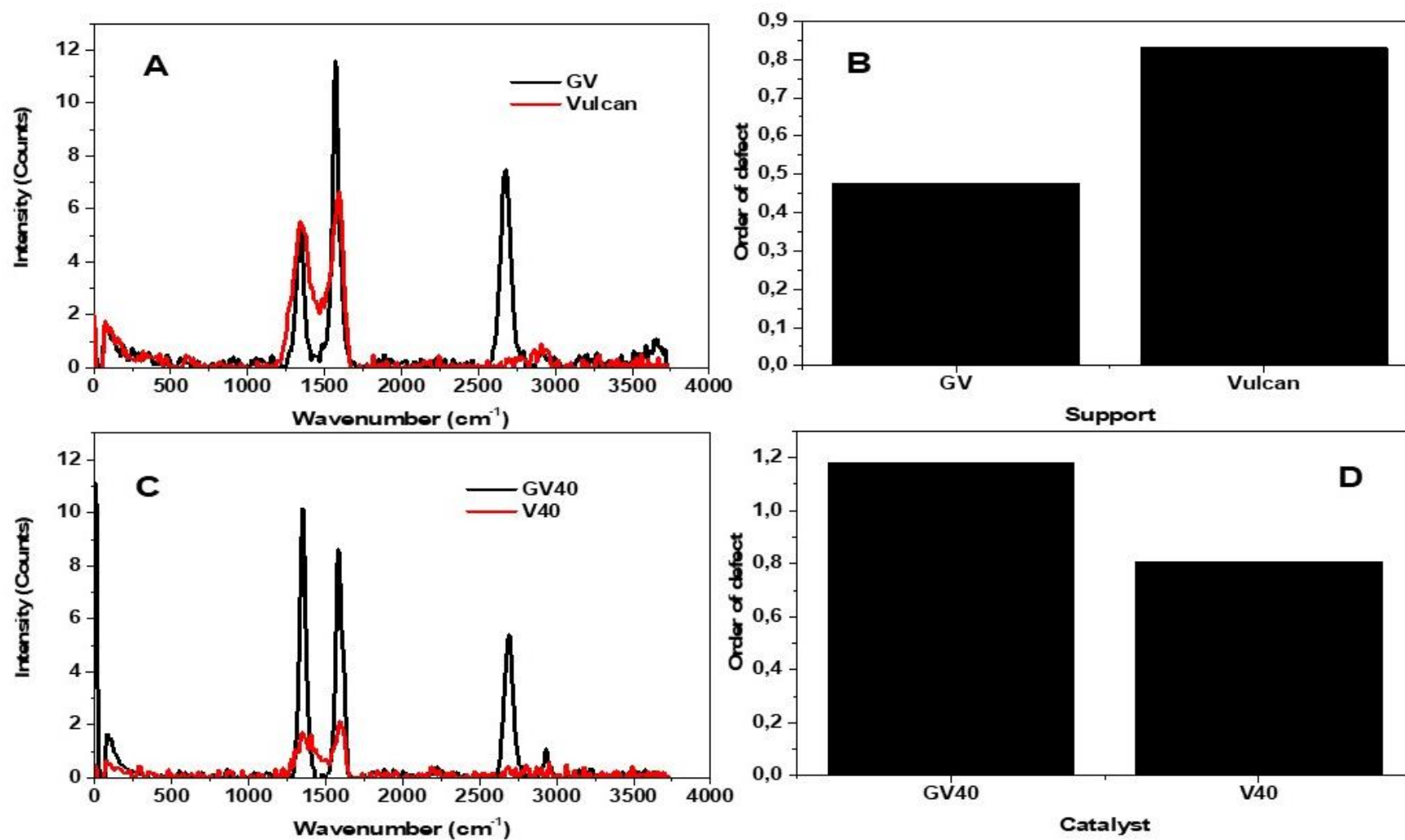
Figure 3.2: A) Raman spectra of supports; B) order of defect of supports; C) Raman spectra of supported catalysts; D) order of defect of supported catalysts.

3.2. Fourier transform infrared spectroscopy.

FTIR analysis was used to study the conformation of attached ionomer (Aquivion) onto the supported catalyst in a qualitative manner. The characteristic functional groups of the as-received Aquivion were observed in the FTIR spectrum at atmospheric conditions. Six bands were observed within the wavenumber range of 800- 1500 cm^{-1} as shown in the Figure 2.3 and Table 2-2. The FTIR spectra of solids (supported catalyst and solid Aquivion) suspended in the catalyst slurry, confirmed the presence and attachment of Aquivion molecules onto the supported catalyst. Figure 3.3 shows the FTIR spectrum of as-received GV40 compared to the air-dried catalyst slurry FTIR spectrum which showed adsorbed Aquivion molecules onto GV40. Each band was studied to investigate the changes in the FTIR spectrum of Aquivion due to either the support (GV or Vulcan) or platinum on the support.
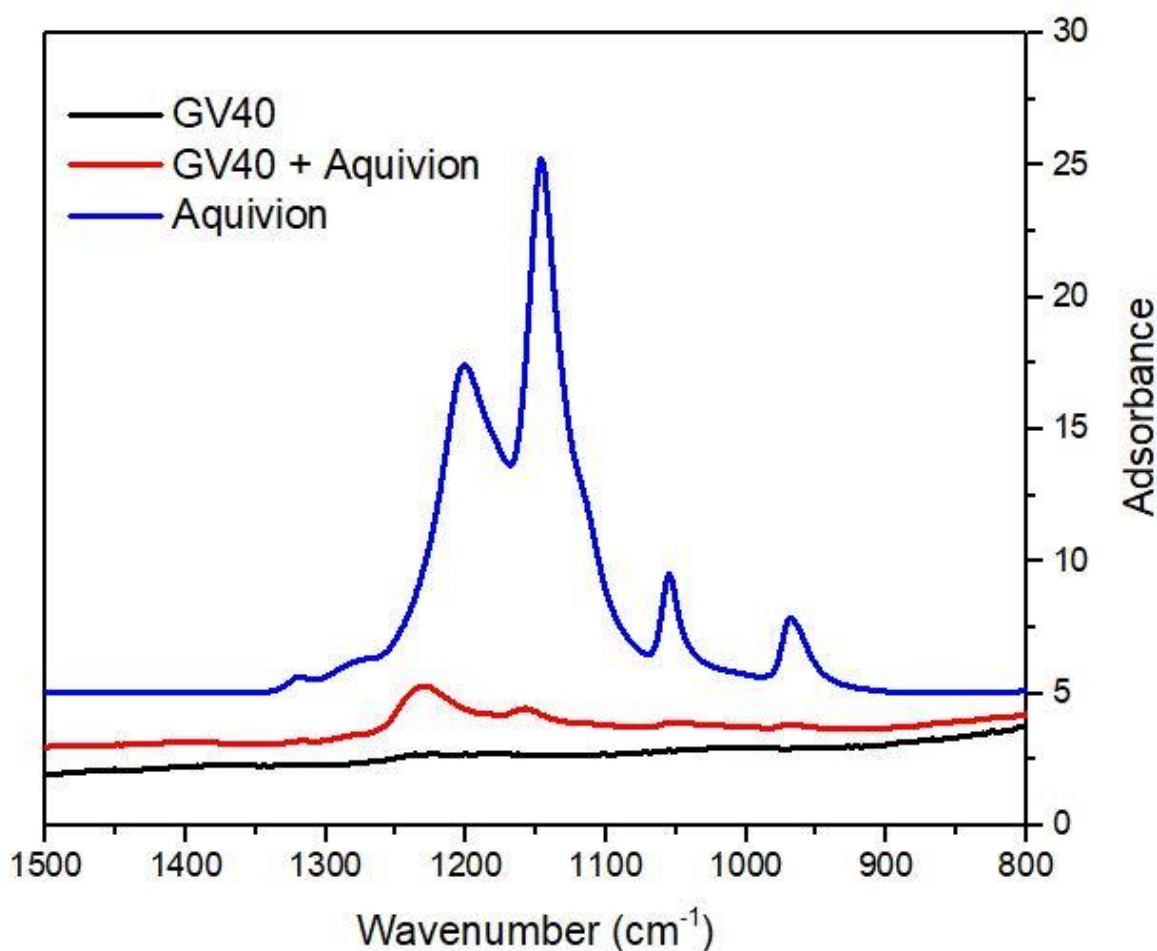
Figure 3.3: FTIR spectra of as-received GV40 and GV40 + aquivion.

3.2.1. FTIR spectra analysis (carbon support and supported catalyst)

The adsorption bands of the adsorbed ionomer were studied. Each band was assigned to its respective functional group (refer to Table 2-2). The changes of Aquivion bands on Vulcan and GV were compared with and without the catalyst.

3.2.1.1. $V_{as}(CF_3)$ band and $V_{as}(SO_3^-)$ band at 1320 cm^{-1} and 1280 cm^{-1}, respectively

The $V_{as}(CF_3)$ functional group is at the end of hydrophobic backbone of Aquivion and is observed at 1320 cm^{-1} in the Aquivion FTIR spectrum. The perfluoro sulfonic acid functional group, $V_{as}(SO_3^-)$, at 1280 cm^{-1}, is the side chain of the Aquivion molecule which is hydrophilic. These two bands are shown in Figure 3.4.
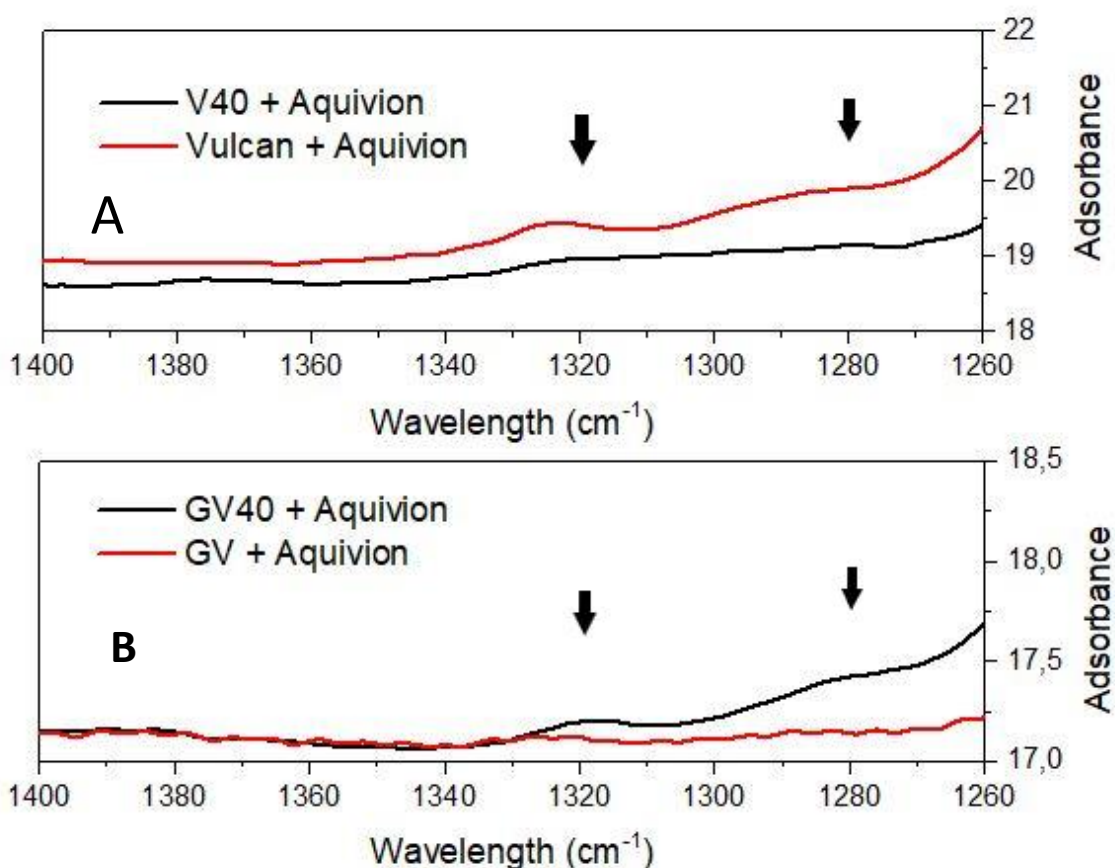
Figure 3.4: $V_{as}(CF_3)$ and $V_{as}(SO^{3-})$ bands FTIR spectra.

The intensity of the $V_{as}(CF_3)$ band decreased significantly in the presence of more hydrophobic GV (Figure 3.4 B) compared to less hydrophobic Vulcan alone (Figure 3.4 A). This significant drop in $V_{as}(CF_3)$ band intensity could be due to a chemisorption of CF$_3$ unto the hydrophobic support to form a compact hydrophobic surface (Andersen *et al.*, 2014).

No V_{as} CF$_3$ chemisorption occurred between Vulcan + Aquivion nor V40 + Aquivion, likely due to the repulsive force between the relatively hydrophilic Vulcan and V_{as}(CF$_3$) present in the hydrophobic backbone. However, the band in the Vulcan + Aquivion spectra shifted to a higher wavelength, likely due to the shortening (rather bending) of the V_{as} CF$_3$ bond. The addition of Pt onto GV, decreased the support's degree of graphitization on the surface, making it less hydrophobic and less interactive with the hydrophobic V_{as}(CF$_3$). Therefore, resulting in the small V_{as}(CF$_3$) band in the GV40 FTIR spectrum in Figure 3.4 B. The V_{as}(CF$_3$) band decreased with increasing hydrophobicity of the supported catalyst (showing interactions between V_{as}(CF$_3$) and the hydrophobic support) and slightly shifted to a higher wavenumber with increasing hydrophilicity of the supported catalyst such as V40 and Vulcan.

The V_{as}(SO$_3^-$) band at 1280 cm^{-1} was not pronounced on GV in Figure 3.4 B. When smoothed, the bands were visible as shown in Figure 3.5. In the case of V40 and Vulcan, V_{as}(SO$_3^-$) showed strong interactions with Pt (the V_{as}(SO$_3^-$) flattened in the V40 + Aquivion spectra) while the band remained present in the ionomer-Vulcan.
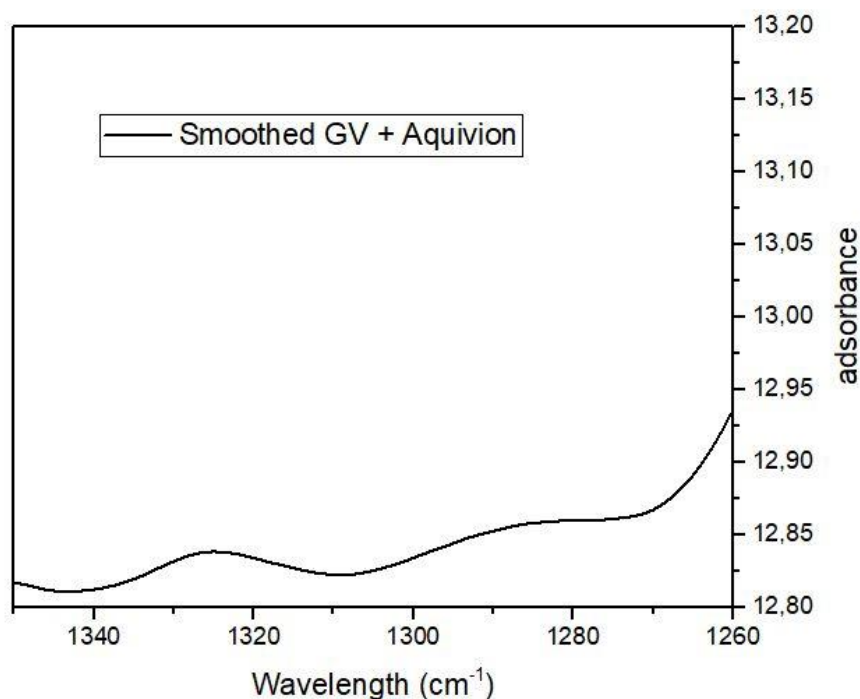
Figure 3.5: Smoothed V_{as}(CF$_3$) and V_{as}(SO^{3-}) bands in the GV + Aquivion FTIR spectra.

Therefore, V_{as}(SO$_3^-$) showed strong interactions with Pt, this was observed with the flattening of the band in the presence of Pt.

3.2.1.2. $V_{as}(CF_2)$ band and $V_s(CF_2)$ band at 1199 cm^{-1} and 1143 cm^{-1}, respectively

The asymmetric and symmetric CF$_2$ bonds are present in the hydrophobic backbone of Aquivion molecule and have the highest absorbance in Aquivion FTIR spectrum as shown with the inset in Figure 3.6.
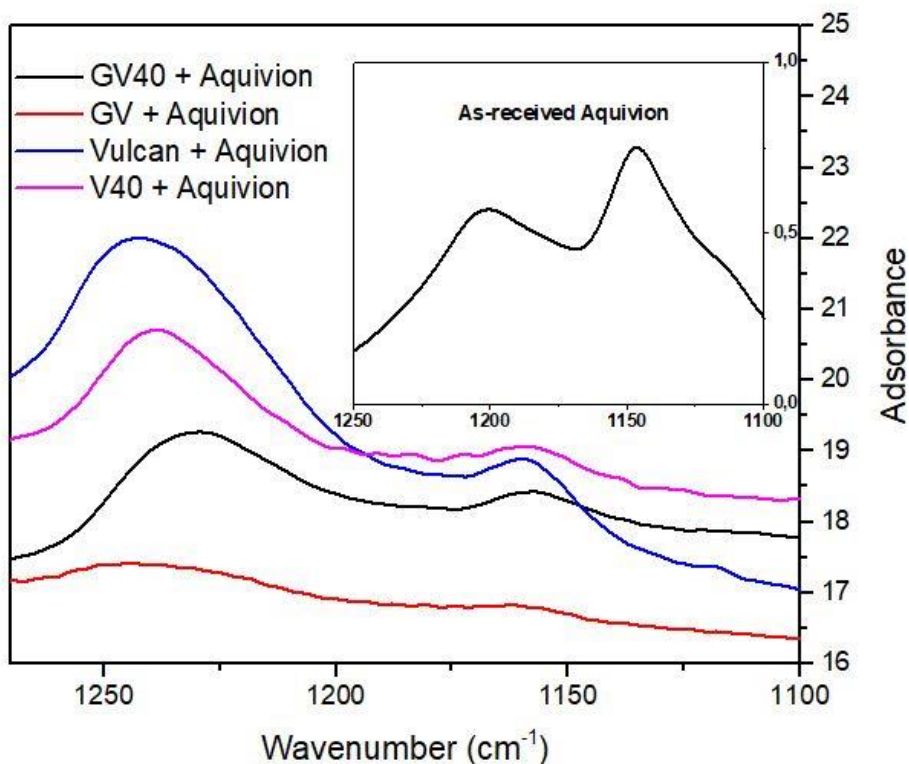
Figure 3.6: FTIR spectra of the asymmetric and symmetric CF$_2$ bands.

The $V_{as}(CF_2)$ bands of the supports (Vulcan and GV) with Aquivion shifted approximately 44 cm^{-1} to higher wavenumbers. With the addition of Pt, the $V_{as}(CF_2)$ band shifted approximately 35 cm^{-1} higher than the characteristic wavenumber of $V_{as}(CF_2)$ in pure Aquivion (1199 cm^{-1}). This indicated a strong interaction between the carbon supports (Vulcan and GV) and $V_{as}(CF_2)$ resulting in the bending of the asymmetric bond C-F present in the backbone of Aquivion.

Similarly, the symmetric C-F bond present in the polytetrafluoroethylene backbone showed strong interaction with the supports (Vulcan and GV) by the significant drop in $V_s(CF_2)$ band intensity irrespective of the presence of Pt (refer to Figure 3.6). The band shifted to a higher wavenumber (approximately 17 cm^{-1}) indicating that the symmetric C-F bond was shortened or became stronger.

3.2.1.3. $V_s(SO_3^-)$ band and $V_s(C\text{-}O\text{-}C)$ band at 1056 cm^{-1} and 969 cm^{-1}, respectively

The symmetric S-O bond in the sulfonic acid of the side chain showed a strong interaction with Pt as the $V_s(SO_3^-)$ band flattened in the presence of Pt (Figure 3.7). No shift was observed, and the band remained present in the absence of Pt as shown in Figure 3.7. The $V_s(SO_3^-)$ band was also seen in the GV + Aquivion spectra when smoothed as shown in Figure 3.8.
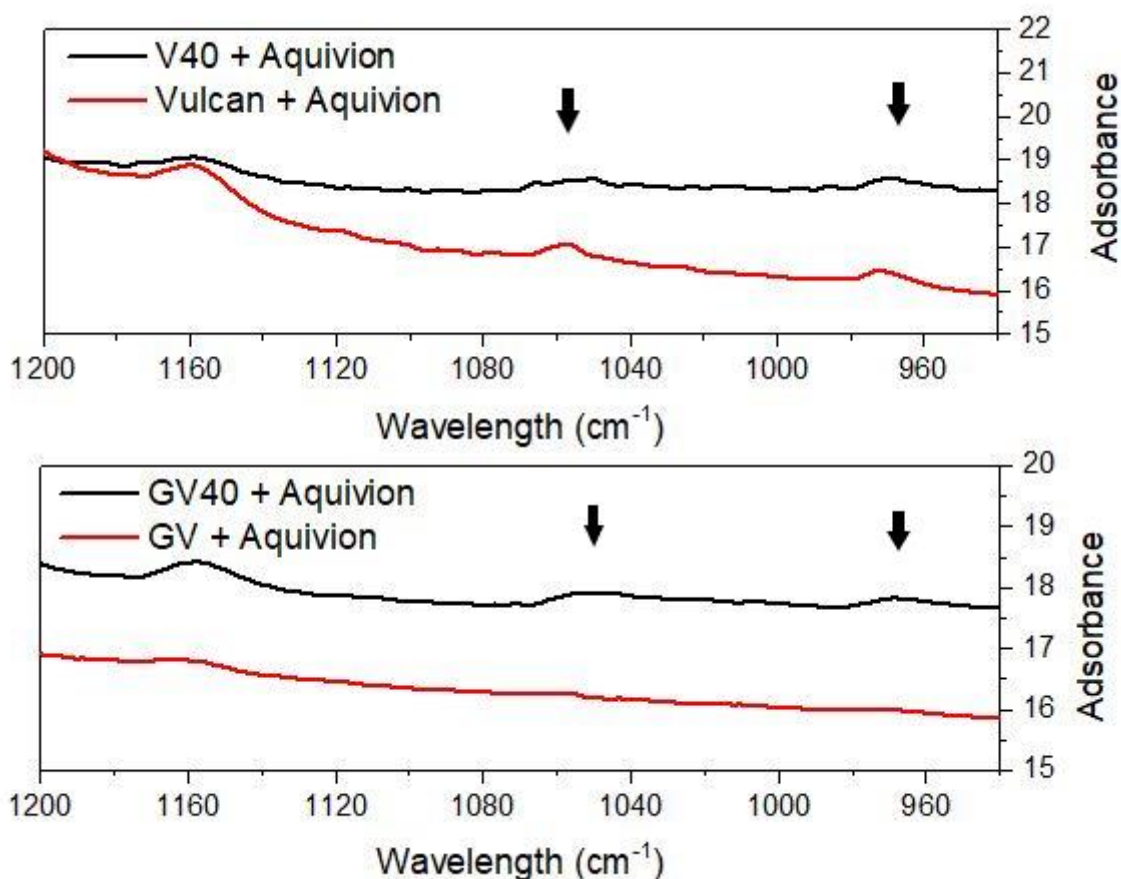
Figure 3.7: $V_s(SO_3^-)$ band and $V_s(C\text{-}O\text{-}C)$ band FTIR spectra.

The symmetric C-O-C bond constitutes the link between the backbone and the side-chain of Aquivion molecule. The stretching of C-O-C bond shifted slightly to higher wavenumbers in the absence of Pt, yet remained at its characteristic wavenumber in the presence of Pt. Therefore, no significant interactions were observed between the symmetric C-O-C band and the supported catalysts.
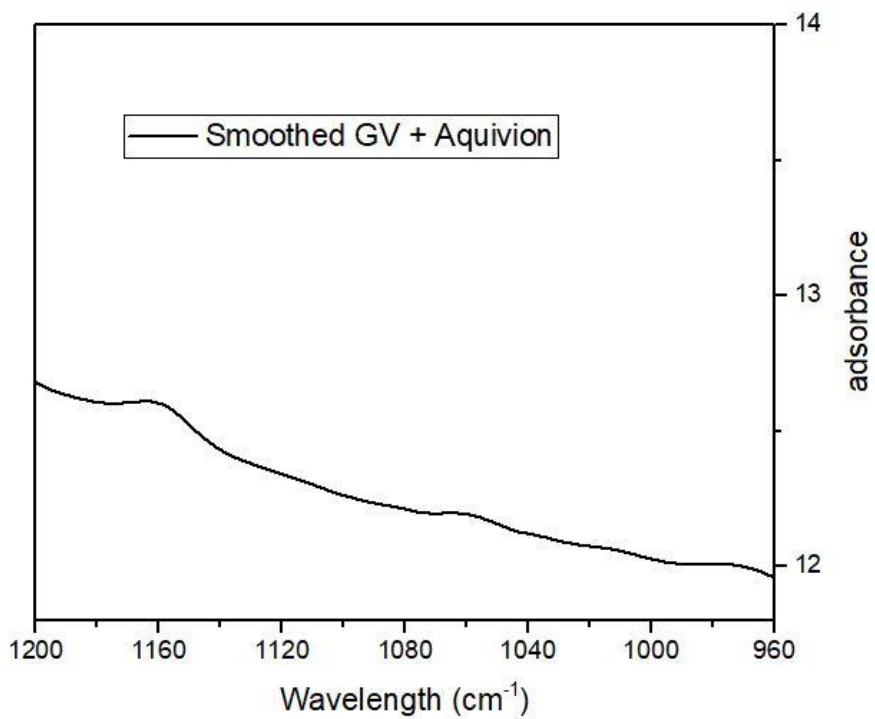
Figure 3.8: Smoothed $V_s(SO_3^-)$ band and $V_s(C\text{-}O\text{-}C)$ band in the GV + Aquivion FTIR spectra.

3.2.2. FTIR spectra analysis (catalyst slurry preparation methods)

As described in Chapter 2, different methods were used to prepare the catalyst slurry; TDM, NDM, FDM and ASDM. The air-dried solids of the catalyst slurries prepared by TDM, NDM, ASDM and FDM were analysed with FTIR. The functional group bands were shifted to higher wavenumbers. However, no difference was observed in the spectra between the four methods as shown in Figure 3.9.
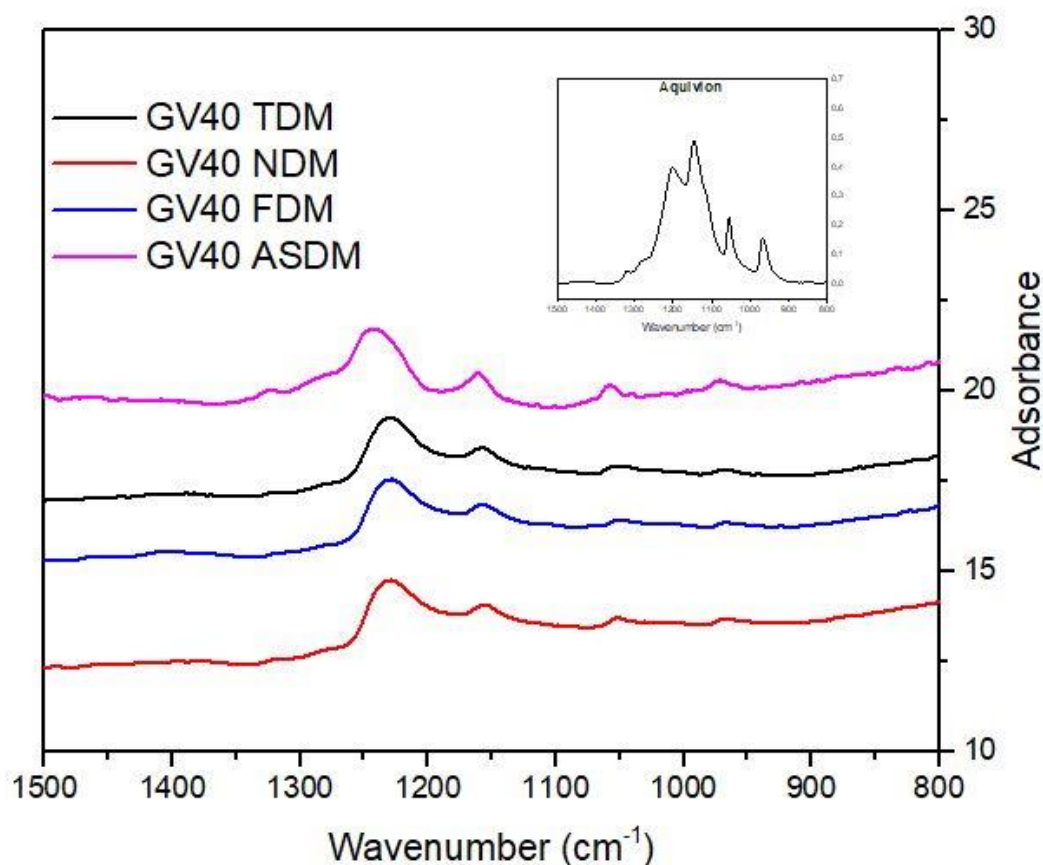
Figure 3.9: FTIR spectra of GV40 and Aquivion from different catalyst slurry preparation methods.

The attachment mechanism of Aquivion molecule onto the supported catalysts (GV40) was independent of the catalyst slurry preparation method, and FTIR was unable to quantify the amount of Aquivion attached. The mechanism of ionomer adsorption onto the supported catalyst depended on the support's degree of graphitization, and therefore hydrophobicity. Strong interactions were observed between the hydrophilic side-chain of Aquivion, Pt and the less hydrophobic Vulcan. Graphitized Vulcan showed strong interactions with the hydrophobic backbone of Aquivion. It can be concluded that Aquivion molecule coiled itself when interacting with carbon supported platinum catalyst, its hydrophilic side-chain pointed away from the hydrophobic GV to form more hydrophobic compact, while its main-chain (the backbone) pointed away from Vulcan to form more hydrophilic compact as illustrated in Figure 3.10.
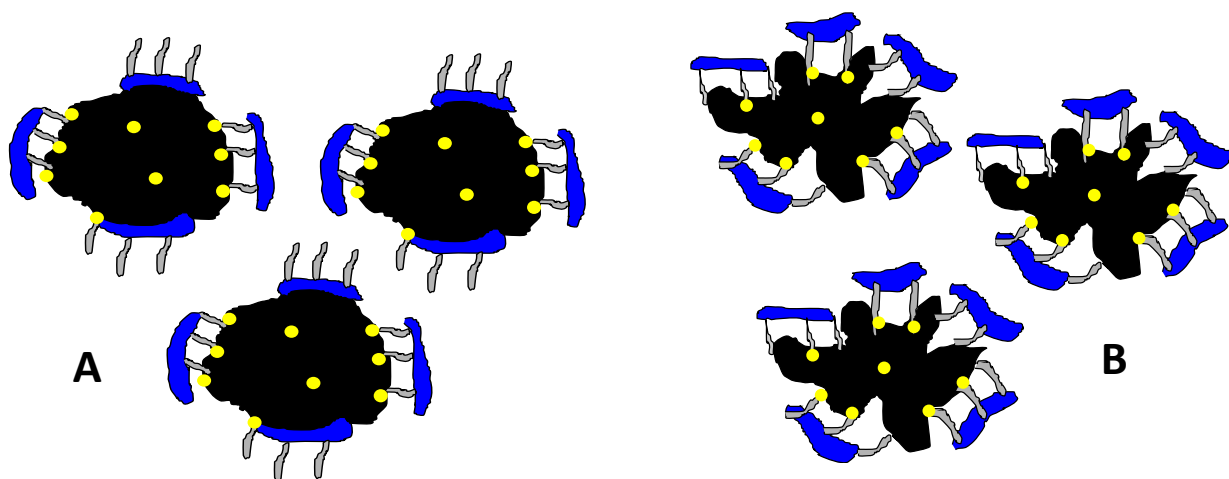
Figure 3.10: A) Attachment and orientation of Aquivion on GV40. B) Attachment and orientation of Aquivion on V40. Blue: Aquivion main-chain (PTFE); grey: Aquivion side-chain (PFSA); yellow: Pt; black: carbon support.

3.3. Scanning electron microscopy

SEM images (Figure 3.11) of the cross-sectional area of the catalyst layers were studied to determine their thicknesses which are summarised in Table 3-1. The targeted loadings for the anode and cathode were 0.1 $mg_{Pt}.cm^{-2}$ and 0.4 $mg_{Pt}.cm^{-2}$.

Table 3-1: Thicknesses of catalyst layers.

| CCM	Anode		Cathode	
	Loading (mg_{Pt}/cm^2)	Thickness (µm)	Loading (mg_{Pt}/cm^2)	Thickness (µm)
GV40 TDM	0.1116	5.70	0.3786	7.10
GV40 NDM	0.1141	6.40	0.4013	8.80
GV40 ASDM	0.1179	3.30	0.3849	9.50
GV40 FDM	0.1583	3.60	0.3962	6.40
V40 TDM	0.0953	2.40	0.3950	8.20
V40 NDM	0.1367	3.90	0.3625	12.9
V40 ASDM	0.1004	3.20	0.4867	12.0

V40 inks made thicker cathodic layers likely due to its lower density compared to GV40; to obtain targeted loadings, larger volumes of V40 were required than GV40. The catalyst slurry preparation methods with slower drying rate (TDM and FDM) produced MEAs with the thinnest cathodes. This indicated the potential for a wide protonic network and good electronic conductivity via tunnelling effect in these electrode structures (Andersen, 2016).

Figure 3.11 presents the SEM image of the cross-section of the catalyst coated membranes (CCM) with the thinnest cathode (GV40 FDM). The catalyst layers on each side of the three-layer membrane showed their porous structure which was studied and reported in Section 4. (Refer to Appendix A for more SEM images).
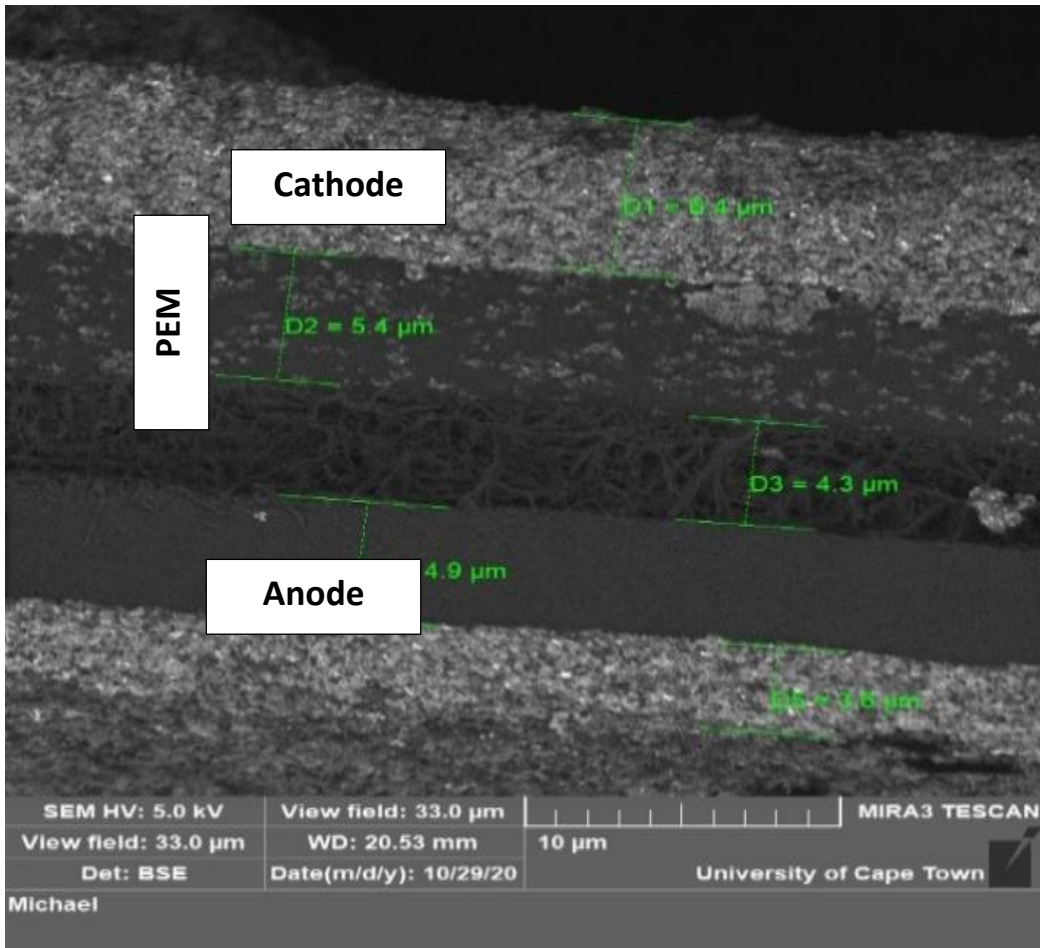
Figure 3.11: SEM image of a GV40 FDM CCM

3.4.   Mercury intrusion porosimetry

The catalyst layer structure in catalyst coated membranes (CCMs) were studied with a mercury intrusion porosimeter. The impact of the catalyst slurry preparation method on the pore size distribution of the catalyst layer was compared and studied.

A bimodal pore size distribution was considered; primary pores (2-20 nm) within the ionomer-supported catalyst agglomerates and secondary pores (>20 nm) between ionomer-catalyst agglomerates (100–300 nm) (Holdcroft, 2014). The ionomer-supported catalyst agglomerate size can be deduced by comparing the ratio between primary and secondary pores. The ionomer-supported catalyst agglomerates cluster to form ionomer-supported catalyst aggregates of 1–3 μm (Holdcroft, 2014).

The Vulcan particles (1.7 – 1.9 g/cm^3 Fuel Cell store) were less dense than GV particles (since graphite density is 2.3 – 2.7 g/cm^3). GV had a higher degree of graphitization (graphite-like structure) which indicated it was more structured and Vulcan was more amorphous. For a given mass to achieve a target loading, more V40 would be required compared to GV40, resulting in thicker V40 catalyst layers (Table 3-1).

Figure 3.12: Assumed particle of A) GV40 with a smaller surface area but dense B) V40 with a larger surface area and less dense.

Stevenson and Pattrick, (2017) compared the specific surface areas of V40 and G40 and found 237.1 m^2/g and 147.9 m^2/g, respectively.

3.4.1. Pore size distribution of GV40 MEAs

Figure 3.13 shows the pore size distribution of GV40 MEAs, two distinct regions were identified: the primary pores (2-20 nm) and the secondary pores (>20 nm). And the additional pore size distribution between 5-10 μm, was attributed to the pores between ionomer-supported catalyst aggregates (1–3 μm).
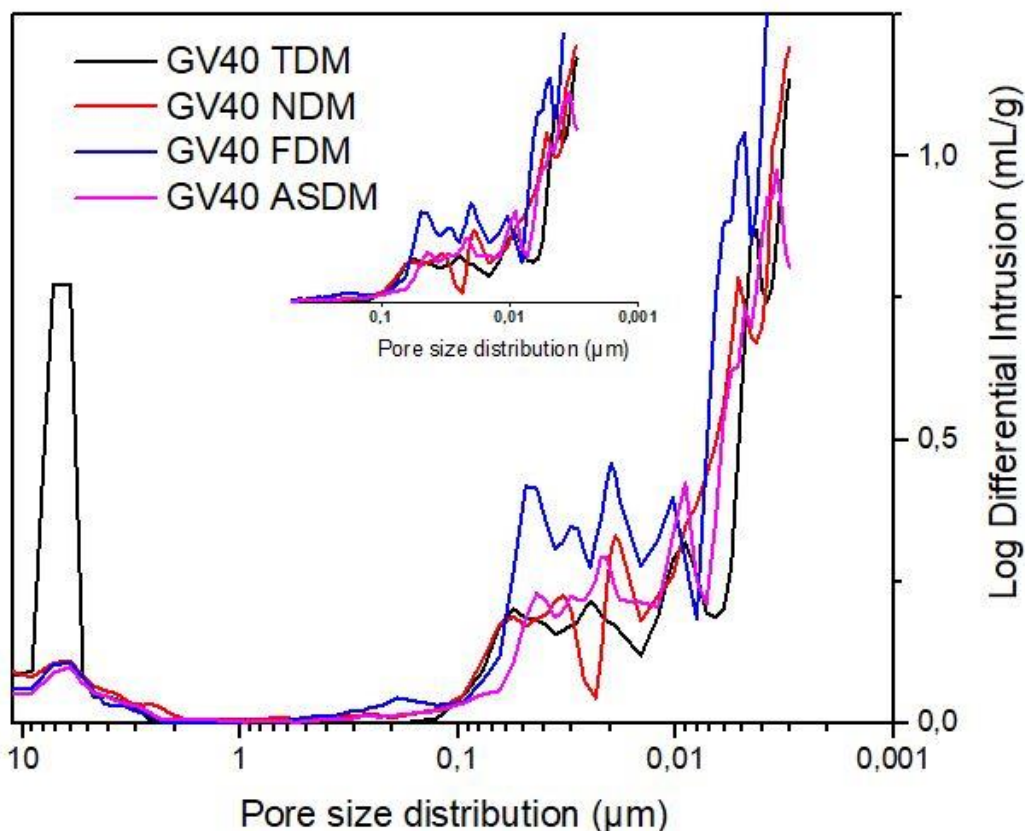
Figure 3.13: Pore size distribution of GV40 MEAs.

Primary and secondary pores were observed between 0-20 nm and 20-300 nm, respectively. The primary-secondary pore ratio of GV40 TDM (by comparing the heights of the peaks below 20 nm and the heights of the peaks above 20 nm) was the highest. This implied that the primary pores inside the agglomerates had a larger intrusion volume than the secondary pores between agglomerates. Therefore, this indicated the formation of larger ionomer-GV40 agglomerates by the TDM, within which primary pores provided a larger intrusion volume. The higher ratio of the pores between 5 and 10 µm (attributed to the space between aggregates) to the secondary pores designated that small ionomer-GV40 aggregates were formed by the TDM. Therefore, GV40 TDM catalyst layers consisted of larger ionomer-GV40 agglomerates (filled with more primary pores between GV particles) which clustered into smaller ionomer-GV40 aggregates with larger intrusion volume space between these. As shown in Figure 3.14; the large volume pores between aggregates provide channels for the transport of reagents and the product (water) improving the mass transport properties of the catalyst layers.
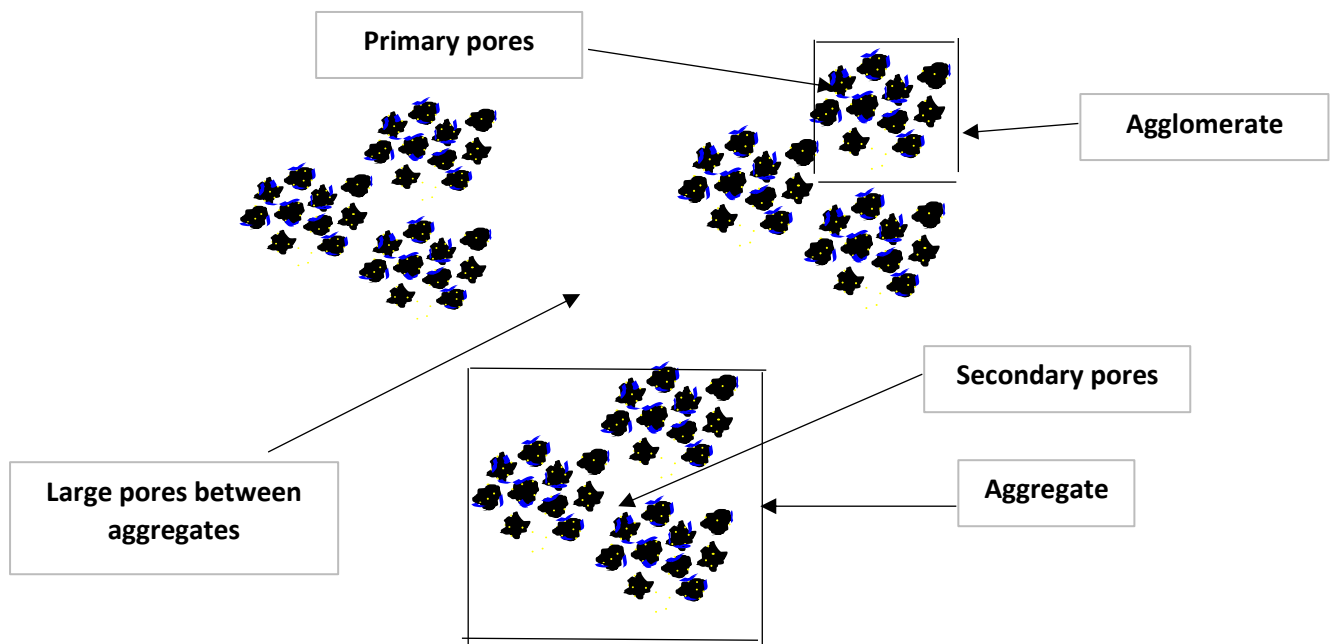
Figure 3.14: Illustration of ionomer-GV40 aggregates formed by the TDM. The aggregate is constituted of ionomer-GV40 agglomerates separated by secondary pores. Yellow dots: Pt particles; Black: GV; Blue: Ionomer

The GV40 FDM MEAs, had a smaller primary-secondary pores ratio compared to TDM MEAs indicating that the pores between GV40 particles and the pores between ionomer-GV40 agglomerates had similar intrusion volume. However, the presence of a pore size distribution between 100 nm and 300 nm signified a more heterogeneous distribution of voids between ionomer-GV40 agglomerates. The smaller ratio of primary to secondary pores of GV40 FDM when compared to GV40 TDM, also implied a smaller size of FDM ionomer-GV40 agglomerates. And the smaller ratio of the pores between 5 and 10 μm to the secondary pores indicated that the clustering of ionomer-GV40 agglomerates formed larger aggregates as shown in Figure 3.15.

Figure 3.15: Illustration of ionomer-GV40 aggregates formed by the FDM. Yellow dots: Pt particles; Black: GV; Blue: Ionomer.

Similar to FDM, both ASDM and NDM showed a smaller ratio of primary to secondary pores when compared to the TDM. However, the ASDM and NDM possessed a slightly higher ratio o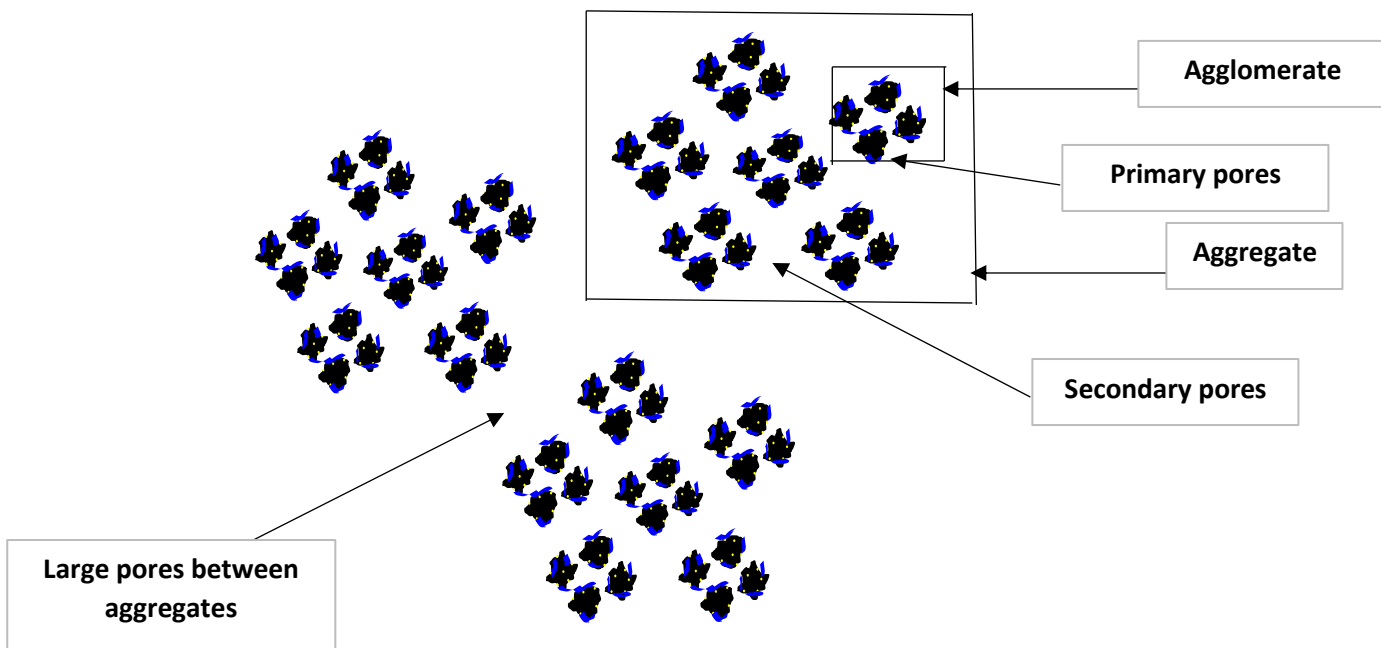f primary pores to secondary pores which indicated that their primary pores had a larger intrusion volume than their secondary pores. This implied that the ionomer-GV40 agglomerates produced by the ASDM and NDM were slightly larger than those produced by the FDM and smaller than those produced by the TDM.

The total intrusion volumes of GV40 catalyst layers are shown in Table 3-2. GV40 FDM catalyst layers showed the largest total intrusion volume.

Table 3-2: Total intrusion volume of GV40 catalyst layers.

GV40 TDM	GV40 NDM	GV40 FDM	GV40 ASDM
0.6368 mL/g	0.6559 mL/g	0.8349 mL/g	0.5640 mL/g

The total intrusion volume and the thickness of a catalyst layer depended on the size and distribution of ionomer-supported catalyst agglomerates and aggregates (the porosity of the catalyst layer). The total intrusion volume is the total accessible space within and between ionomer-supported catalyst aggregates (total space consisting of primary pores, secondary pores, and voids between aggregates).

In the case of GV40 TDM and GV40 FDM with cathode layer thicknesses of 7.10 μm and 6.40 μm, respectively, designated a porous and thin catalyst layer (good mass transport properties). This was possible with:

1. Large aggregates formed by small agglomerates with large intrusion volume distributed in the secondary and primary pores as in the case of GV40 FDM. The small thickness of the catalyst layer was due to small spaces between aggregates.
2. Small aggregates formed by large agglomerates, with large intrusion volume primary pores and large spaces between aggregates (as in the case of GV40 TDM).

It is possible that the ASDM and NDM produced large aggregates formed by small ionomer-GV40 agglomerates. The poor dispersion of the ionomer likely resulted in the formation of large ionomer clusters which settled between GV40 aggregates (possibly decreasing the mass transport properties of the catalyst layers).

3.4.2. Pore size distribution of V40 MEAs

Similar bimodal pore size distribution was observed with V40 MEAs as shown in Figure 3.16. V40 MEAs however, showed a higher ratio of pores between 5-10 µm to secondary pores indicating a large intrusion volume between aggregates. It is therefore suggested that V40 MEAs possessed smaller ionomer-supported catalyst aggregates than GV40 MEAs.
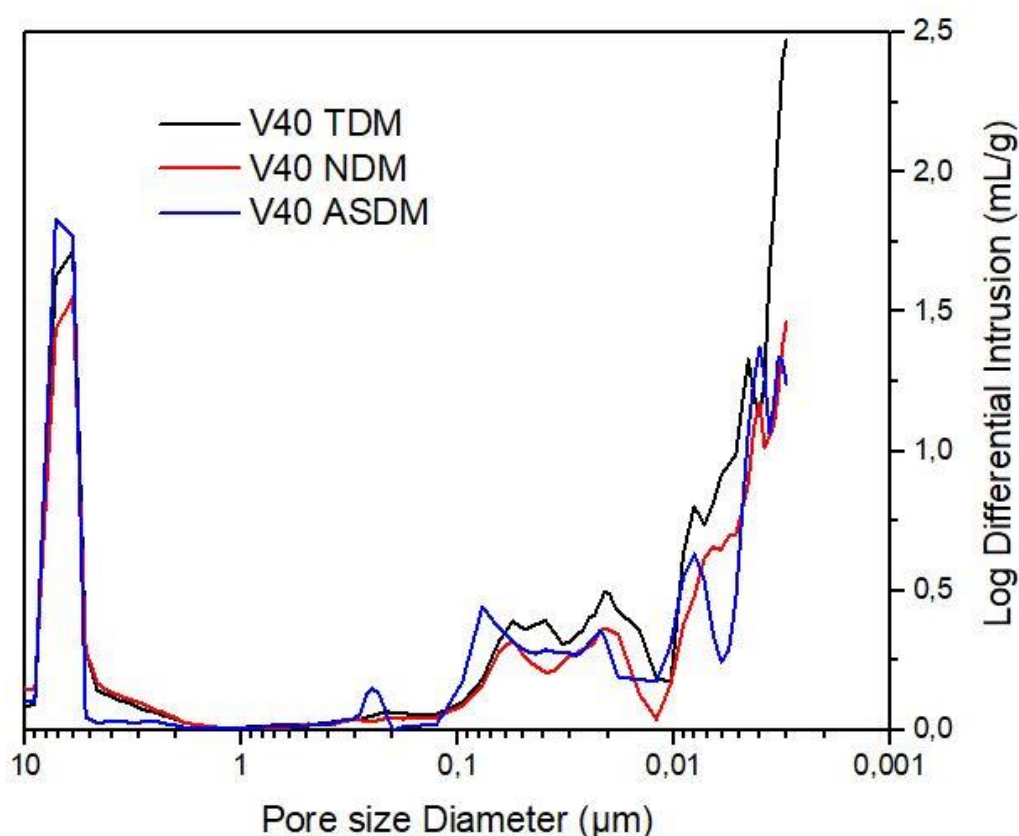

Figure 3.16: Pore size distribution of V40 MEAs.

The ratio of primary pores to secondary pores of V40 TDM catalyst layers was the highest. This indicated that there was more pore volume inside the ionomer-V40 agglomerates resulting in the formation of larger agglomerates. In contrast, in the case of ASDM, the ratio of primary pores to secondary pores was the smallest, signifying larger pore intrusion volume between agglomerates and smaller intrusion volume inside the agglomerates. The additional pore size distribution between 200 nm and 300 nm for V40 ASDM catalyst layers, indicated that the sizes of voids between agglomerates varied nonuniformly. Unlike V40 TDM and V40 NDM, which followed a similar trend in their secondary pore size distributions. From their respective ratio of primary pores to secondary pores, it was suggested that TDM produced the largest ionomer-V40 agglomerates, followed by the NDM and the ASDM.

No significant difference was observed in their ratios of 5 and10 µm pores to the secondary pores, therefore the ionomer-V40 aggregates had possibly a similar size irrespectively of the catalyst slurry preparation method. This may be due to the strong interaction between the ionomer and the less hydrophobic V40.

Table 3-3 shows the total intrusion volumes of V40 catalyst layers, which possessed larger total intrusion volumes than GV40 catalyst layer, likely due to the highly porous structure of V40 and its lower density which required thicker layers to achieve similar loading.

Table 3-3: Total intrusion volume of V40 catalyst layers.

V40 TDM	V40 NDM	V40 ASDM
1.2770 mL/g	1.0490 mL/g	1.1029 mL/g

TDM produced V40 a catalyst layer with the largest total intrusion volume with the smallest thickness; 8.20 µm (Table 3-1). This was due to the large agglomerates formed, filled with secondary pores, these agglomerates clustered to form smaller aggregates with smaller spaces between these which resulted in a porous and thin (good mass transport properties) catalyst layer. In contrast, the total intrusion volume, and the large thickness of V40 NDM indicated the presence of smaller agglomerates with large intrusion volume secondary pores between agglomerates. Therefore, NDM produced a thick and porous V40 catalyst layer with smaller agglomerates and large intrusion volume pores between agglomerates. In the case of ASDM, the total intrusion volume was reduced due to the poor interaction between the ionomer and V40 which resulted in the formation of large clusters of ionomers which settled between V40 aggregates (possibly impacted the mass transport properties of the catalyst layer).

Figure 3.17 illustrates the different sizes of ionomer-V40 agglomerates formed by various catalyst slurry preparation methods. Where A shows the clustering of larger ionomer-V40 agglomerates to form smaller aggregates formed by TDM, which indicate good mass transport properties through the pores (predominant through the pores between aggregates and primary pores). And B shows larger aggregates formed by smaller ionomer-V40 agglomerates produced by NDM. The large voids between aggregates and the secondary pores between agglomerates provided pathways for the transport of reagents and the product.
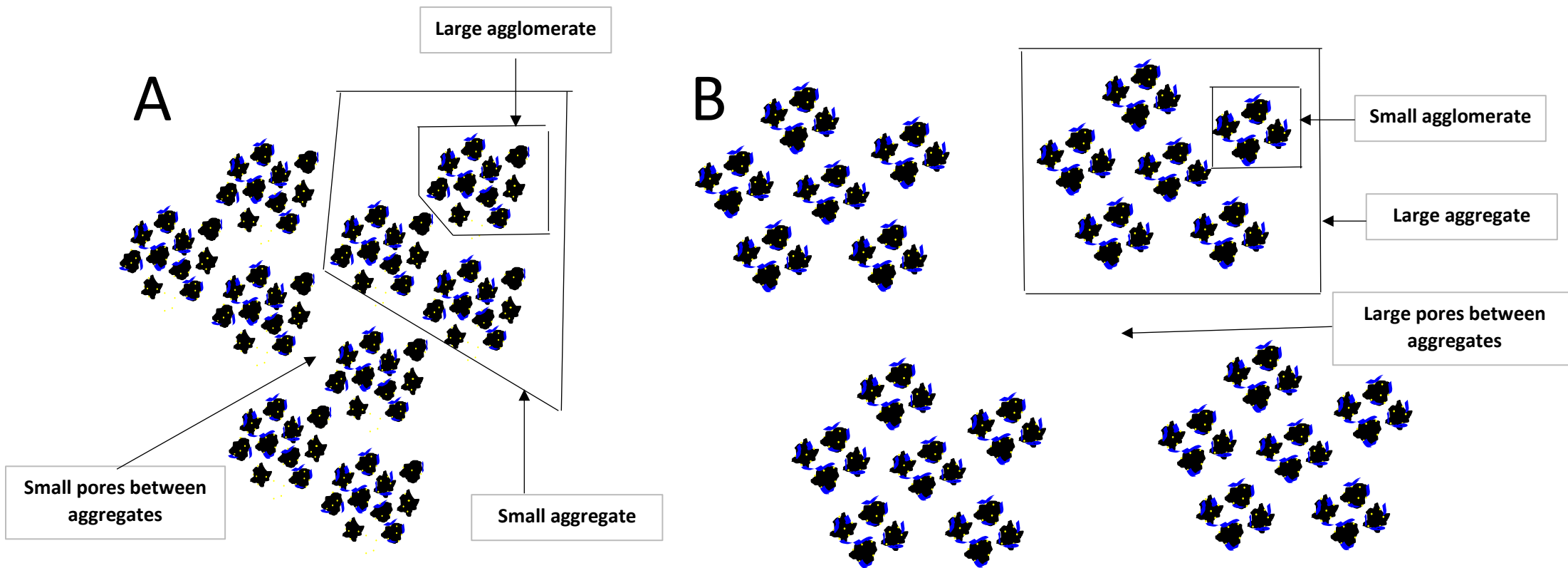
Figure 3.17: Illustrations of ionomer-V40 agglomerates and aggregates: A) larger agglomerates and small aggregates formed by TDM, B) small agglomerates and large aggregates formed by NDM.

In summary, the degree of graphitization of GV40 was higher than V40 which was indicative of their surface properties; V40 was less hydrophobic. The degree of graphitization of the supported catalyst influenced the adsorption and reconfiguration of the amphiphilic ionomer. The hydrophilic side-chain (PFSA) of the ionomer showed strong interactions with Vulcan (forming hydrophilic compacts) and Pt, while strong interactions were observed between GV and the hydrophobic backbone of Aquivion (forming hydrophobic compacts). And the attachment mechanism of ionomer onto the supported catalyst did not depend on the catalyst slurry preparation method as shown in Figure 3.9.

Slow drying rate methods such as TDM and FDM produce thinner GV40 catalyst layers which indicated a wide protonic network. TDM produced the thinnest V40 cathode while NDM and ASDM produced catalyst layers with large thicknesses as shown in Table 3-1.

The pore size distribution of GV40 TDM catalyst layers indicated the formation of large agglomerates which clustered to smaller aggregates with large volume space between aggregates. The total intrusion volume (0.637 mL/g) and the small thickness of a GV40 (7.10 μm) catalyst layer indicated the formation of a thin and porous layer. The pores between ionomer-GV40 aggregates formed during TDM possibly improved the mass transport of the catalyst layer, reagents and water could easily move through the catalyst layer by diffusion and especially by capillary movement.

In the case of NDM and ASDM, it was deduced that smaller ionomer-GV40 agglomerates were formed with more secondary pores which resulted in larger aggregates. However, due to the hydrophobic nature of GV40 and the short contact time (during water removal) between the ionomer and GV40 during the NDM and ASDM, poor interfaces were created between GV40 and the ionomer. This resulted in large GV40 aggregates which weakly interacted with possibly formed thicker ionomer clusters; therefore, thicker GV40 catalyst layers were formed by NDM and ASDM.

V40 NDM and V40 ASDM catalyst layers consisted of smaller agglomerates with large intrusion volume secondary pores which likely led to the formation of large aggregates. This resulted in the formation of catalyst layers with the largest thickness. However, a strong interaction between the ionomer and V40 was expected due to the surface properties of V40 (less hydrophobicity and high porosity). Nonetheless, the fast-drying rate of ASDM limited interaction between the ionomer and V40.

These aggregate structures of the catalyst layers were studied by a Tosca Series Atomic Force Microscopy (AFM) and the catalyst layers topography images are shown in Figure 3.18.
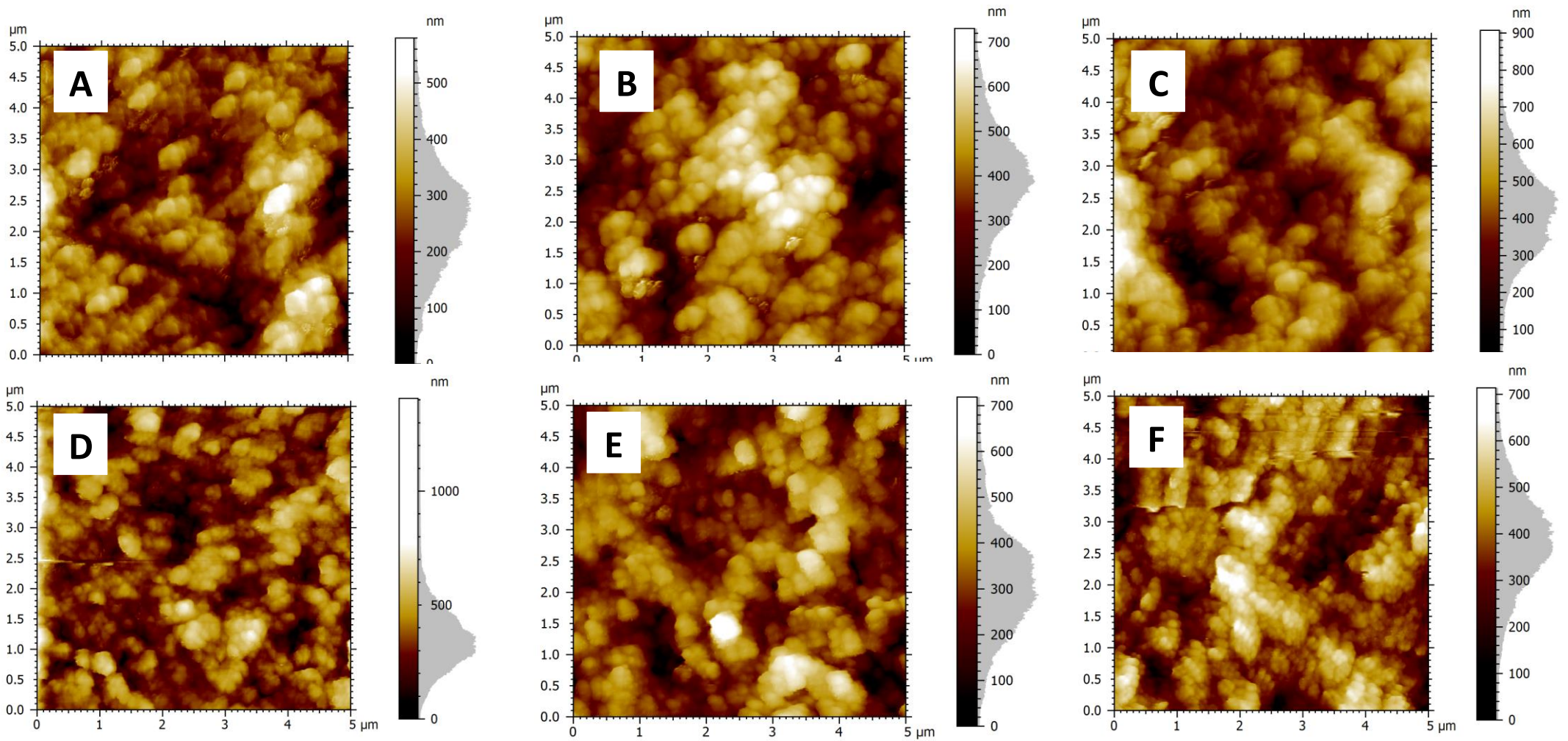
Figure 3.18: AFM images; A) GV40 TDM; B) GV40 NDM; C) GV40 ASDM; D) V40 TDM; E) V40 NDM and F) V40 ASDM.

61

Larger GV40 aggregates formed by NDM and ASDM (as shown in Figure 3.18 B and C) clustered to form larger lumps with small spaces between these. Unlike GV40 TDM (Figure 3.18 A), which showed the presence of smaller aggregates.

For V40, similar aggregate size to GV40 TDM was observed, however, V40 ASDM showed small V40 aggregates clustered to form larger lumps with smaller spaces in between (Figure 3.18 F). While it was evident that V40 NDM and V40 TDM small aggregates (Figure 3.18 D and E) formed into a similar porous structure.

Chapter 4 In-situ electrochemical evaluation

This chapter presents the in-situ electrochemical evaluations of the MEAs, made using various slurry preparation methods, including:

A. Cyclic voltammetry: to determine the electrochemical surface area (ECSA) of the MEAs.
B. Polarization and power curves: to determine and compare the performance of the MEAs under specified humidity conditions.
C. Electrochemical impedance spectroscopy: to measure the charge transfer resistances.

The electrochemical properties of the MEAs produced by different catalyst slurry preparation methods, were compared to evaluate the impact of the drying step during catalyst slurry preparation on MEA performance.

4.1. Electrochemical surface area

Cyclic voltammetry was run in-situ by controlling the parameters described in Table 2-4. The charge generated from hydrogen adsorption onto the Pt surface was determined from the voltammogram and the ECSA was calculated by using Equation 1.5. The characteristic peaks of Pt/C cyclic voltammogram are shown in Figure 4.1.
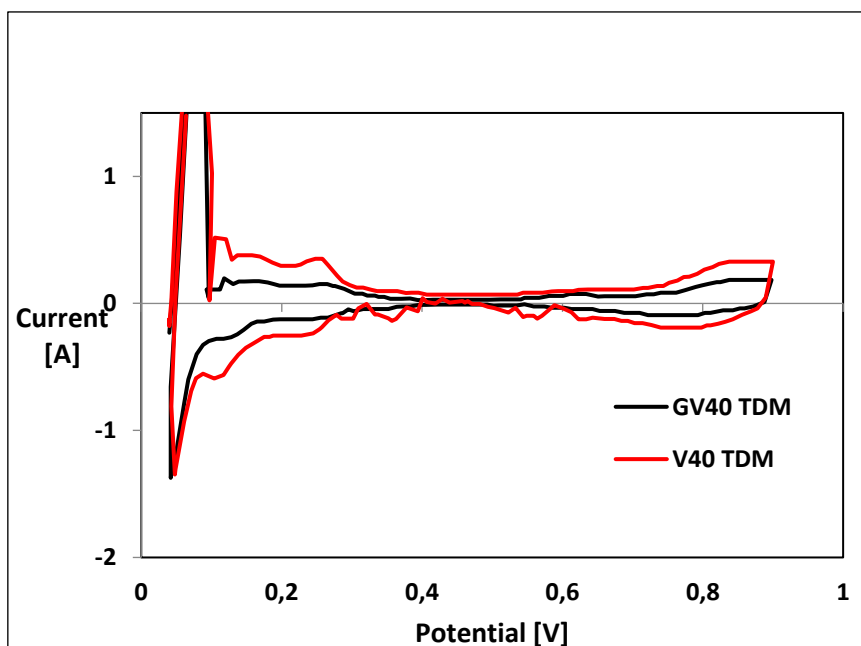

Figure 4.1: Cyclic voltammograms of GV40 TDM and V40 TDM MEAs.

The beginning of life (BoL) ECSAs from the charge generated by H-adsorption, were calculated and are presented in Table 4-1.

Table 4-1: BoL ECSAs of V40 and GV40 MEAs.

MEAs	Loading (mg_{Pt}/cm^2)		Active area (cm^2)	ECSA (m^2/g_{Pt})
	Anode	Cathode		
GV40 TDM	0,1141	0,3661	25	58,20
GV40 NDM	0,1132	0,3853	25	45,08
GV40 FDM	0,1074	0,3902	50	56,42
GV40 ASDM	0,1417	0,3900	25	47.69
V40 TDM	0,0992	0,4299	25	62,98
V40 NDM	0,0913	0,3613	25	64,56
V40 ASDM	0.1001	0,4867	25	54,94

V40 MEAs showed higher BoL ECSA than GV40 MEAs due to the porous structure of V40 and the larger spaces between V40 aggregates (deduced by the high ratio of 5 – 10 µm pores to the secondary pores, refer to Chapter 3 section 4) which improved Pt sites accessibility. The larger spaces between V40 aggregates allowed the transport of water which increased the protonic connectivity and resulted in high BoL ECSAs.

TDM and FDM produced the highest BoL ECSAs for GV40 MEAs, likely due to an optimal ionomer distribution and porous structure of the catalyst layer, increasing proton transport and access to Pt sites.

In the cases of ASDM and NDM, a poor distribution of the ionomer was likely achieved due to the rapid drying rate (during ASDM) and the absence of drying step in the NDM. The hydrophobic surface of GV40 likely agglomerated in the presence of water and the ionomer clustered to form large ionomer aggregates with poor ionomer-GV40 interface. This decreased the protonic connectivity and resulted in isolated Pt sites and low BoL ECSAs. These are also seen in the AFM images (Figure 3.19) indicating large clustered packed carbon aggregates.

The BoL ECSAs of V40 MEAs produced by TDM and NDM were markedly similar. This was possibly due to the large interface created by the ionomer and V40 by the interaction of the ionomer to the less hydrophobic Vulcan. The favourable ionomer/catalyst distribution ensured protonic connectivity and access to Pt sites as illustrated in Figure 4.2. Due to poor ionomer distribution during ASDM, lower BoL ECSA was observed.

The BoL ECSA of GV40 and V40 MEAs depended on the ionomer dispersion and the large intrusion volume pore distribution in the catalyst layers. The large ionomer-supported catalyst

interface (shaped by the preparation methods and nature of the support) and the water transport efficiency (via water channels) ensured protons transport to active Pt sites and resulted in high BoL ECSAs.
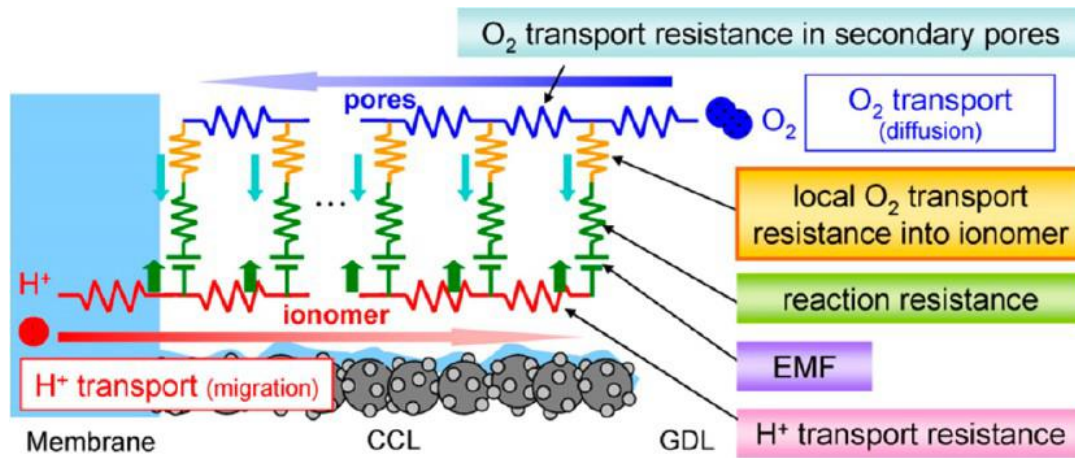

Figure 4.2: Steady-state 1-D transport model of cathode catalyst layer (Holdcroft, 2014).

4.2. Polarization and power curves

Performance tests consisted of current-voltage polarization measurement under three different RH conditions as described in Table 2-4. GV40 and V40 MEAs prepared by different catalyst slurry preparation methods were compared to elucidate the effect of the drying step on the MEA performance.

4.2.1. GV40 MEAs performance

The respective polarization and power curves are shown in Figure 4.3.

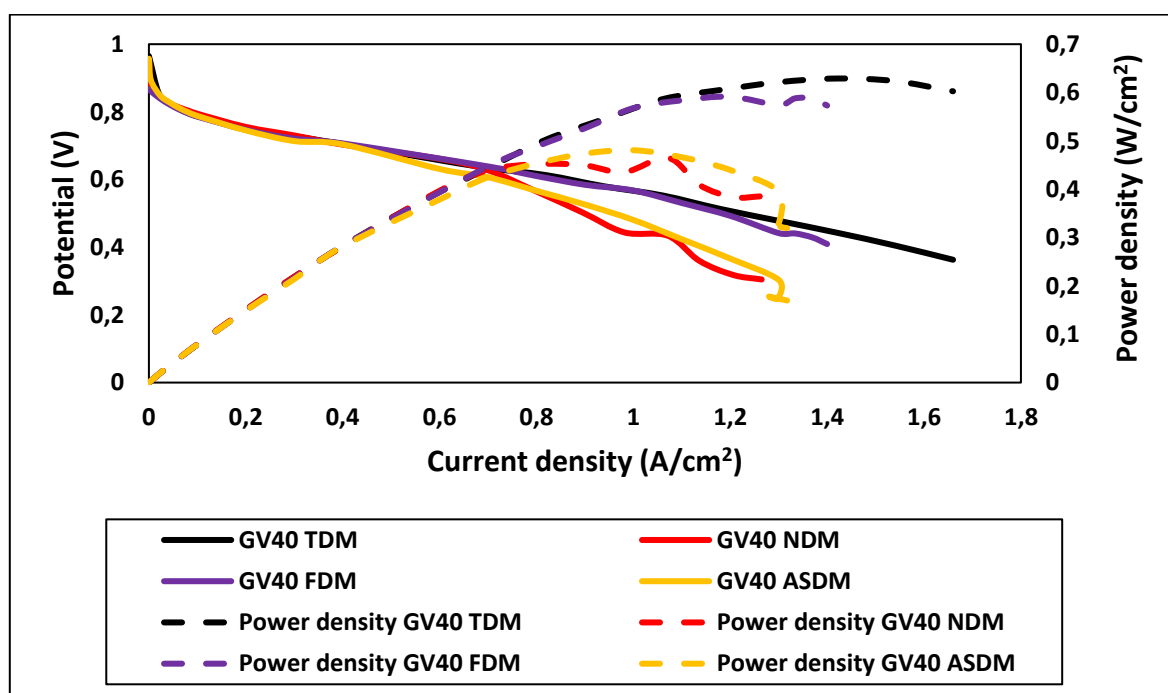*Figure 4.3: Polarization and power curves of GV40 MEAs under 74% RH.*

The GV40 MEAs showed similar performance in the activation region (0-0.2 A.cm^{-2}) and started deviating in the ohmic (0.2-1.2 A.cm^{-2}) to the mass transfer region (>1.2 A.cm^{-2}), with only GV40 TDM reaching 1.6 A.cm^{-2}. The ohmic resistance primarily caused by resistance from the membrane electrolyte and the ionomer in the catalyst layers. The protons produced by the HOR in the anode, move to the cathode via the membrane electrolyte. Optimal amount of moisture in the membrane electrolyte ensures optimal proton conductivity, while excessive amount of water will cause the membrane to swell (high ionic resistance) and deficiency of water will decrease the proton conductivity of the membrane (high ionic resistance) (Kim *et al.*, 2016). However, the ionomer in the catalyst layers retains water (and provide continuity of proton conductivity) and the pores in the catalyst layers constitute channels for the transport of water. Therefore, having used the same membrane electrolyte for all MEAs, it was assumed that the differences observed in the ohmic region, were due to the ionomer distribution (large

ionomer-supported catalyst interfaces, thicknesses of ionomer layers) and the capacity to keep the membrane hydrated.

The similarity of GV40 TDM and GV40 FDM performances in the ohmic region designated a large ionomer-GV40 interface which improved the protonic connectivity in the catalyst layers and the catalyst layers capacity to hydrate (water transport) the membrane. These large ionomer-supported catalyst interfaces formed during TDM and FDM, resulted in larger BoL ECSAs as shown in Table 4-1. Unlike TDM and FDM, GV40 MEAs prepared by ASDM and NDM showed a higher loss in the ohmic region. The loss of performance is observed in the MEAs with poor ionomer dispersion in the catalyst layer with larger clustered catalyst aggregates with inefficient ionic connectivity in the catalyst agglomerates.

The power densities of GV40 TDM and GV40 FDM MEAs were similar from low current densities to high current densities. While there was a similar decrease in the slope of GV40 NDM and GV40 ASDM MEAs power density curves from the ohmic region, indicating internal ohmic resistances dominated by the ionic (proton transfer) resistance and possible membrane dehydration.

4.2.2. V40 MEAs performance

Figure 4.4 shows the polarization and power curves of V40 MEAs prepared by three different catalyst slurry preparation methods.
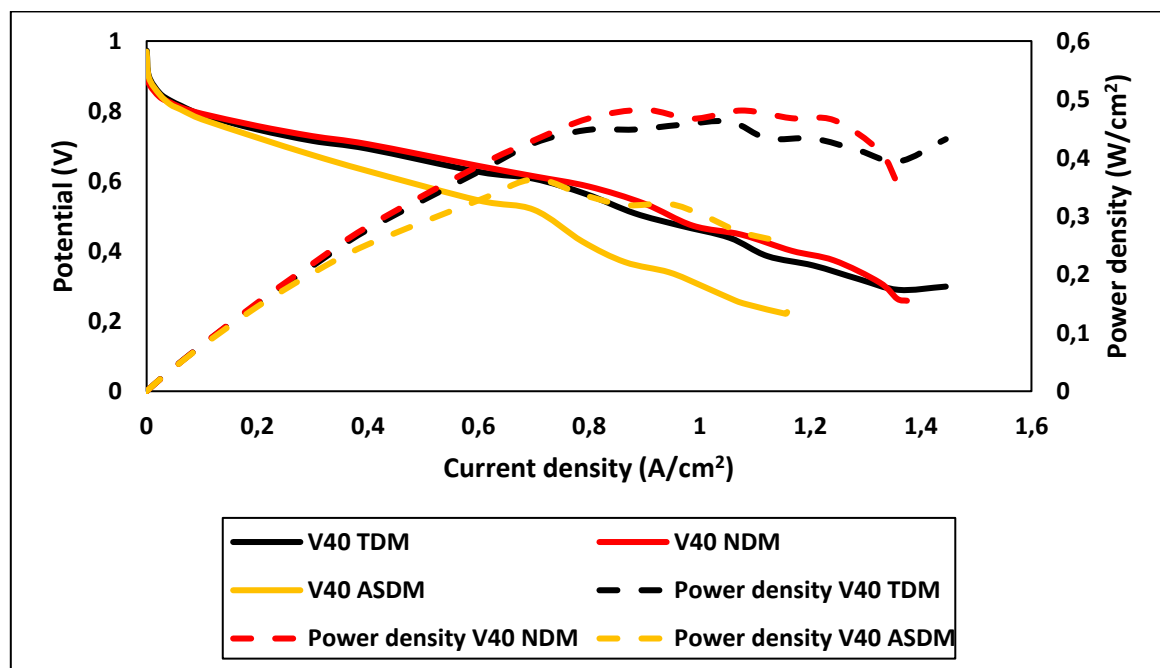

Figure 4.4: Polarization and power curves of V40 MEAs under 74% RH.

For the V40 MEAs, similar potential losses were observed at low current densities (activation losses). V40 ASDM showed major losses in its ohmic region, indicating a weak interaction between the ionomer and V40 which caused a loss in ionomer-V40 interface and protonic connectivity in the catalyst layers. This resulted in decreasing the water uptake in the catalyst layers which also likely led to membrane dehydration. This was confirmed by the increase in performance when the polarization measurement was at 100% RH, the proton conductivity increased with water in the MEA (refer to the appendix A).

TDM and NDM produced similar performance due to the strong ionomer-V40 interaction which resulted in a large interface, increased protonic connectivity and similar BoL ECSA. This confirmed the hypothesis that V40 did not need a drying step to interact with the ionomer, rather its surface properties facilitated its interaction with the ionomer depending on the ionomer-supported catalyst contact time.

4.3.   Electrochemical impedance spectroscopy

MEA resistances were measured with EIS frequency sweep from 20KHz to 0.1Hz at 0.1 A.cm^{-2} to determine the charge transfer resistance.

4.3.1. EIS of GV40 MEAs

Figure 4.5 shows the Nyquist's plots of the GV40 MEAs which consisted of ohmic resistances at high frequency, charge transfer resistance (the diameter of the semi-circle) and the mass transport resistance at low frequency. Although the frequency is not shown in the Nyquist's plot, the frequency increases with the decreasing Zr (Orazem and Tribollet, 2017). The Ohmic resistance (Zr intercept) clearly increased from FDM to NDM, ASDM and TDM. This may be due to the single cells used for testing; Baltic 50 cm^2 cell for GV40 FDM and Pragma 25 cm^2 cell for the rest of GV40 MEAs. However, EIS at a low current density such as 0.1 A.cm^{-2} is predominantly used to probe the charge transfer resistance. The charge transfer resistances (the distance between the initial point and the final point of the semicircle on Zr-axis) increased in the order of FDM < TDM < ASDM < NDM.
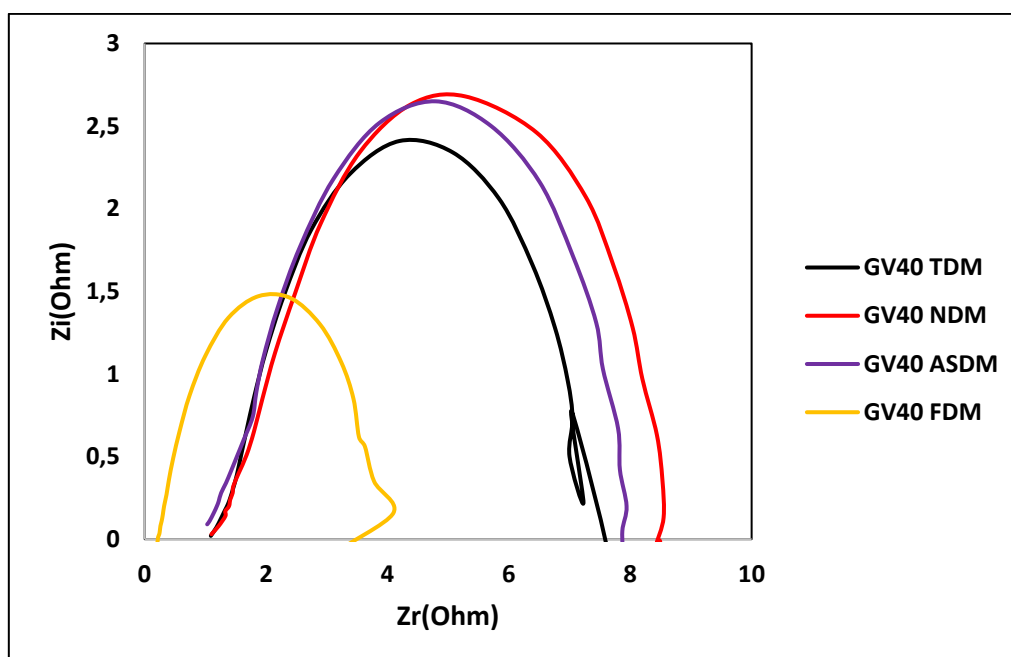

Figure 4.5: Nyquist plots for GV40 MEAs.

ZView was used to fit and simulate the Randle's circuit (Figure 4.6) of these Nyquist plots. The circuit consisted of a resistor (R_S) which was in series with the parallel combination of the constant phase element (CPE) and a charge transfer resistance (R_{CT}) (in series with the Warburg impedance) (Lim *et al.*, 2012) such as:

A. Resistor (R_s): which represented the ohmic resistances due to the cell, the proton exchange membrane, the ionomer layer in the catalyst layer, and contact resistances.
B. Constant phase element (CPE): showing the capacitance of the catalyst layer.
C. Charge transfer resistance (R_{CT}): impedance to HOR and ORR
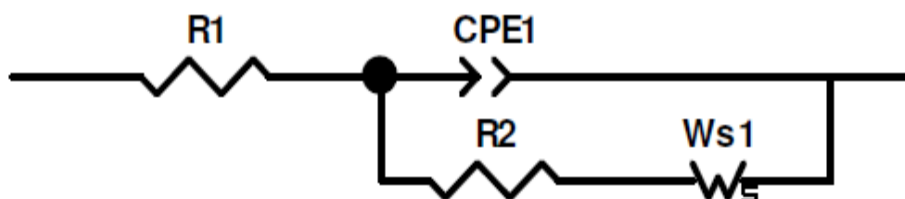D. Warburg impedance (W_s): resistance due to mass transport of reagents and the product.

Figure 4.6: Randle's circuit.

The fitted values of the resistances are shown in Table 4-2:

Table 4-2: EIS results fitted for the GV40 MEAs.

Elements	GV40 TDM	GV40 NDM	GV40 ASDM	GV40 FDM
R_s (Ohm)	1,299	1,538	1,139	1,361
CPE (Farad)	0,810	0,666	0,695	0,645
R_{CT} (Ohm)	**6,117**	**8,400**	**7,670**	**4,595**
W_s (Ohm)	6,052	7,591	6,837	4,596

TDM and FDM produced GV40 MEAs with the lowest charge transfer resistances, suggesting that optimal electron transfer routes were formed with the slow drying rate methods. High charge transfer resistance indicated resistance to the transfer of electrons (via the support) to Pt active sites for oxygen reduction. It is evident that electronic conductivity was limited in GV40 MEAs with poor ionomer distribution. The conductive support in ASDM and NDM GV40 MEAs were likely heavily coated or even completely insulated with ionomer, inhibiting electron transfer. These MEAs presented with clustered of large catalyst aggregates which could possibly have been coated with relatively thick ionomer layers, which severely impacted the electronic connectivity.

4.3.2. EIS of V40 MEAs

The Nyquist plots of the V40 MEAs are shown in Figure 4.7. These plots consisted of semi-circles whose diameters correspond to the charge transfer resistances of the catalyst layers. The semi-circle of V40 ASDM MEA, possessed the largest diameter which indicated that ASDM produced V40 MEAs with the highest resistance to charge transfer.
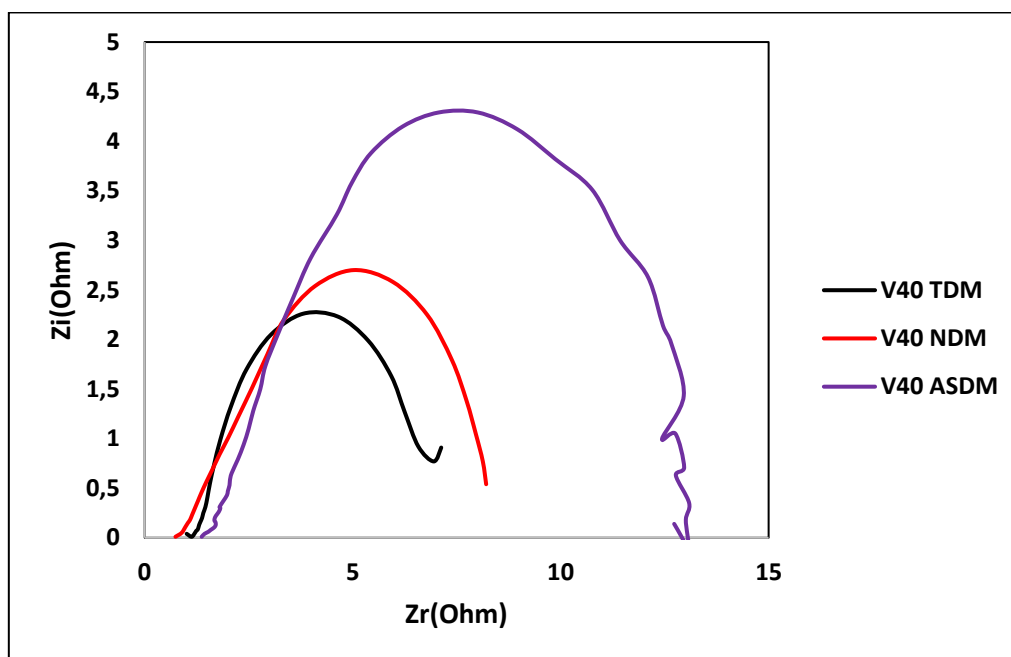

Figure 4.7: Nyquist plots of V40 MEAs.

Table 4-3 summarizes the electrical circuit (Figure 4.6) fitted values determined with ZView. Similar to GV40, only the charge transfer resistances are discussed as the EIS measurement was performed in the activation region of a polarization curve, where ohmic and mass transport resistances were insignificant.

Table 4-3: EIS results fitted for the V40 MEAs.

Elements	V40 TDM	V40 NDM	V40 ASDM
R_s (Ohm)	1,277	0.992	1,668
CPE (Farad)	0,811	0,660	0,728
R_{CT} (Ohm)	**5.920**	**7.851**	**12.530**
W_s (Ohm)	5.274	7,469	11.040

The charge transfer resistance varied with the catalyst slurry preparation method with TDM < NDM < ASDM.

The V40 TDM and NDM MEA electronic structure appear to have similar aggregate structures presented in Figure 3.18, yet V40 TDM presented with a thinner layer as well as a more porous structure, with the highest intrusion pore volume. A thinner layer presents a shorter distance required for electron charge transfer and less resistance. As observed with the lower ECSA, ASDM produced V40 MEA with small ionomer-V40 interfaces and the supported catalyst was clustered in insulated walls of ionomer. The lack of ionomer distribution is highly evident in the large resistance to charge transfer. Clearly, the different preparation methods produced various ionomer-supported catalyst interfaces which increased or reduced the resistance to charge transfer for the required electrochemical reactions.

The different catalyst slurry preparation methods produced different structures of the ionomer-supported catalyst agglomerates and aggregates in the catalyst layers which affected the MEA performance.

Catalyst slurry preparation methods with slow drying rates (TDM and FDM) produced GV40 MEAs with the lowest charge transfer resistance, the highest BoL ECSA and best performance (0.614 A.cm^{-2} and 0.686 A.cm^{-2} for FDM and TDM, respectively at 0.65V). This is likely due to the optimal porous structure achieved during the drying step of the catalyst slurry preparation, allowing an optimal contact between the ionomer and the supported catalyst. Therefore, more three-phase boundary (TPB) sites were formed when the slow drying methods (FDM and TDM) were used.

Due to the stronger interaction between the ionomer and V40 (compared to GV40), no significant difference was observed between V40 TDM and V40 NDM MEAs. Similar performance and BoL ECSA were achieved. The surface properties of V40 (lower hydrophobicity) facilitated its interactions with the ionomer which ensured protonic connectivity in the catalyst layer.

The fast-drying catalyst slurry preparation method (ASDM) produced GV40 MEAs and V40 MEAs with poor performances, low BoL ECSAs and relatively high charge transfer resistances. This was due to the poor ionomer-supported catalyst interface, decreasing the protonic connectivity, and isolation of Pt sites caused by either ionomer agglomeration or thick film aggregate coatings.

# Chapter 5 Ex-situ electrochemical evaluation

with the half-MEA

A half-MEA test cell was used to perform accelerated stress tests (ASTs) on the cathode prepared by different catalyst slurry preparation methods. Two protocols were followed:

1. AST as suggested by the US DoE in nitrogen.
2. AST as suggested by the US DoE with cycling in oxygen.

5.1.   Accelerated stress test in nitrogen

ASTs were carried out in nitrogen atmosphere. The ECSA was determined at the beginning of life (BoL) as well as between AST cycles. Equation 1.7 was used to estimate the ECSA. The two following electrochemical reactions were considered to cause the variations in the ECSA and hydroquinone-quinone capacitance:

$$C + 2H_2O \rightarrow CO_2 + 4H^+ + 4e^- \qquad (1)$$

$$Pt + xH_2O \leftrightarrow PtO_x + 2xH^+ + 2xe^- \qquad (2)$$
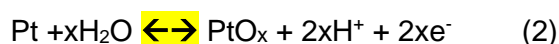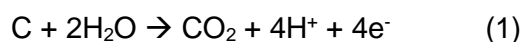
The oxidation of Pt (the catalyst) in the presence of water, resulted in the formation of PtO_x which was not active and reduced the number of active sites in the catalyst layer (loss in ECSA). Similarly, the support (carbon) oxidised in the presence of water to form CO_2. The support loss resulted in a loss of electronic connectivity (decrease in double layer capacitance (DLC) and hydroquinone-quinone capacitance) and in the agglomeration of Pt particles (loss in ECSA). The hydroquinone-quinone (from the carbon support) charge is generated from the two-electron and two-proton redox reaction of benzoquinone and hydroquinone on the carbon support in the presence of water (Valent, Koryta and Panoch, 1987). The change in hydroquinone-quinone charge (or capacitance) can be indicative of carbon corrosion as it strongly depends on the specific surface area and surface chemistry of the carbon support (Castanheira *et al.*, 2015).

The presence of water is indispensable as it is required for the proton conductivity in the catalyst layer and keeps the membrane hydrated. In the half-MEA, two sources of water were considered: from the pool of liquid electrolyte and from the humidified reagent (nitrogen gas).

Figure 5.1 shows the cyclic voltammograms of a GV40 ASDM half-MEA (other CVs in appendix B) with the characteristic peaks of Pt/C, during cycling between 1-1.5V vs SHE in nitrogen.
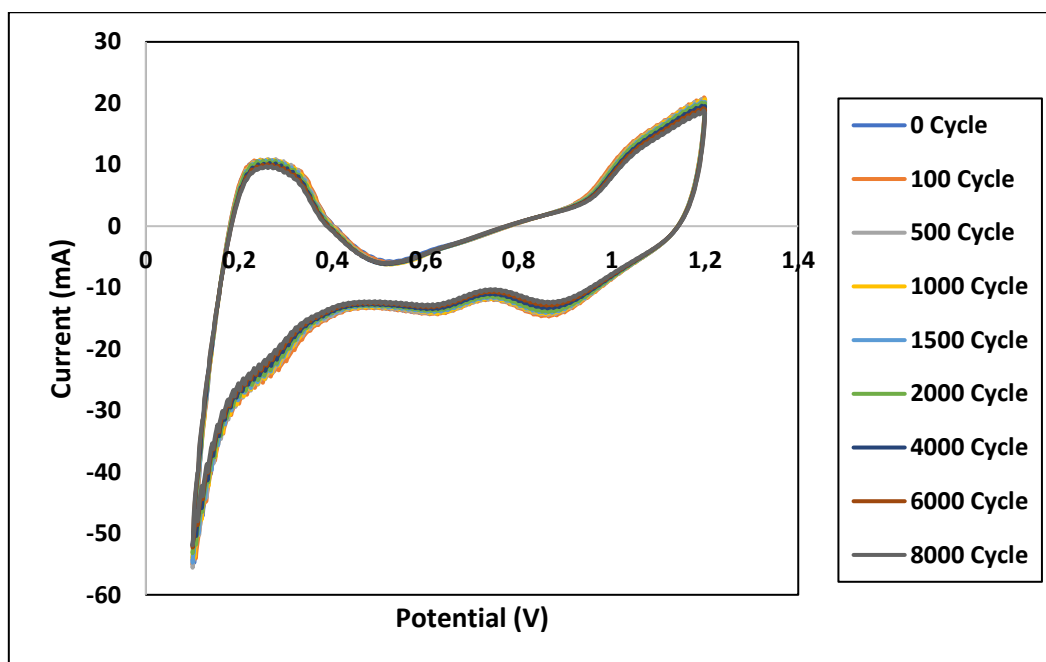

Figure 5.1: Cyclic voltammograms of GV40 ASDM MEA recorded after stress cycles in N_2.

Figures 5.2 and 5.3 show ECSA as a function of stress cycle for GV40 and V40 half-MEAs, respectively.
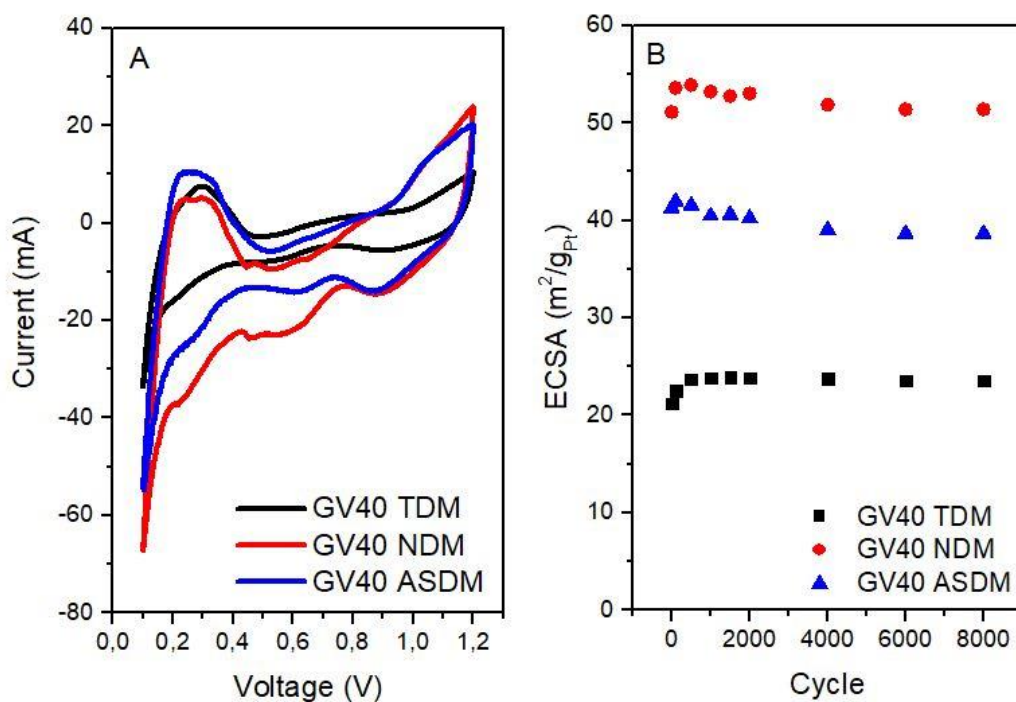

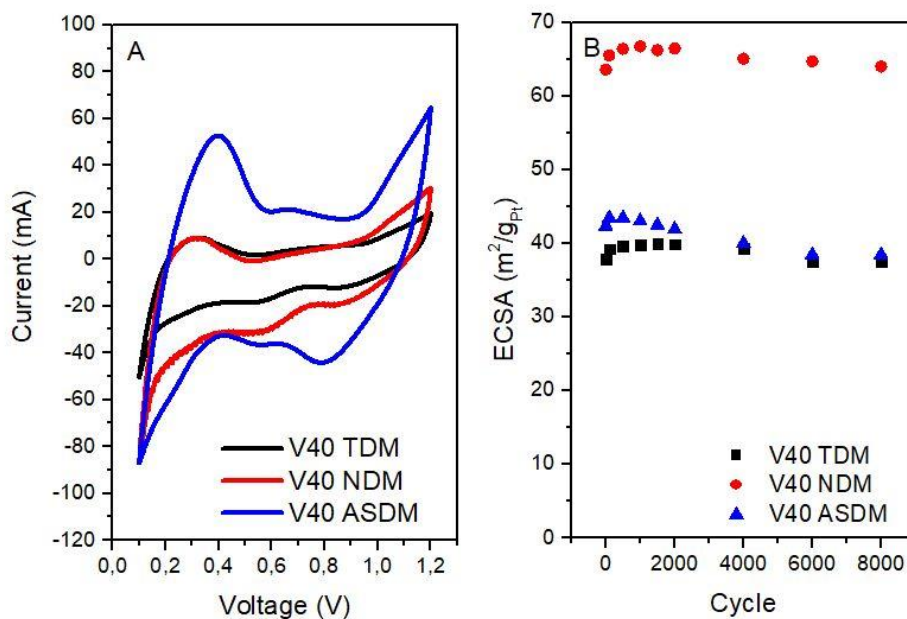*Figure 5.2: A) BoL Cyclic voltammograms of GV40 MEAs; B) Variation of GV40 half-MEAs ECSA during AST in N_2.*

Figure 5.3: A) BoL Cyclic voltammograms of V40 MEAs; B) Variation of V40 half-MEAs ECSA during AST in N_2.

The ECSA varied significantly from the ECSAs obtained from in-situ measurements (full MEA testing). With the half-cell, the GV40 NDM BoL ECSA was 2.4 times higher than GV40 TDM half-MEA. While with the in-situ measurements, GV40 TDM BoL ECSA was 1.30 times higher than GV40 NDM. These variations in the half-cell measurements were likely due to the uncontrolled N_2 flowrate (affects the shape of the CV) and poor N_2 pathway through the catalyst layer. N_2 flow rate and pathway during CV, play a key role in ECSA measurement (Carter *et al.*, 2007). The parallel flow field plate with inlet and outlet openings on the same side, as shown in Figure 5.4A, restricted the N_2 flow pathway. The humidified N_2 gas likely exited the cell as it entered and did not circulate through the entire catalyst layer. Optimizing the flow field plate would consist of channelling the N_2 gas through a serpentine pathway as shown in Figure 5.4 B, which would force the N_2 gas to circulate the entire catalyst layer.
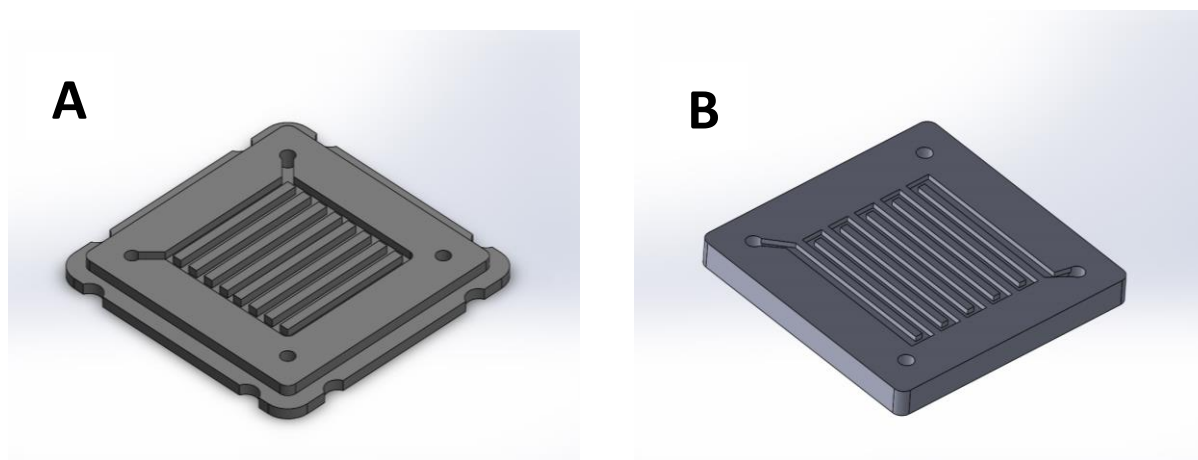
Figure 5.4: A) Parallel flow field plate; B) Serpentine flow field plate

It was evident that the high-pressure gas flow with controlled back pressures at which in-situ analysis was performed had an influenced on the ECSA. <mark>Therefore, N_2 flowrate in the half-MEA cell constituted a major artifact during ECSA measurement (Carter *et al.*, 2007).</mark>

Therefore, values measured with the half-cell could not quantitatively reflect the ECSA and could only be used as a qualitative measure. The ASDM half-MEAs (GV40 and V40) reached a maximum ECSA after 100 stress cycles and showed clear ECSA losses. The initial increase in ECSA to a maximum value was likely due to the increased protonic connectivity with the absorption of water by the poorly distributed ionomer during initial cycling. The ECSAs of ASDM half-MEAs only started to decrease after 100 stress cycles which could indicate that the retained water started to react with the carbon support to form CO_2 and resulted in ECSA losses (7.85% and 11.5% of GV40 ASDM and V40 ASDM respectively after 8000 stress cycles). The ECSA of GV40 NDM peaked after 100 stress cycles, likely due to the enhanced wettability of the catalyst layer which improved its protonic connectivity. GV40 NDM experienced a slow decrease in ECSA after 100 cycles (4.68% loss after 8000 stress cycles).

In the cases of GV40 TDM, V40 NDM and V40 TDM, the maximum ECSA was reached after 1500, 1000 and 1500 stress cycles, respectively. This could be due to the longer period required to maximise the water retention by the well distributed ionomer with cycling, increasing the protonic connectivity in the catalyst layers. The ECSA values slowly dropped 1.57%, 4.09% and 6.18% less than their maximum values for GV40 TDM, V40 NDM and V40 TDM, respectively.

The capacitance of the catalyst layers in the non-faradaic region of the cyclic voltammogram (0.5 – 0.8V; hydroquinone-quinone capacitance, including the DLC) is highly dependent on the carbon support (Castanheira *et al.*, 2015). Castanheira *et al.*, (2015) observed a gradual increase of the hydroquinone-quinone charge to a maximum before it decreased. Less durable supports reached their maximum hydroquinone-quinone charge in the earlier stress cycles and then decreased. The charge of the less organised carbon support was higher than the more structured carbon (Castanheira *et al.*, 2015).

Figures 5.5 and 5.6 present the hydroquinone-quinone capacitance (determined by integrating the capacitance between 0.5V and 0.8V) of GV40 and V40 half-MEAs, respectively, as functions of stress cycles. V40 half-MEAs showed higher hydroquinone-quinone capacitances than their GV40 counterparts. This was likely due to the large specific surface area and surface chemistry of Vulcan. Vulcan is a Sp^3-hybridized carbon with a high order of defect and results in higher hydroquinone-quinone capacitance and therefore more prone to oxidize compared

to a more graphitised Sp^2-hybridized carbon with a lower order of defect (Stevenson and Pattrick, 2017).
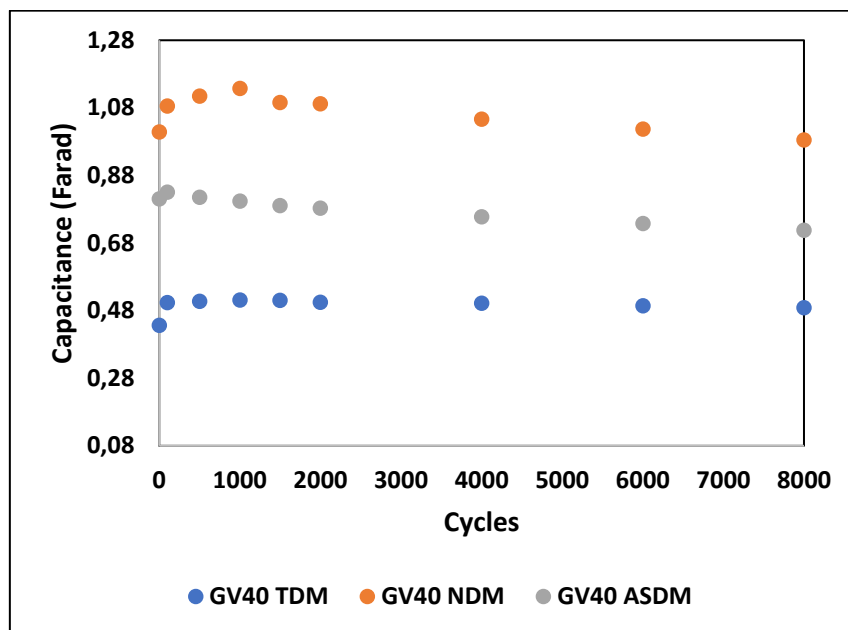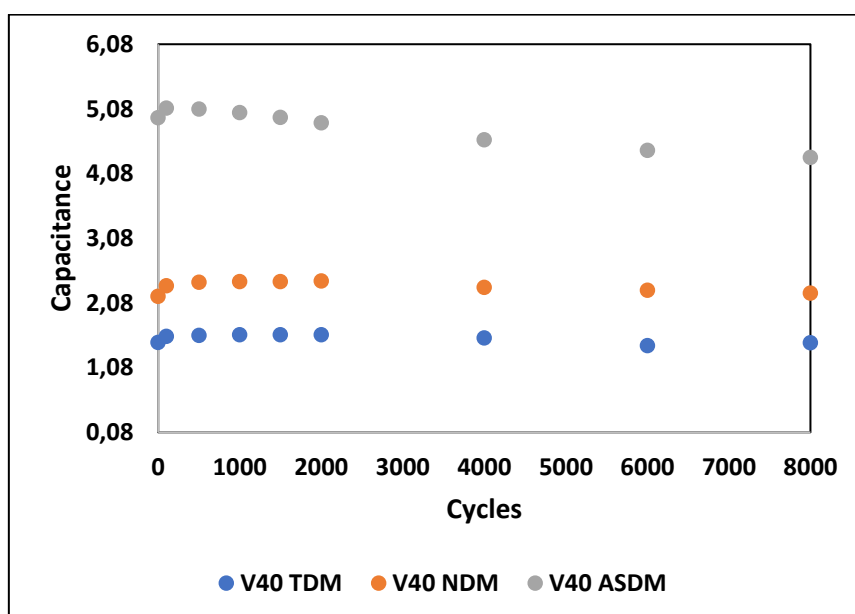

Figure 5.5: hydroquinone-quinone capacitance of GV40 half-MEAs as a function of stress cycles done N₂.

GV40 TDM half-MEA showed the lowest absolute hydroquinone-quinone capacitance, this was likely due to the good ionomer distribution and coverage around the supported catalyst since the hydroquinone-quinone capacitance strongly depends on the support surface area. The orientation of the ionomer played a key role in the water-carbon interactions (or contact), the hydrophilic side-chain of the ionomer pointed outwardly and interacted with water while its hydrophobic backbone interacted with GV and formed a hydrophobic boundary which protected the support from a rapid corrosion. Therefore, a slow decrease in the hydroquinone-quinone capacitance was observed with GV40 TDM. Unlike NDM and ASDM which formed smaller ionomer-GV40 interfaces and low ionomer coverage which resulted in higher hydroquinone-quinone capacitances.

The hydroquinone-quinone capacitance of GV40 TDM half-MEA reached its maximum value after 1500 stress cycles and remained relatively steady through to 8000 stress cycles. While GV40 NDM hydroquinone-quinone capacitance peaked after 1000 stress cycles and decreased. GV40 ASDM reached its maximum hydroquinone-quinone capacitance after only 100 stress cycles and then decreased. It could be concluded that TDM produced a GV40 catalyst layer with the hydroquinone-quinone capacitance which remained relatively steady, even after 8000 stress cycles. This was due to the good ionomer dispersion, coverage and orientation which formed more hydrophobic boundaries (which insulated the support) and resulted in high resistance to carbon corrosion. In contrast ASDM, produced a GV40 catalyst

layer with the lowest resistance to carbon corrosion, showing a relatively rapid drop in the hydroquinone-quinone capacitance after only 100 stress cycles. This could likely be due to the poor ionomer-GV40 interfaces formed during ASDM, which exposed the GV support to water induced carbon corrosion.

In Figure 5.6, V40 ASDM showed the highest absolute hydroquinone-quinone capacitance, likely due to the poor distribution and low coverage of the ionomer onto the support. The lowest absolute hydroquinone-quinone capacitance of V40 TDM indicated a good ionomer distribution and coverage onto the support. The hydroquinone-quinone capacitance for both V40 TDM and V40 NDM peaked after 1500 stress cycles and slowly decreased as shown in Figure 5.6. The V40 ASDM hydroquinone-quinone capacitance reached a maximum value after only 100 stress cycles and rapidly decreased thereafter. This indicated that NDM and TDM produced V40 catalyst layers with higher resistance to carbon corrosion while ASDM resulted in a V40 catalyst layer with low resistance to carbon corrosion (Castanheira *et al.*, 2015). NDM and TDM showed higher resistance to corrosion likely due to the good ionomer distribution and large ionomer-V40 interfaces which insulated Vulcan from water induced carbon corrosion.

Figure 5.6: hydroquinone-quinone capacitance of V40 half-MEAs as a function of stress cycles done in N_2.

Two sources of water were identified with the half-MEA setup: the humidified nitrogen inlet gas and water molecules from the electrolyte (1M H_2SO_4) pool. The nitrogen was bubbled through water at ambient temperature (approximately 25°C), resulting in relatively low humidity conditions, approximately 39% RH (assuming a dew point of 10°C). And water diffusion from the pool to the catalyst layer caused a water gradient along the thickness of the catalyst layer while the restricted N_2 flow pathway through the parallel flow field plate caused

a water gradient along the surface of the catalyst layer. The water concentration decreased along the thickness of the catalyst layer, from the pool side through to the GDL and flow-field plate, resulting in a limiting amount of water which decreased the oxidation rates of Pt and carbon support. Therefore, as a follow up evaluation, oxygen was bubbled and flowed through the working electrode (catalyst layer; cathode) during stress cycles to enhance carbon corrosion.

5.2.   Accelerated stress test in oxygen

In the presence of humidified oxygen, four electrochemical reactions were expected to occur during a potential cycling AST:

$$C + 2H_2O \rightarrow CO_2 + 4H^+ + 4e^- \qquad (3)$$

$$Pt + xH_2O \longleftrightarrow PtO_x + 2xH^+ + 2xe^- \qquad (4)$$

$$C + O_2 \rightarrow CO_2 \qquad (5)$$

$$Pt + xO_2 \longleftrightarrow PtO_{2x} \qquad (6)$$
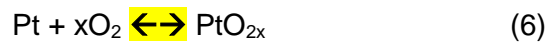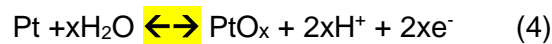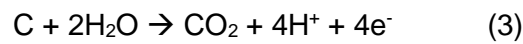
Where reactions (5) and (6) were mostly favoured due to the predominant presence of oxygen. Pt reacting separately with both water and oxygen, would result in the formation of PtO_x which is not active. Carbon support would oxidize in the presence of water and oxygen, causing a loss in the electronic connectivity of the catalyst layer and the agglomeration of Pt particles.

Figure 5.7 shows the cyclic voltammograms of GV40 ASDM half-MEA (other CVs in Appendix B), after cycling between 1-1.5V vs SHE in oxygen. Prior to CV measurements, the cell was purged by N_2 for 15 minutes to remove traces of oxygen.
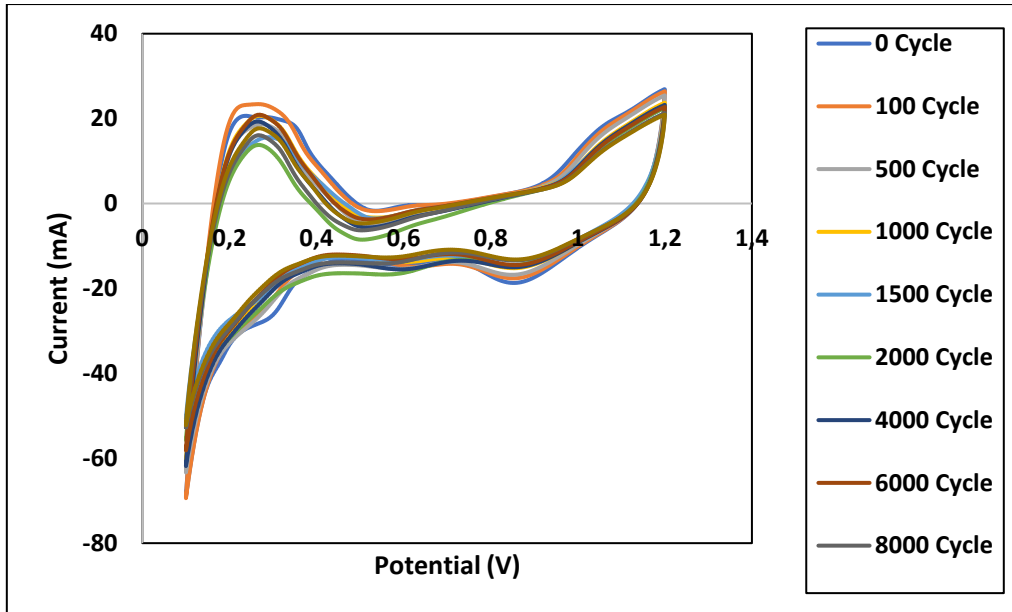
Figure 5.7: Cyclic voltammograms of GV40 ASDM MEA recorded after stress cycles in O₂.

Figures 5.8 and 5.9 show ECSAs as functions of stress cycle. The BoL ECSAs of the half-MEAs in Figures 5.8 and 5.9 varied from the ECSAs measured in Figure 5.2 and 5.3. These inconsistencies in ECSA measurements were likely caused by the ineffective and inconsistent transport of the humidified nitrogen gas through the catalyst layer. The gas flow was neither controlled nor channelled consistently, which resulted in different ECSA values of catalyst layers consisting of the same catalyst slurry (and similar loadings).
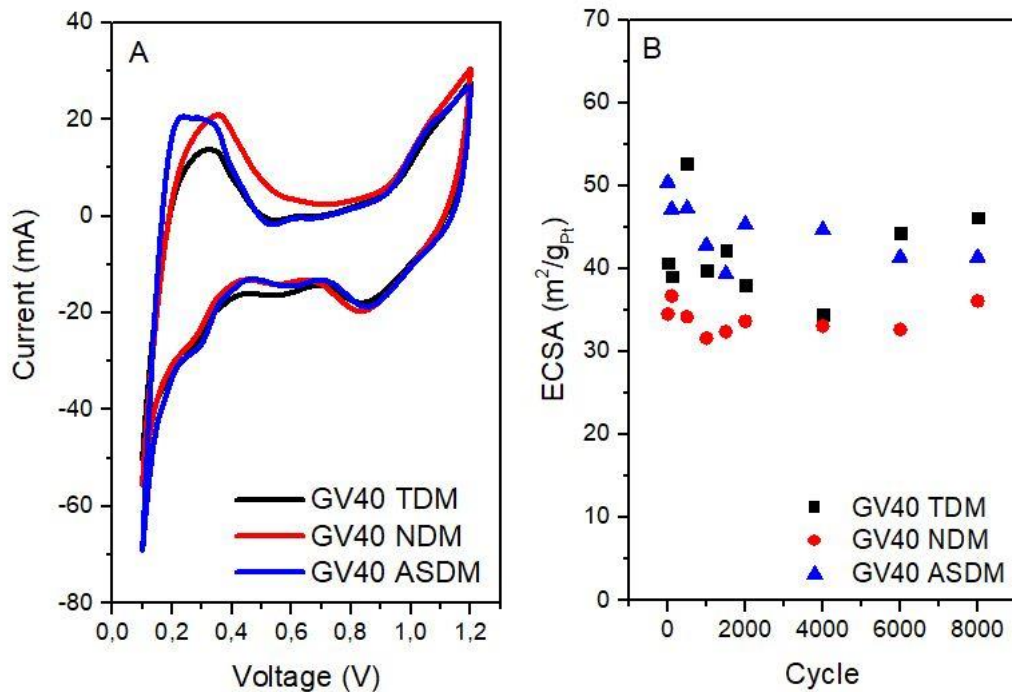
Figure 5.8: A) BoL cyclic voltammograms of GV40 MEAs; B) Variation of GV40 half-MEAs ECSA during AST in O₂

81
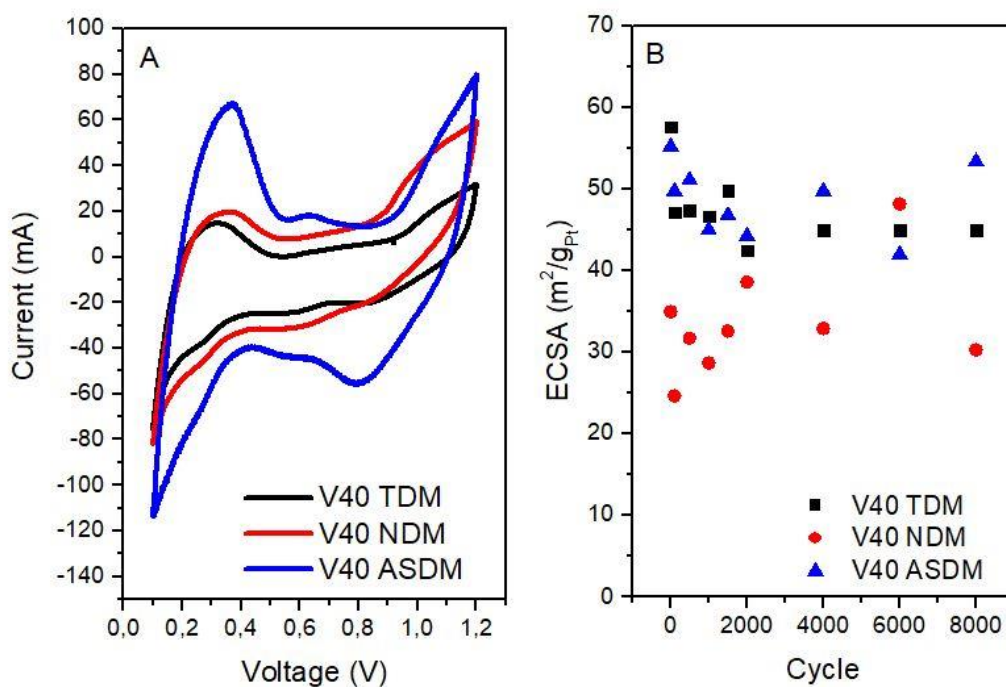
Figure 5.9: A) BoL of cyclic voltammograms of V40 MEAs; B) Variation of V40 half-MEAs ECSA during AST in O_2

The erratic changes of the ECSAs may be due to the oxidation and reduction of Pt which was exasperated due to a stagnant state. The nitrogen gas did not effectively purge the catalyst layers due to the ineffective transport pathway of the parallel flow field plate.

Further investigations consisted of determining the hydroquinone-quinone capacitance as a function of stress cycle. Unlike the capacitance-cycle plots in Figures 5.5 and 5.6, the hydroquinone-quinone capacitances decreased during the initial stress cycles, increased to a second maximum capacitance (while the first maximum capacitance was the initial capacitance) and linearly decreased with increasing stress cycles. The decrease of the hydroquinone-quinone capacitance in the early stress cycles could be due to the bare support oxidation as in the electrochemical reaction (5). While the small increase of the hydroquinone-quinone capacitance and linear decrease indicated the interaction and further oxidation by water, respectively.

Figure 5.10 shows the hydroquinone-quinone capacitances of GV40 half-MEAs as functions of stress cycles.
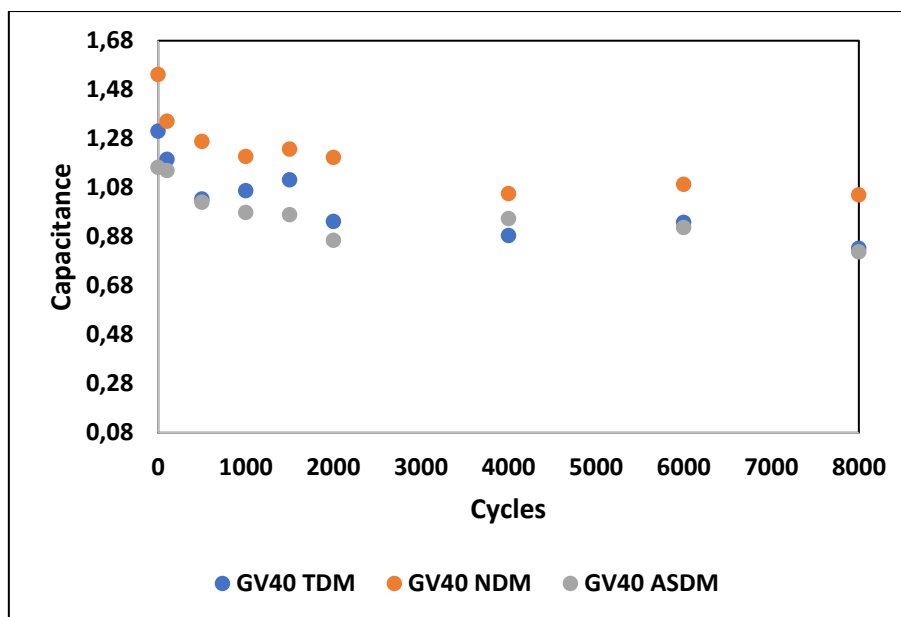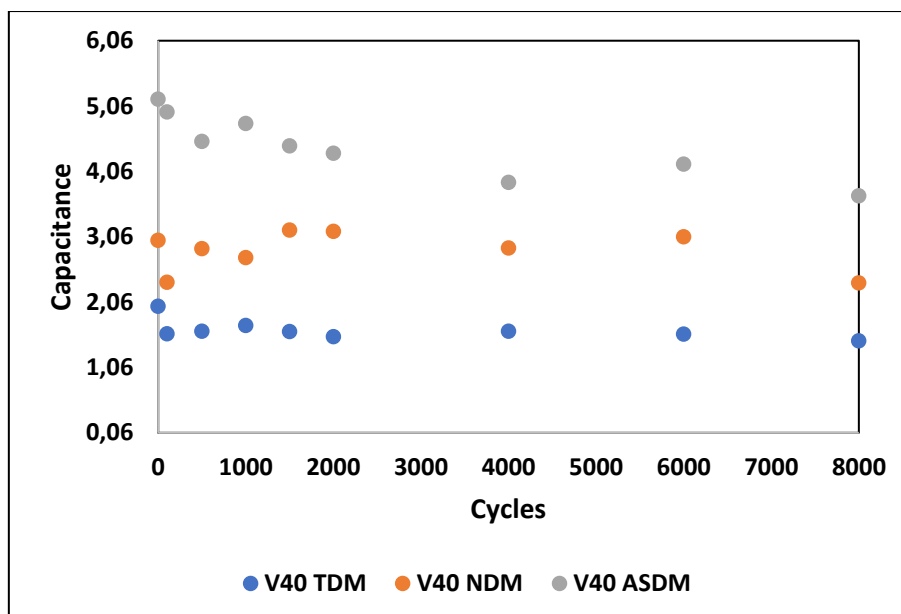
Figure 5.10: Hydroquinone-quinone capacitance of GV40 half-MEAs as a function of stress cycles done in O_2

The hydroquinone-quinone capacitance of GV40 half-MEAs rapidly decreased in the early stress cycles, likely due to the loss of electron connectivity caused by the bare support oxidation with oxygen. The initial loss of GV40 NDM and GV40 ASDM hydroquinone-quinone capacitance extended to 1000 stress cycles, unlike GV40 TDM with the rapid loss only within the 500 initial stress cycles. Assuming the losses observed in the early stress cycles were due to the bare support oxidation, it was concluded that the initial loss in GV40 TDM hydroquinone-quinone capacitance stopped after 500 stress cycles because of its good ionomer dispersion and coverage which insulated the support from oxygen. While the initial drop of GV40 NDM and GV40 ASDM hydroquinone-quinone capacitance continued until 1000 stress cycles because of the smaller ionomer-supported catalyst interfaces which exposed the support to oxygen and corrosion. Their second maximum hydroquinone-quinone capacitances indicated the changes in the ionomer-supported catalyst interfaces due to the increase of the catalyst layer wettability. And the slow decrease observed between 2000-8000 stress cycles likely signified the further oxidation of the support with water.

Similarly, the hydroquinone-quinone capacitance of V40 half-MEAs decreased during the early stress cycles, increased to a second maximum value before it decreased linearly as shown in Figure 5.11.

83

Figure 5.11: Hydroquinone-quinone capacitance of V40 half-MEAs as a function of stress cycles done in O$_2$

The hydroquinone-quinone capacitances of V40 NDM and TDM initial decreased after 100 stress cycles, indicating a similar ionomer coverage which insulated Vulcan from oxygen and corrosion unlike V40 ASDM with a continual decrease in hydroquinone-quinone capacitance until 500 stress cycles.

EIS was included during AST to investigate the impact of carbon corrosion on the ionomer in the catalyst layer. The findings are discussed in the next section.

5.3. Electrochemical impedance spectroscopy during AST in nitrogen.

The AST was further probed with EIS. EIS frequency sweeps were taken after each set cycle in `the range of 20 KHz to 100 mHz at the potential of 0.5V vs SHE, in the ohmic region to study the effect of AST cycles on the ionomer (Saleh and Easton, 2012). Figure 5.12 shows Nyquist plots as a function of cycle number for GV40 TDM half-MEA (Nyquist plots for other MEA slurries in Appendix).
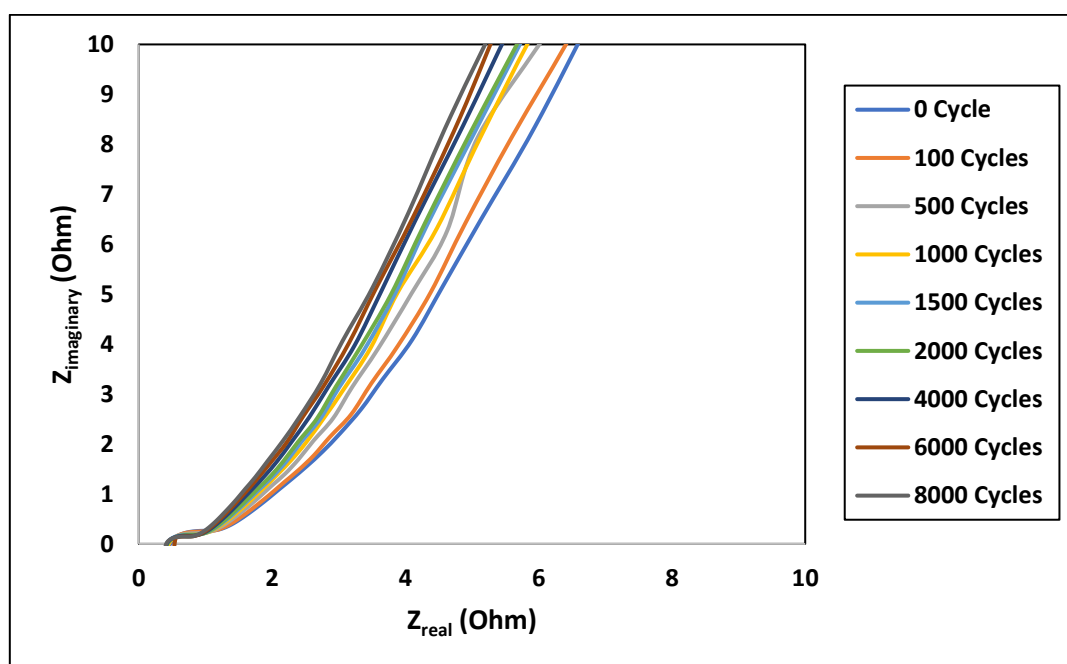
Figure 5.12: Nyquist plots during AST of GV40 TDM half-MEA.

In the ohmic region (0.5V), the charge transfer resistance may be assumed negligible in the presence of nitrogen gas since no ORR occurs. The predominant resistance observed was ionic due to the ionomer (proton conductor in the catalyst layer) and the membrane at high frequency (at low Z_{real}). The Warburg-like component at low frequency (at high Z_{real}) was attributed to the resistance due to mass transport, and its angle slowly increased with increasing stress cycle.

The ohmic resistances were estimated by ZView and their variations were compared as a function of cycles. The ohmic resistance losses after stress cycles for the GV40 half-MEAs (cathodes) are shown in Figure 5.13. The percentage losses were calculated based on the ohmic resistance before AST cycles (0 cycle).
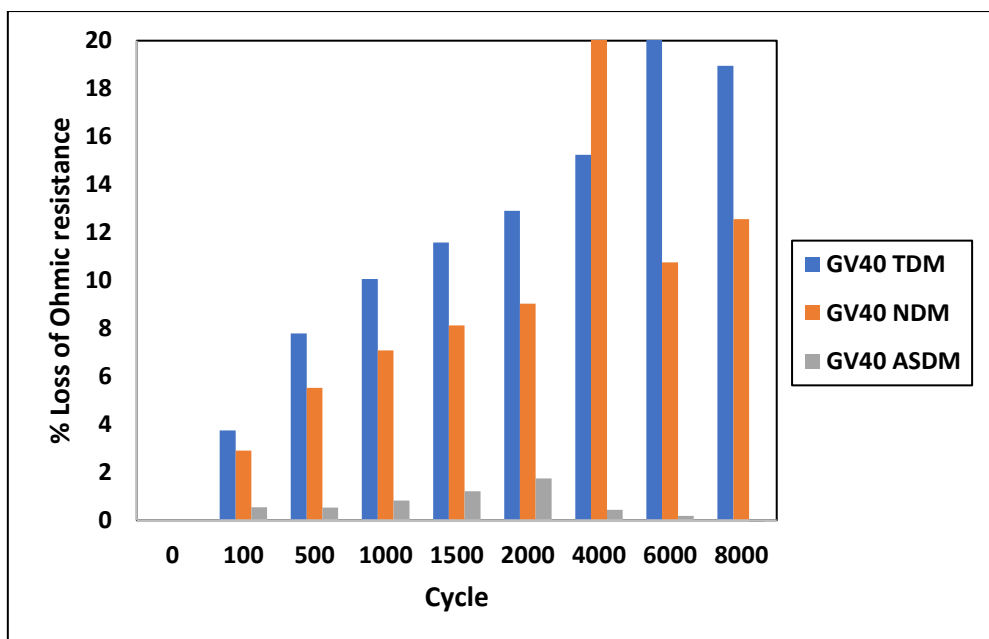
Figure 5.13: The ohmic resistances % loss of the GV40 half-MEAs as a function of stress cycles.

The highest loss in ohmic resistance (19%) was observed with the GV40 TDM half-MEA. Results in previous chapters have shown that GV40 TDM presented with optimal ionomer dispersion and orientation around the GV40 catalyst (hydrophobic compacts with the side chain pointed outwardly). The decrease in the ohmic resistance was likely due to the retaining of water molecules by the hydrophilic sidechain. It is suggested that the retained water molecules improved the proton conductivity of the ionomer (by swelling the ionomer) in the catalyst layer and resulted in a decrease in the ohmic resistance. The lowest loss in the ohmic resistance was observed with GV40 ASDM, which increased to a maximum percentage loss (only 1.75%) after 2000 stress cycles and slowly decreased. The small ionomer-GV40 interfaces formed during ASDM indicated the presence of unattached large ionomer clusters which could retain water. However, no significant increase in the protonic connectivity of GV40 ASDM catalyst layer due to the isolation of these large ionomer clusters.

In the case of V40 half-MEAs, the ohmic resistance losses were also estimated by ZView and compared as a function stress cycles, as shown in Figure 5.14.
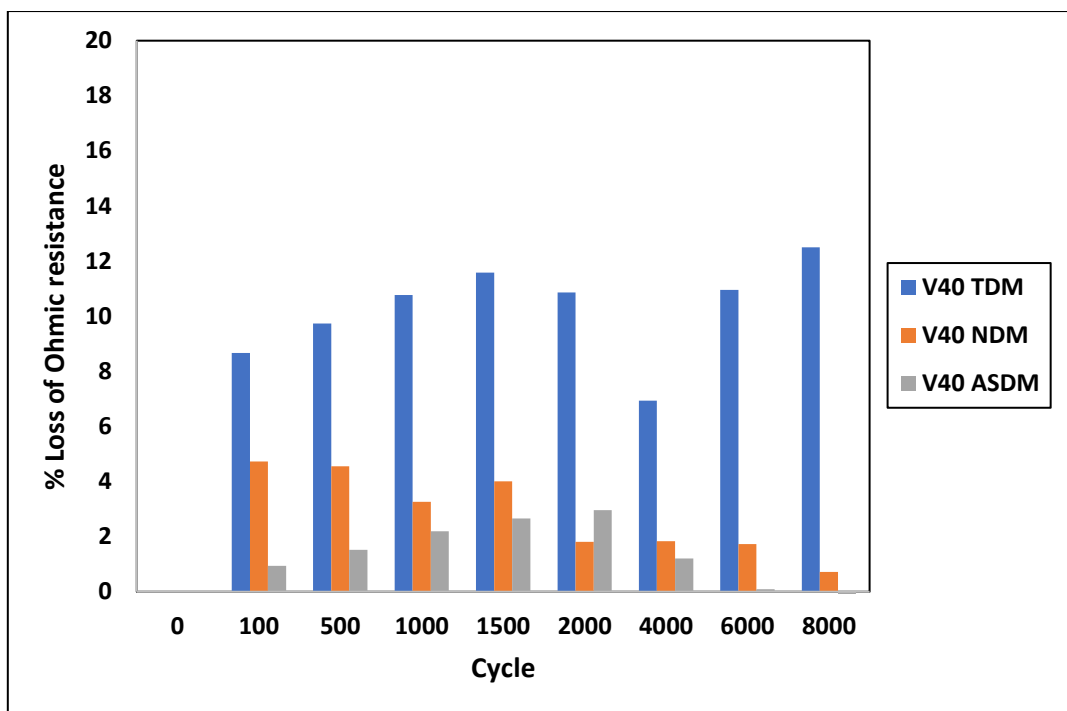
Figure 5.14: The ohmic resistances % loss of the V40 half-MEAs as a function of stress cycles.

The ohmic resistance of V40 TDM and V40 NDM half-MEAs decreased 12.5% and 1.00 %, respectively, of their initial values after 8000 stress cycles, suggesting an improvement in the ionic conductivity in the catalyst layer. This was likely due to the absorption of water molecules (provided by the electrolyte in the pool and the moisture in the N_2 feed) into the ionomer which was well dispersed and attached onto V40. While the ohmic resistance of V40 ASDM increased to a maximum value (after 2000 stress cycles) and decreased to its initial value after 8000 cycles. This was due to the poor distribution of the ionomer which resulted in large clusters of ionomer that could retain water but could not significantly improve the protonic connectivity. It could be concluded that the AST in nitrogen improved the wettability of the catalyst layers with the retaining of water molecules by the ionomer which increased their protonic connectivity.

Irrespective of its orientation or dispersion, the ionomer in the catalyst layers did not degrade during AST cycles in N_2. This was determined by studying the capacitance as a function of the catalyst layer resistance. The capacitance was indirectly proportional to the product of the phase angle and imaginary resistance (Saleh and Easton, 2012). The capacitance plots shown in Figure 5.15 were used to investigate the impact of AST on the ionomer in GV40 TDM (other capacitance plots in the Appendix B). Herein the capacitance plotted as the y-axis and resistance in x-axis.
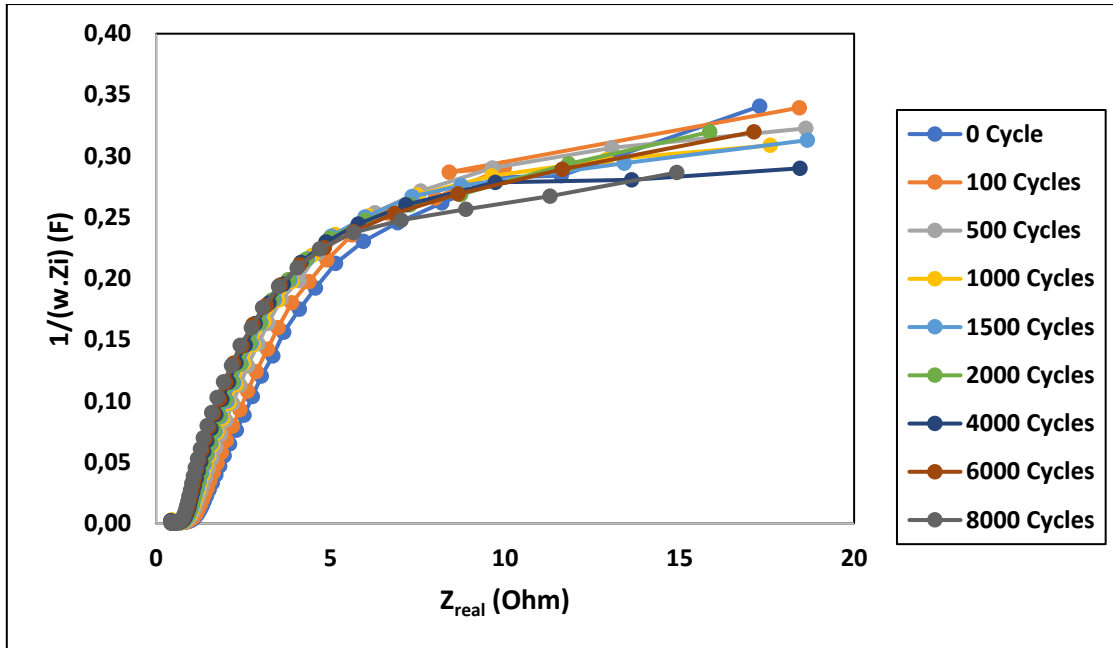
Figure 5.15: Capacitance plots during AST in N_2 of GV40 TDM half-MEA.

The change in the initial slope of the GV40 TDM half-MEA capacitance plots at high frequency (low Z_{real}) was very small (Figure 5.15 and Table 5-1) with slopes approaching zero. These results, like the results presented by Saleh and Easton, 2012, demonstrated that the ionomer was stable with no degradation during the AST cycles. The slope for each GV40 half-MEA and V40 half-MEAs plot as functions of stress cycles are summarized in Table 5-1.

Table 5-1: Estimated initial slopes of the capacitance plots.

Constant intercept	
Half-MEA	Slope
GV40 TDM	-1×10^{-4}
GV40 NDM	-2×10^{-5}
GV40 ASDM	-9×10^{-5}
V40 TDM	-9×10^{-4}
V40 NDM	-8×10^{-4}
V40 ASDM	-7×10^{-5}

The estimated slopes approached zero strongly suggesting no significant changes were observed in the initial slopes of GV40 and V40 capacitance plots, as functions of AST cycles. The ionomer was therefore, not impacted by the AST in any of the MEAs studied.

In this chapter the support corrosion was investigated by the AST and the impact of stress cycles on the ionomer was analysed by EIS. The key results are summarized as follows:

1. During stress cycles, only the carbon support degraded during the DoE AST in N_2. The ionomer did not oxidise nor degrade.

2. Support corrosion depended on the humidity in the half-MEA cell provided by the electrolyte in the pool and from the humidified N_2. The latter was ineffective due to the ineffective parallel flow field plate used. It is likely that only a single channel was used between inlet and exhaust and the humidified N_2 gas did not optimally circulate through the catalyst layer.

3. TDM and NDM produced GV40 and V40 half-MEAs with the highest resistance to corrosion, respectively. This was shown with their smallest losses in the hydroquinone-quinone capacitance during AST in N_2. The variations in the ECSA during AST in O_2 were likely caused by the oxidation and reduction of Pt.

4. The ionomer distribution and orientation in the catalyst layer affected the rate of carbon corrosion. Good ionomer distribution retarded carbon corrosion by absorbing incoming water with its hydrophilic side-chains (as seen with GV40 TDM, V40 TDM and V40 NDM). While poor ionomer distribution formed small ionomer-supported catalyst interfaces which exposed the carbon support to incoming water and corrosion (as seen with ASDM half-MEAs and GV40 NDM).

Chapter 6 Conclusions and recommendations

1.1.   Conclusions

The preparation of the catalyst slurry inks affects the performance of membrane electrode assembly (MEAs) used in hydrogen fuel cell applications. The objective of this study was to determine the impact of the thermal drying during catalyst slurry preparation on the MEA performance and to optimize the preparation method to be time and energy efficient.

Various catalyst slurry preparation methods were used to study the ionomer-supported catalyst interactions: TDM, ASDM, FDM and NDM. The FDM and ASDM were incorporated to isolate the impact of thermal drying (high temperature) and to decrease the drying period, respectively. The impact of the support surface properties on the ionomer attachment onto the supported catalyst was investigated by using two supported catalysts GV40 and V40. GV40 has a graphitised Vulcan support with higher electron conductivity and higher hydrophobicity compared to V40.

The study showed that the way the ionomer interacted and shaped around the carbon support, depended on the nature of the support as well as the presence of the Pt catalyst. The hydrophobic backbone of the ionomer faced the GV support and its side chain interacted with the platinum, resulting in the formation of hydrophobic compacts with the side-chain pointing outwardly. The hydrophilic side-chain was drawn to the platinum and less hydrophobic Vulcan, which resulted in the formation of hydrophilic compacts with the hydrophobic backbone pointing outwardly. The mechanism of the ionomer attachment only depended on the surface properties of the supported catalyst, irrespective of the catalyst slurry preparation method.

The density of the supported catalyst layer and the catalyst slurry preparation method determined the catalyst layer thicknesses. V40 catalyst layers were thicker than GV40 catalyst layers due to the lower density of the V40 catalyst slurry. The slow drying rate methods (TDM and FDM) resulted in the thinner, denser GV40 and V40 cathodes layered structures compared to fast drying methods.

Good protonic connectivity and mass transport properties of the catalyst layer depended on the ionomer-supported catalyst interfaces and the size of aggregates formed, respectively. The fast-drying rate method (ASDM) resulted in the formation of large ionomer-supported catalyst aggregates and small ionomer-supported catalyst interfaces in both GV40 and V40 catalyst layers, which inhibited their mass transport properties and decreased the protonic connectivity, respectively. The NDM resulted in large ionomer-GV40 aggregates with small

interfaces between the ionomer and GV40 due to the hydrophobic surface of GV. In contrast, the hydrophilic surface of Vulcan facilitated its interactions with the ionomer and resulted in the formation of large ionomer-V40 interfaces and relatively smaller ionomer-V40 aggregates. Which increased the protonic connectivity and improved the mass transport properties of the catalyst layers, respectively. The slow-drying methods (TDM and FDM) produced large ionomer-supported catalyst interfaces and aggregates indicating optimal protonic connectivity and mass transport properties of the catalyst layer.

The performance tests (polarization curve, ECSA and charge transfer resistance) ran in-situ showed that the catalyst slurry preparation influenced the electrochemical properties of the catalyst layers. The slow-drying rate methods (FDM and TDM) produced GV40 catalyst layers with the lowest potential losses due to the good ionomer dispersion and the optimal porous structure of these catalyst layers. GV40 FDM and GV40 TDM MEAs possessed the highest BoL ECSAs (56.42 m^2/g_{Pt} and 58.20 m^2/g_{Pt}, respectively) and the lowest charge transfer resistances. These electrochemical properties indicated the optimal formation of TPB sites with increased protonic and electronic connectivity. In contrast, significant potential losses were observed in the polarization curves of GV40 NDM and GV40 ASDM MEAs. This indicated a poor ionomer distribution and inhibited mass transport properties of the catalyst layers. These MEAs showed the lowest BoL ECSAs and the highest charge transfer resistances.

Similar performance and BoL ECSAs were observed between V40 TDM and V40 NDM indicating that the drying process was not required for V40 MEAs. However, V40 ASDM MEAs showed lower performance and BoL ECSA. This was due to the small ionomer-V40 interfaces formed during ASDM which decreased the active sites of the catalyst layers.

Despite the inefficient transport of nitrogen though the parallel flow field plate during AST, the half-MEA evaluation produced a trend for the hydroquinone-quinone capacitance that was conclusive. During AST in N_2, the hydroquinone-quinone capacitance increased to a maximum value in the early stress cycles before it linearly decreased. It was observed that catalyst layers with the highest resistance to carbon corrosion reached their maximum hydroquinone-quinone capacitances in the late cycles and slowly decreased to a lower percentage loss of their maximum values, such were the cases of GV40 TDM, V40 TDM and V40 NDM. The good ionomer dispersion and coverage in these catalyst layers insulated the carbon support from water and induced corrosion.

The conclusions could address the knowledge gap described as questions in Chapter 1, section 4. The drying process allowed the reconfiguration, attachment, and distribution of the ionomer onto the supported catalyst which results in the formation of large ionomer-supported catalyst interfaces and provides the protonic connectivity at the active sites. The drying process dictates the pore structure of the catalyst layer which improves its mass transport properties. However, with the FDM, it can be concluded that it is not about the temperature, but rather the slow drying rate which provides the ionomer and the supported catalyst with maximum contact time. The drying rate plays a key role in the ionomer-GV40 optimal interactions, fast-drying rate method (ASDM) resulted in small ionomer-supported catalyst interfaces and a poor porous structure of the catalyst layers. This was due to the fast drying of the solvent with no time for the ionomer to interact with the supported catalyst and resulted in a poor ionomer distribution and coverage. The drying process during GV40 slurry preparation is therefore essential to produce MEAs with benchmark performance. Only with a less hydrophobic support such as Vulcan, can the catalyst slurry be prepared with no drying process. This is due to the interactions between the side-chain of the ionomer and Vulcan which results in large ionomer-V40 interfaces.

1.2.   Recommendations

Due to time limitations, the following recommendations are made:

1. Usage of a rotary evaporator which might help to reduce the drying time and force ionomer-supported catalyst contact during rotation. A vacuum oven can also be an alternative.
2. Usage of X-ray photoelectron spectroscopy (XPS) and scanning electron microscopy colour energy-dispersive X-ray spectroscopy (SEM-EDS) to investigate the structure and orientation of the ionomer.
3. To determine the specific surface area (SSA) of the catalyst coated membrane (CCM) which would be used to estimate the Pt utilization (ECSA/SSA) of CCMs prepared by different catalyst slurry preparation methods.
4. To study in-situ the durability of MEAs produced by different catalyst slurry preparation methods.
5. To improve the design of the half-MEA flow field plate for a more efficient transport of reagents through the catalyst layer and to investigate the impacts of the electrolyte temperature (H_2SO_4 in the pool), the gas humidity and flow rate on the measurements (ECSA and AST).

1.3.   Research impact

The knowledge acquired through this study, provides insight on the impact of the catalyst slurry preparation method on the MEA performance. The study presents physical and electrochemical techniques (including the half-MEA cell) that need to be used to study the structure and properties of the catalyst layer. With the understanding, the current catalyst slurry preparation method can be optimized to be time-efficient.

The preliminary results of this work were presented in the seminar on Nanotechnology in August 2019, at the Cape peninsula university of technology.

This study generated a thesis for the degree Master of Engineering. The findings and conclusions of this study are being summarised in a scientific paper and will be submitted to the Advanced Functional Materials for a review and a possible publication.

The title of the paper: Understanding the impact of the catalyst ink preparation on the ionomer-supported catalyst interactions and MEA performance in PEMFCs.

The authors: Bamato Jonathan Itota, Dr. Jessica Chamier (UCT), Dr. Mahabubur Chowdhury (CPUT) and Dr. Olivia Barron (UWC).

References

Aksakal, C. and Sisman, A. (2018) 'On the Compatibility of Electric Equivalent Circuit Models for Enhanced Flooded Lead Acid Batteries Based on Electrochemical Impedance Spectroscopy'. doi: 10.3390/en11010118.

Andersen, S. M. *et al.* (2014) 'Adsorption Behavior of Per fl uorinated Sulfonic Acid Ionomer on Highly Graphitized Carbon Nano fi bers and Their Thermal Stabilities'. doi: 10.1021/jp501088d.

Andersen, S. M. (2016) 'Applied Catalysis B : Environmental Nano carbon supported platinum catalyst interaction behavior with perfluorosulfonic acid ionomer and their interface structures', *'Applied Catalysis B, Environmental'*. Elsevier B.V., 181, pp. 146–155. doi: 10.1016/j.apcatb.2015.07.049.

Berg, P., Novruzi, A. and Promislow, K. (2006) 'Analysis of a cathode catalyst layer model for a polymer electrolyte fuel cell', 61, pp. 4316–4331. doi: 10.1016/j.ces.2006.01.033.

Carrette, L., Kaspar Andreas, F. and Ulrich, S. (2001) 'Fuel Cells - Fundamentals and Applications', *Fuel Cells*, 1(1), pp. 5–39.

Carter, R. N. *et al.* (2007) 'Artifacts in measuring electrode catalyst area of fuel cells through cyclic voltammetry', *ECS Transactions*, 11(1 PART 1), pp. 403–410. doi: 10.1149/1.2780954.

Castanheira, L. *et al.* (2015) 'Carbon corrosion in proton-exchange membrane fuel cells: Effect of the carbon structure, the degradation protocol, and the gas atmosphere', *ACS Catalysis*, 5(4), pp. 2184–2194. doi: 10.1021/cs501973j.

Christie John, G. (1993) *Transport Process and Unit Operations*. Third. Edited by I. Prentice Hall international. new jersey: entice Hall international, Inc.

Cindrella, L. *et al.* (2009) 'Gas diffusion layer for proton exchange membrane fuel cells-A review', *Journal of Power Sources*, 194(1), pp. 146–160. doi: 10.1016/j.jpowsour.2009.04.005.

Danilczuk, M. *et al.* (2011) 'Understanding the fingerprint region in the infra-red spectra of perfluorinated ionomer membranes and corresponding model compounds : Experiments and theoretical calculations', *Journal of Power Sources*. Elsevier B.V., 196(20), pp. 8216–8224. doi: 10.1016/j.jpowsour.2011.05.067.

Dychalska, A., Popielarski, P. and Fabisiak, K. (2015) 'Study of CVD diamond layers with amorphous carbon admixture by Raman Study of CVD diamond layers with amorphous carbon admixture by Raman scattering spectroscopy', (November). doi: 10.1515/msp-2015-0067.

Hanawa, H. *et al.* (2012) 'In Situ ATR-FTIR Analysis of the Structure of Na fi on − Pt / C and Na fi on − Pt 3 Co / C Interfaces in Fuel Cell'. doi: 10.1021/jp306955q.

Hodkiewicz, J. and Scientific, T. F. (2010) 'Characterizing Carbon Materials with Raman Spectroscopy', *Thermo Fischer Scientific*, pp. 1–5.

Holdcroft, S. (2014) 'Fuel Cell Catalyst Layers: A Polymer Science Perspective'. doi: 10.1021/cm401445h.

Holton, B. O. T. and Stevenson, J. W. (2013) 'The Role of Platinum in Proton Exchange Membrane Fuel Cells', (4), pp. 259–271.

Jang, J. H. *et al.* (2009) 'Complex Capacitance Analysis of Ionic Resistance and Interfacial Capacitance in PEMFC and DMFC Catalyst Layers'. doi: 10.1149/1.3187928.

Kim, K. *et al.* (2010) 'The effects of Nafion Ò ionomer content in PEMFC MEAs prepared by a catalyst-coated membrane (CCM) spraying method', *International Journal of Hydrogen Energy*. Elsevier Ltd, 35(5), pp. 2119–2126. doi: 10.1016/j.ijhydene.2009.11.058.

Kim, T. *et al.* (2016) 'ScienceDirect Solvent effect on the Nafion agglomerate morphology in the catalyst layer of the proton exchange membrane fuel cells', *International Journal of Hydrogen Energy*. Elsevier Ltd, 42(1), pp. 478–485. doi: 10.1016/j.ijhydene.2016.12.015.

Kunusch, C., Puleston, P. and Mayosky, M. A. (2012) *Sliding-Mode Control of PEM Fuel Cells*. New York: SPRINGER DORDRECHT HEIDELBERG LONDON NEW YORK. doi: 10.1007/978-1-4471-2431-3.

Lim, J. W. *et al.* (2012) 'Ionic Resistance of a Cathode Catalyst Layer with Various Thicknesses by Electrochemical Impedance Spectroscopy for PEMFC', *Journal of The Electrochemical Society*, 159(4), pp. B378–B384. doi: 10.1149/2.030204jes.

Mathias, M. (2005) 'Two Fuel Cell Cars In', (September).

Orazem, M. E. and Tribollet, B. (2017) *Electrochemical impedance spectroscopy*. 2nd edn. new jersey: Wiley. Available at: https://books.google.co.za/books?lr=&id=1KilDgAAQBAJ&dq=Electrochemical+Impedance+Spectroscopy%2C+M.E.+Orazem+and+Bernard+Tribollet%2C+John+Wiley+%26+Sons%2C+2008.&q=tags#v=onepage&q=tags&f=false.

Peschel, G. (2011) 'Carbon - Carbon bonds: Hybridization', 2, pp. 1–6.

Pletcher, D. (2019) *A first course in electrode processes*. Royal Society of Chemistry.

Pozio, A. *et al.* (2002) 'Comparison of high surface Pt / C catalysts by cyclic voltammetry', 105(March 2001), pp. 13–19.

Rosa, A. da (2013) *Fundamentals of Renewable Energy Processes*. 3rd edn. Edited by A. da Rosa. Academic press. doi: 10.1016/B978-0-12-397219-4.00009-6.

Saleh, F. S. and Easton, E. B. (2012) 'Diagnosing Degradation within PEM Fuel Cell Catalyst Layers Using Electrochemical Impedance Spectroscopy particles Nafion ionomer Carbon support', 159(5), pp. 546–553. doi: 10.1149/2.098205jes.

Sedaghat, A. *et al.* (2013) 'Performance assessment of a hybrid fuel cell and micro gas turbine power system', *Energy Equipment and Systems*, 1(1), pp. 59–74. doi: 10.22059/ees.2013.2740.

Sevjidsuren, G. *et al.* (2010) 'Effect of Different Support Morphologies and Pt Particle Sizes in Electrocatalysts for Fuel Cell Applications', 2010. doi: 10.1155/2010/852786.

Sharma, R. and Andersen, S. M. (2018) 'Quanti fi cation on Degradation Mechanisms of Polymer Electrolyte Membrane Fuel Cell Catalyst Layers during an Accelerated Stress Test', 30. doi: 10.1021/acscatal.8b00002.

Stevenson, M. L. and Pattrick, G. (2017) 'Alternative carbon materials as practical and more durable fuel cell electrocatalyst supports than conventional carbon blacks', *Journal of the Southern African Institute of Mining and Metallurgy*, 117(10), pp. 989–995. doi: 10.17159/2411-9717/2017/v117n10a10.

Tan, Y. *et al.* (2019) 'Hydration Behavior of Magnesium Oxysulfate Cement with Fly Ash via Electrochemical Impedance Spectroscopy', 31(10), pp. 1–11. doi: 10.1061/(ASCE)MT.1943-5533.0002827.

Tang, H. *et al.* (2006) 'PEM fuel cell cathode carbon corrosion due to the formation of air / fuel boundary at the anode', 158, pp. 1306–1312. doi: 10.1016/j.jpowsour.2005.10.059.

Valent, O., Koryta, J. and Panoch, M. (1987) 'Elsevier Sequoia S.A., Lausamre - Printed in The Netherlands', *Journal of Electroanalytical Chemistry*, 226, pp. 21–25.

Wang, Wentao *et al.* (2015) 'ScienceDirect Fabrication of catalyst coated membrane with screen printing method in a proton exchange membrane fuel cell', *International Journal of Hydrogen Energy*. Elsevier Ltd, 40(13), pp. 4649–4658. doi: 10.1016/j.ijhydene.2015.02.027.

Wee, J., Lee, K. and Kim, S. H. (2007) 'Fabrication methods for low-Pt-loading electrocatalysts in proton exchange membrane fuel cell systems', 165, pp. 667–677. doi: 10.1016/j.jpowsour.2006.12.051.

Yadav, A. P. (2013) 'Estimation of Active Surface Area of Platinum by Electrochemical Impedance Spectroscopy', *International Journal of Chemical Studies*, 1(3), pp. 1–4. Available at: www.chemijournal.com.

A. Appendix A

A.1. Scanning electron microscopy

These are the SEM images of GV40 CCMs and V40 CCMs:
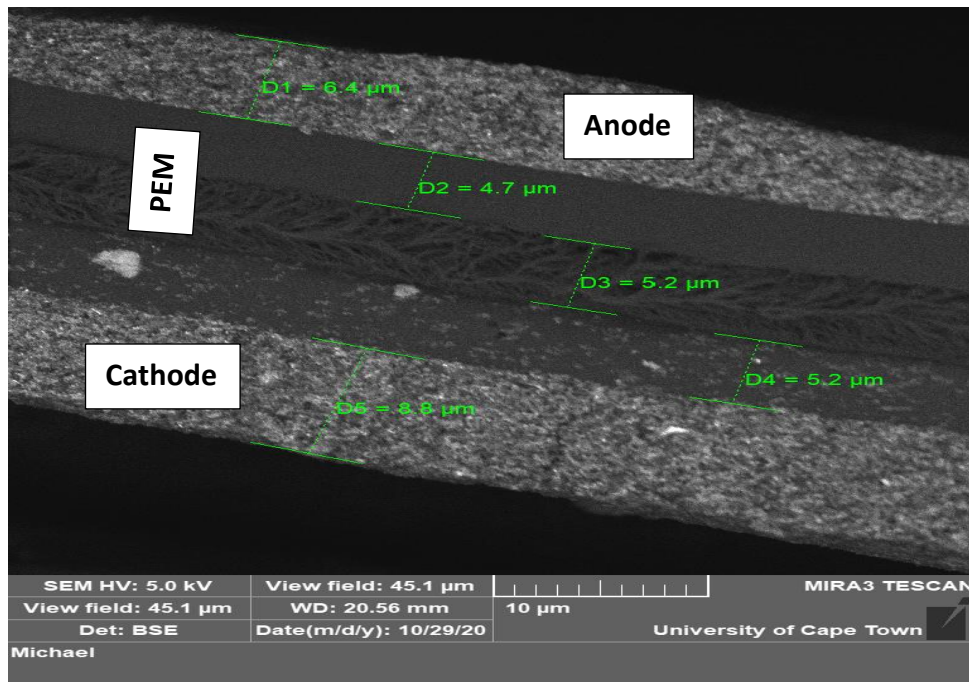
Figure A.1: SEM image of GV40 NDM CCM.
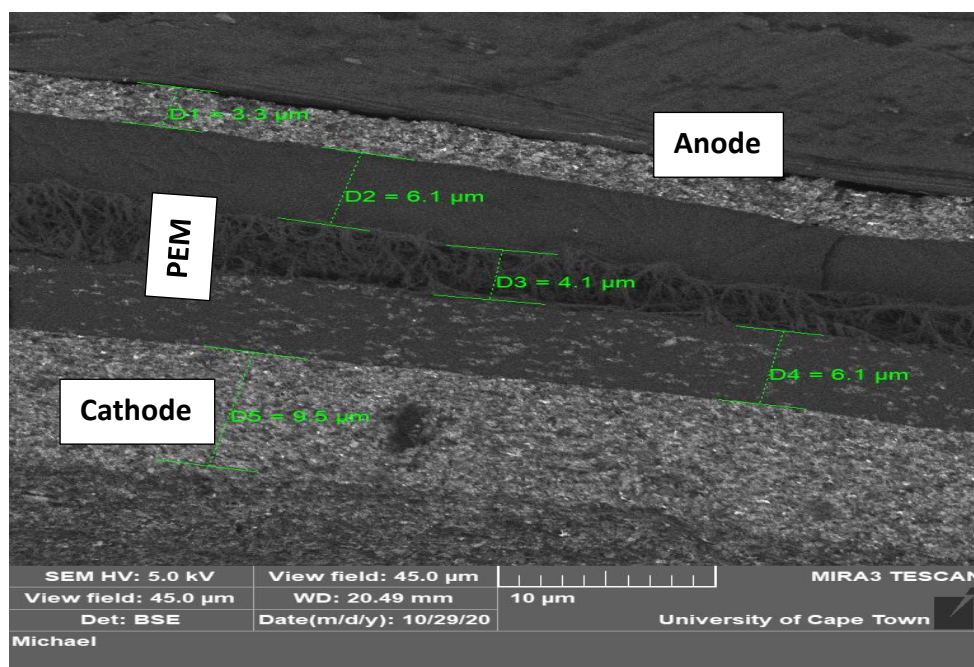
Figure A.2: SEM image of GV40 ASDM CCM.
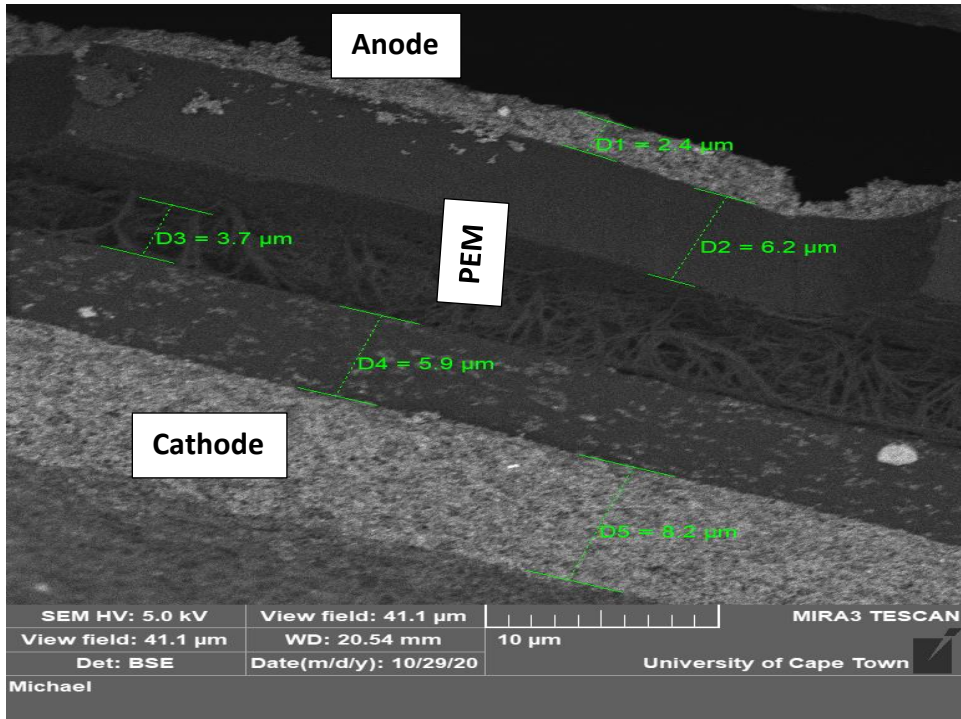
Figure A.3: SEM image of V40 TDM CCM.
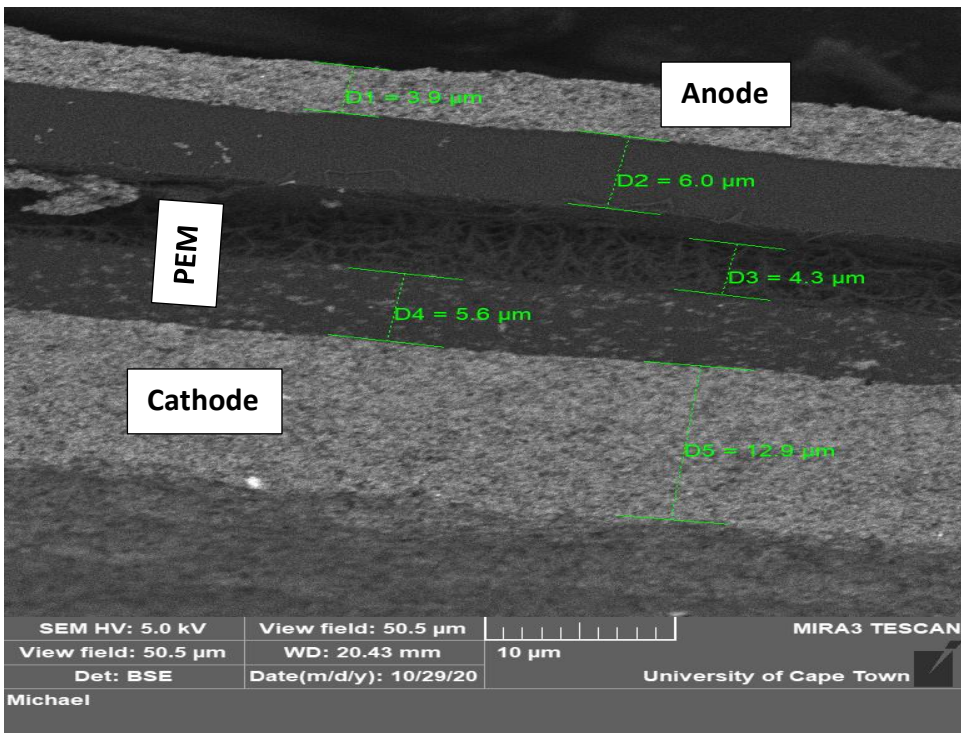
Figure A.4: SEM image of V40 NDM CCM.
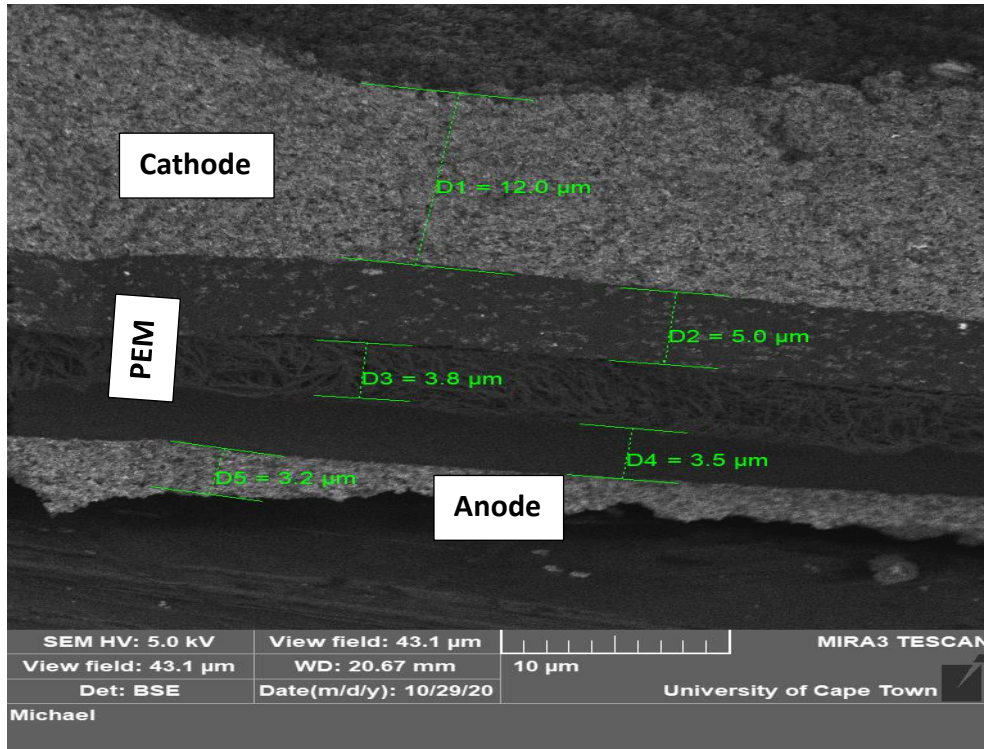
Figure A.5: SEM image of V40 ASDM CCM.

A.2.   Cyclic voltammetry

The cyclic voltammograms of GV40 MEAs and V40 MEAs are shown in Figures A.6 and A.7 respectively:
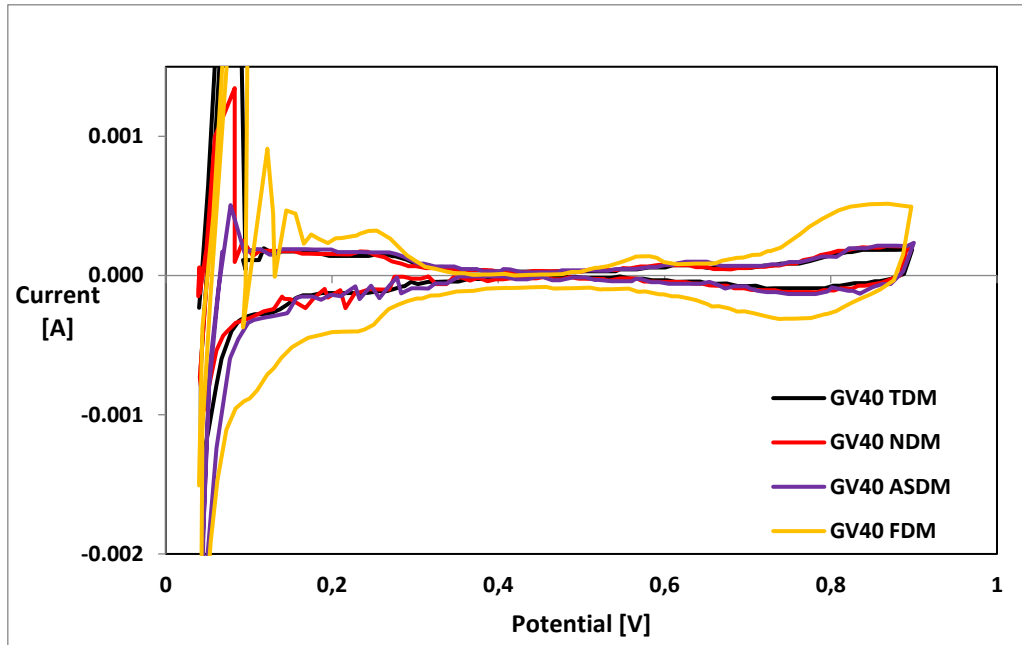
Figure A.6: cyclic voltammograms of GV40 MEAs under 100% RH.
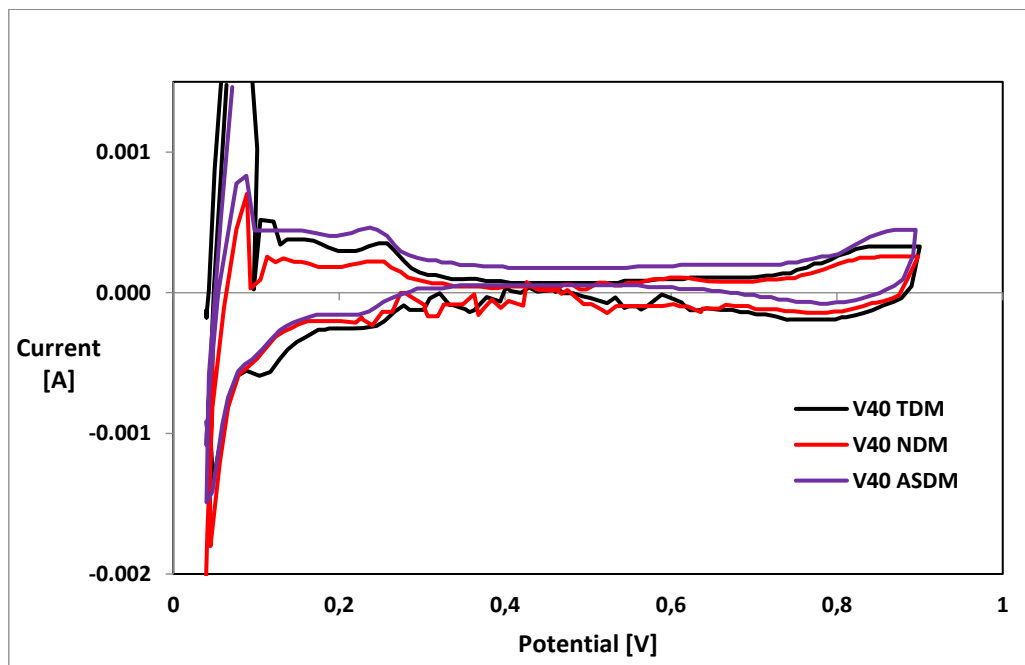
Figure A.7: cyclic voltammograms of V40 MEAs under 100% RH.

A.3.   Polarization and power curves

The polarization and power curves of GV40 and V40 MEAs under 100% RH, 74% RH and 65% RH.
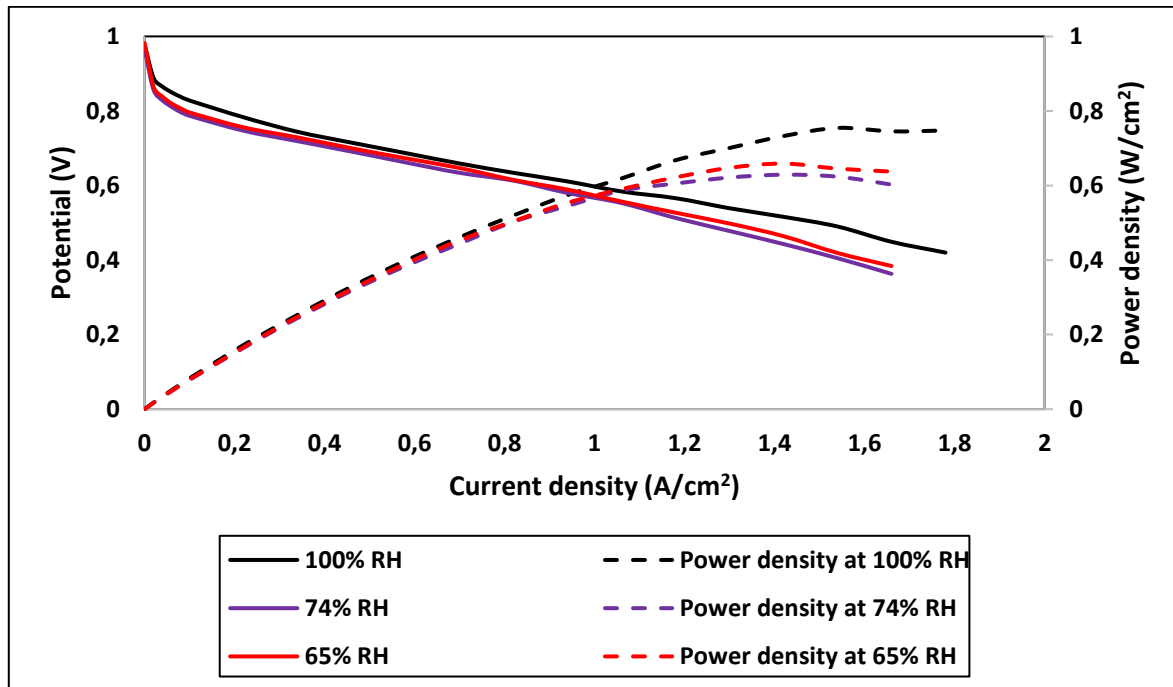
Figure A.8: GV40 TDM polarization curve under three RH conditions.
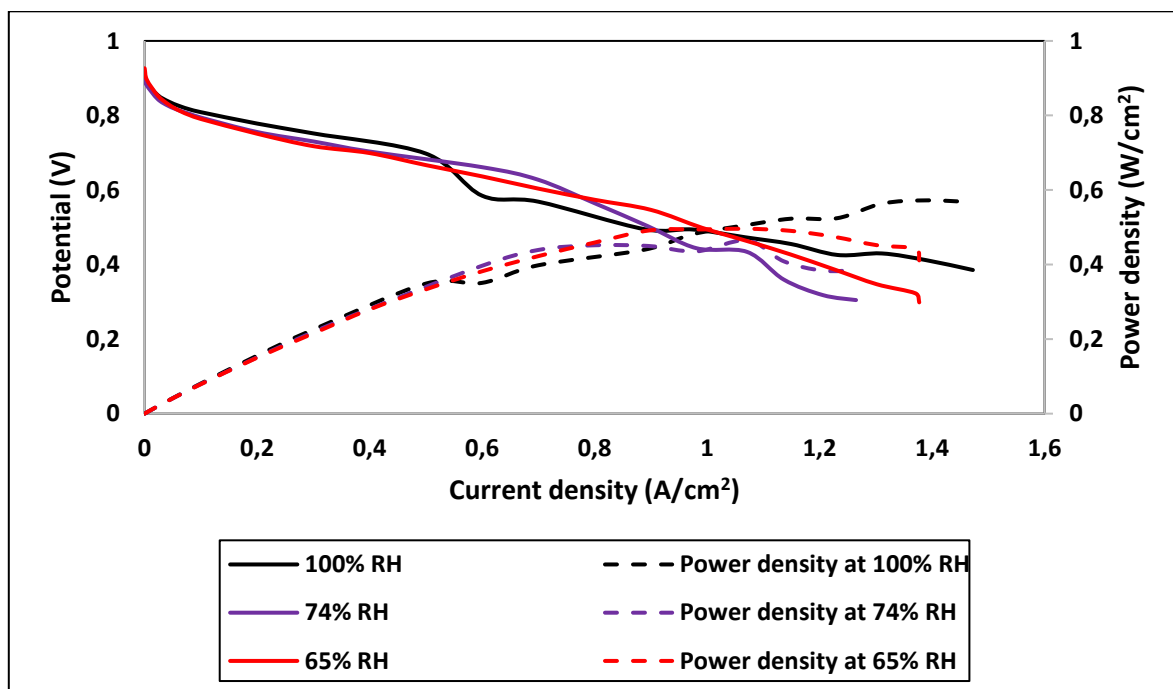
Figure A.9: GV40 TDM polarization curve under three RH conditions.
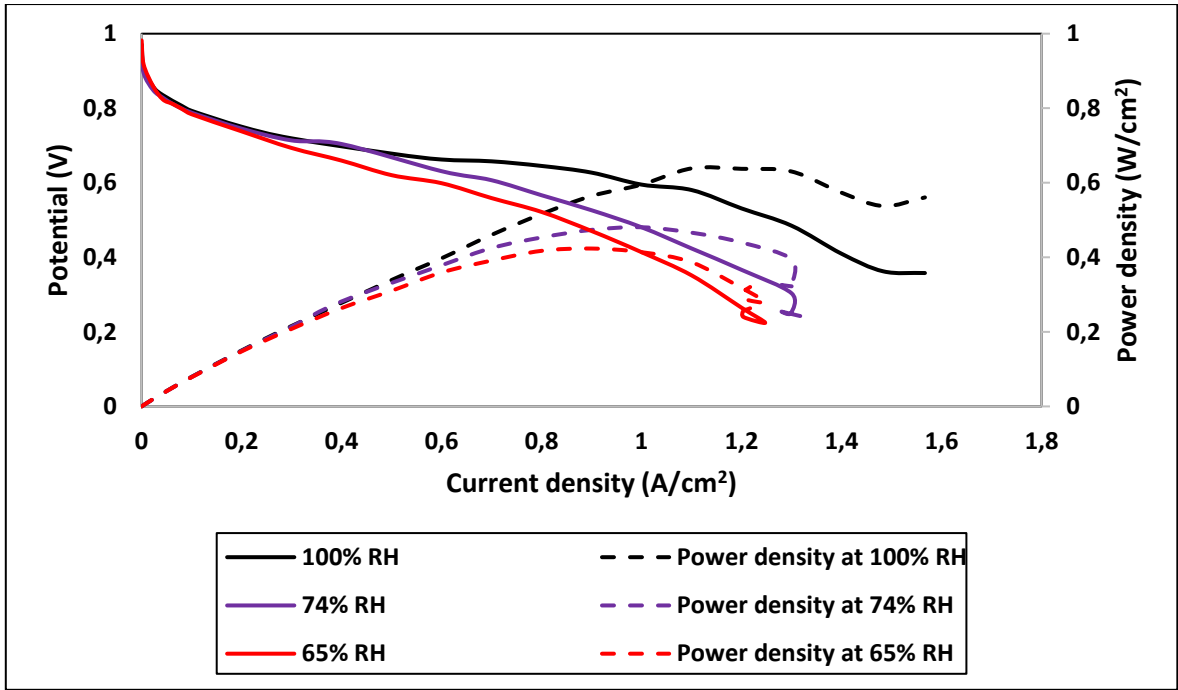
Figure A.10: GV40 ASDM polarization curve under three RH conditions.
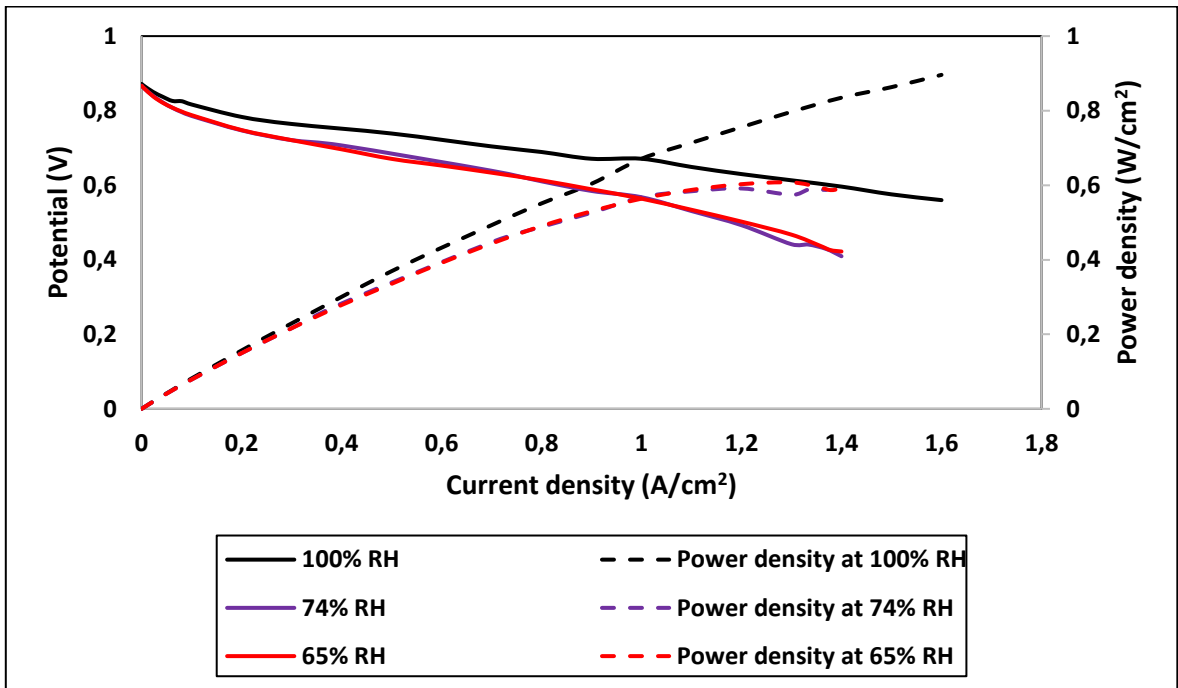
Figure A.11: GV40 FDM polarization curve under three RH conditions.
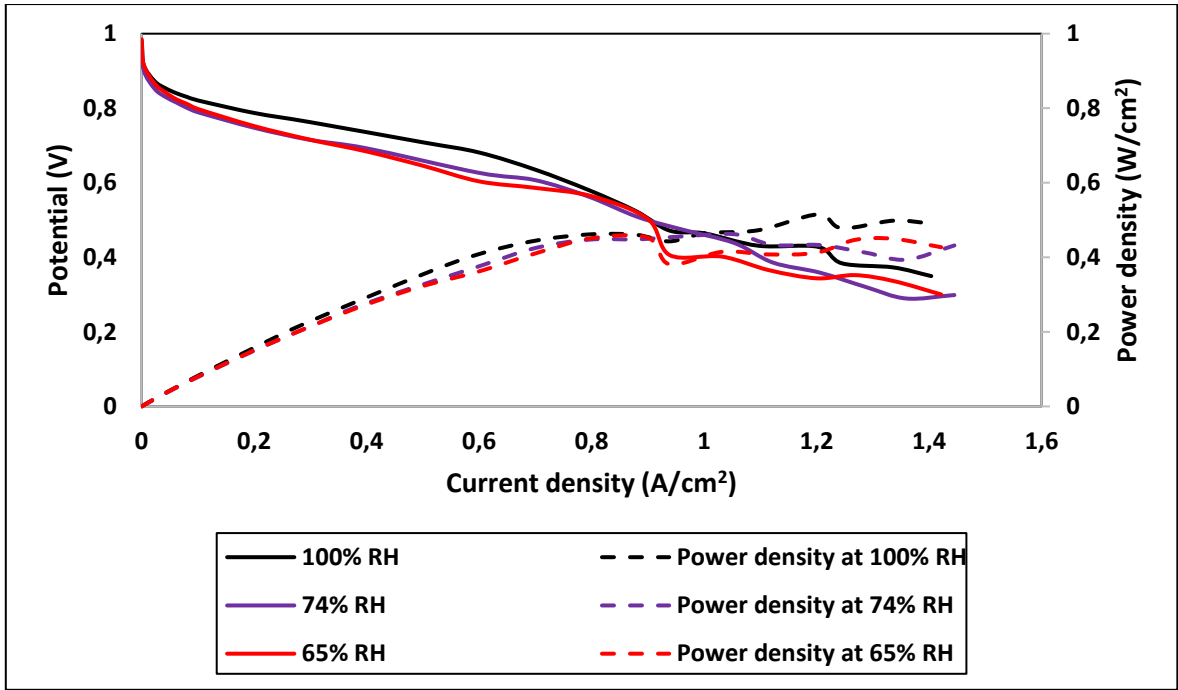
Figure A.12: V40 TDM polarization curve under three RH conditions.
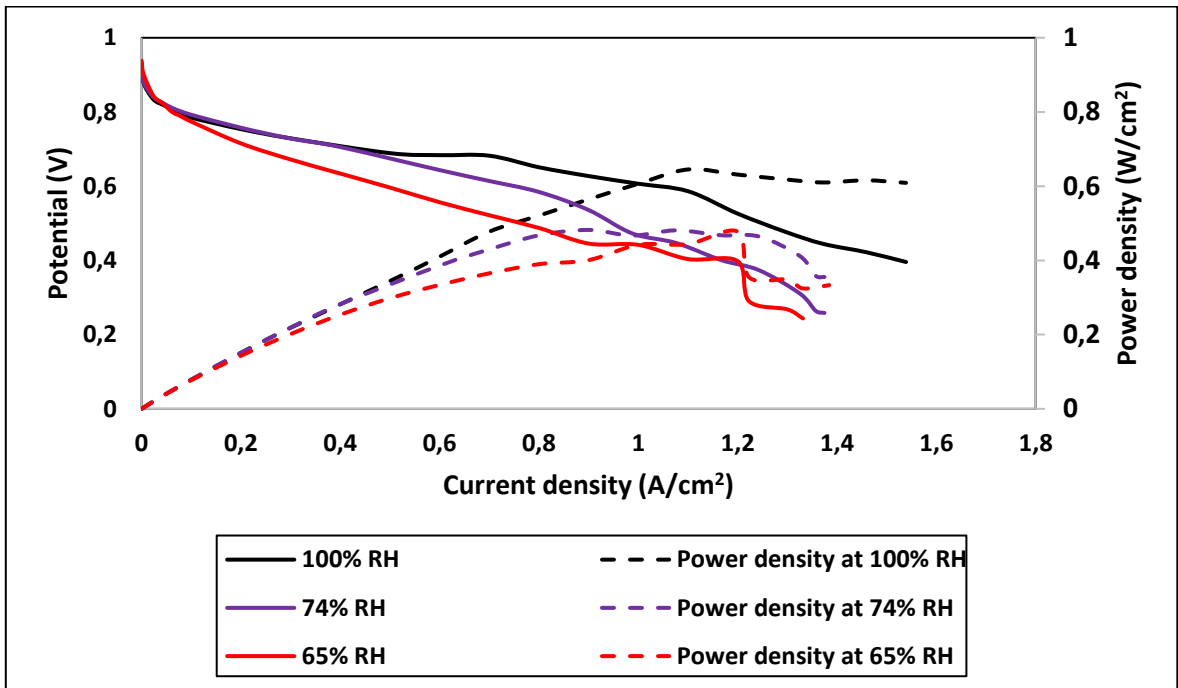
Figure A.13: V40 NDM polarization curve under three RH conditions.
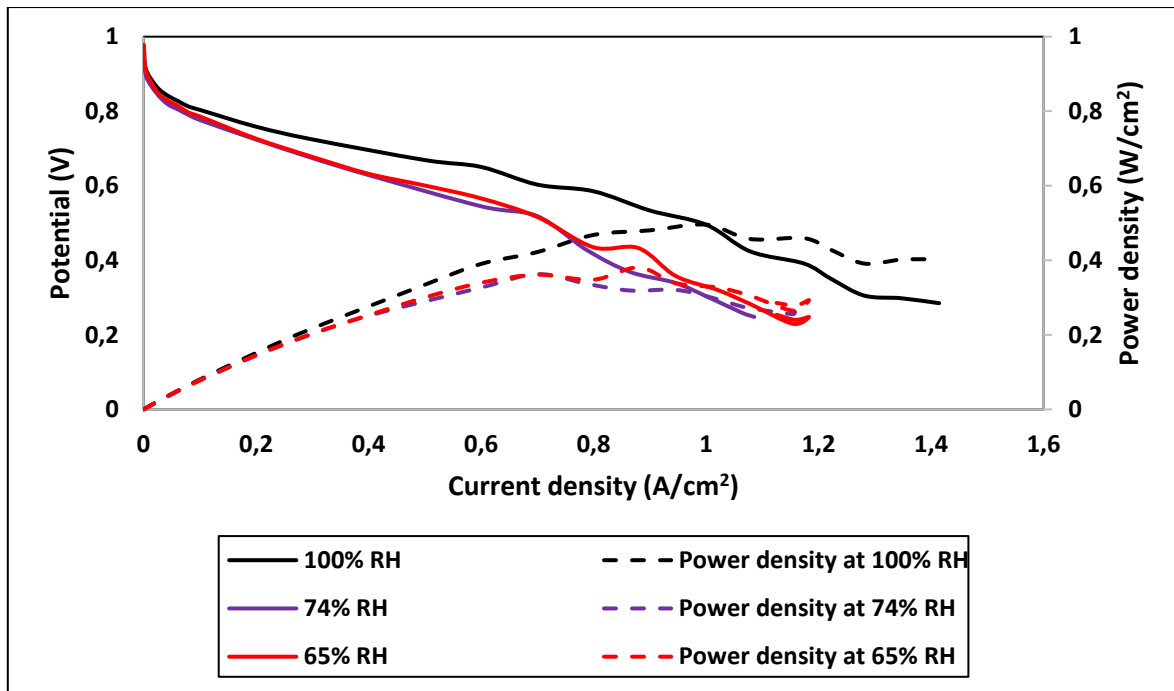
Figure A.14: V40 ASDM polarization curve under three conditions

B. Appendix B

B.1.   Cyclic voltammetry during AST in oxygen

The cyclic voltammograms of GV40 half-MEAs and V40 half-MEAs during AST in oxygen.
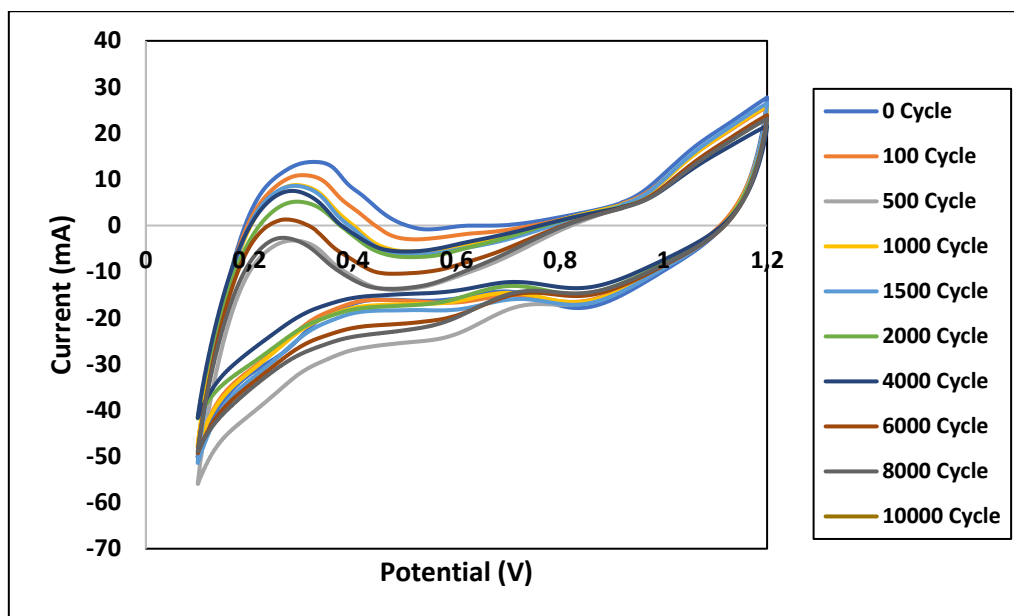
Figure B.1: Cyclic voltammograms of GV40 TDM half-MEA recorded after stress cycles in O_2.
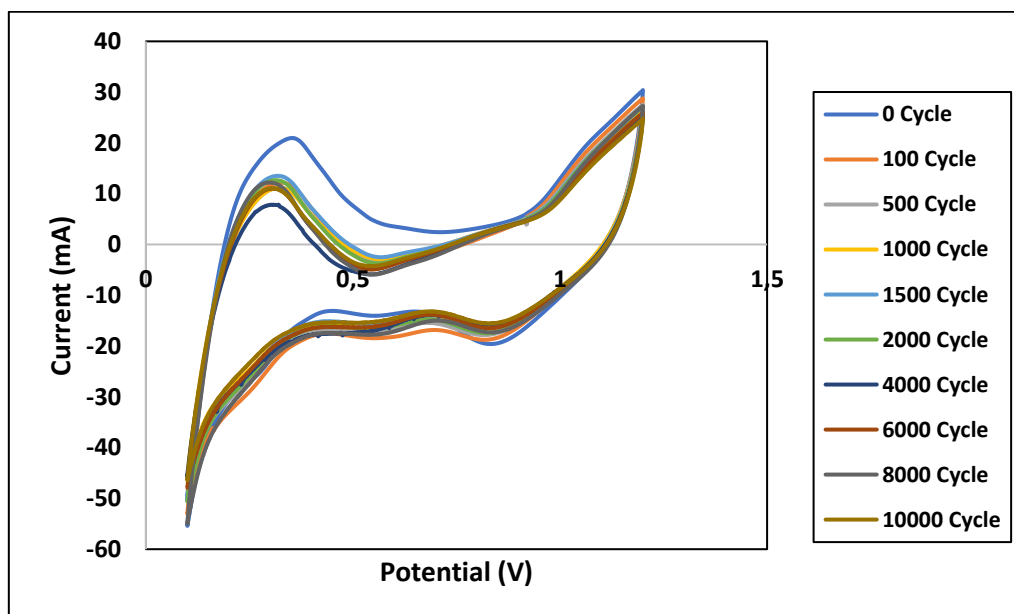
Figure B.2: Cyclic voltammograms of GV40 NDM half-MEA recorded after stress cycles in O_2.
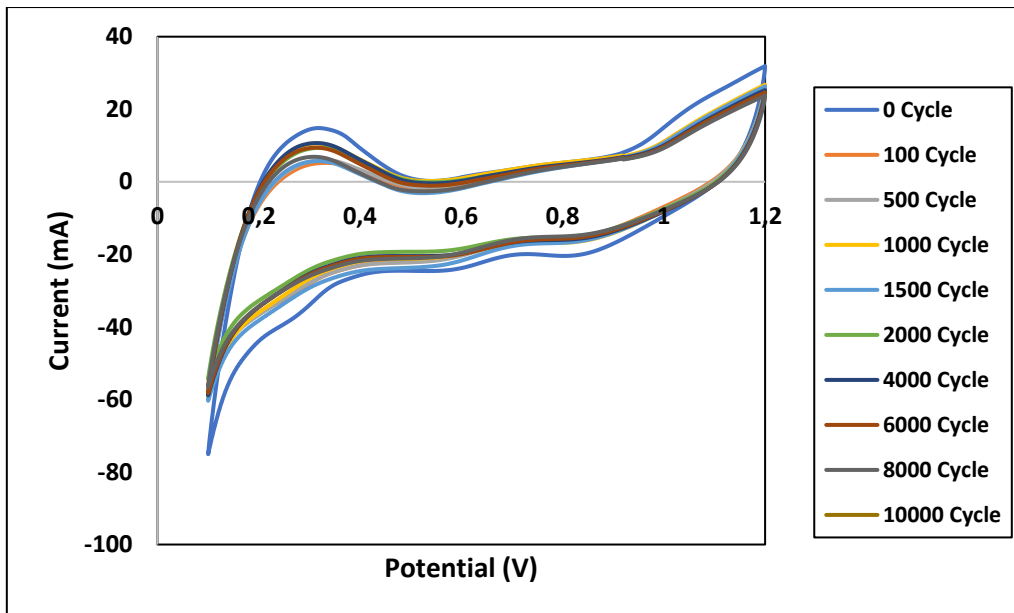
Figure B.3: Cyclic voltammograms of V40 TDM half-MEA recorded after stress cycles in O₂.
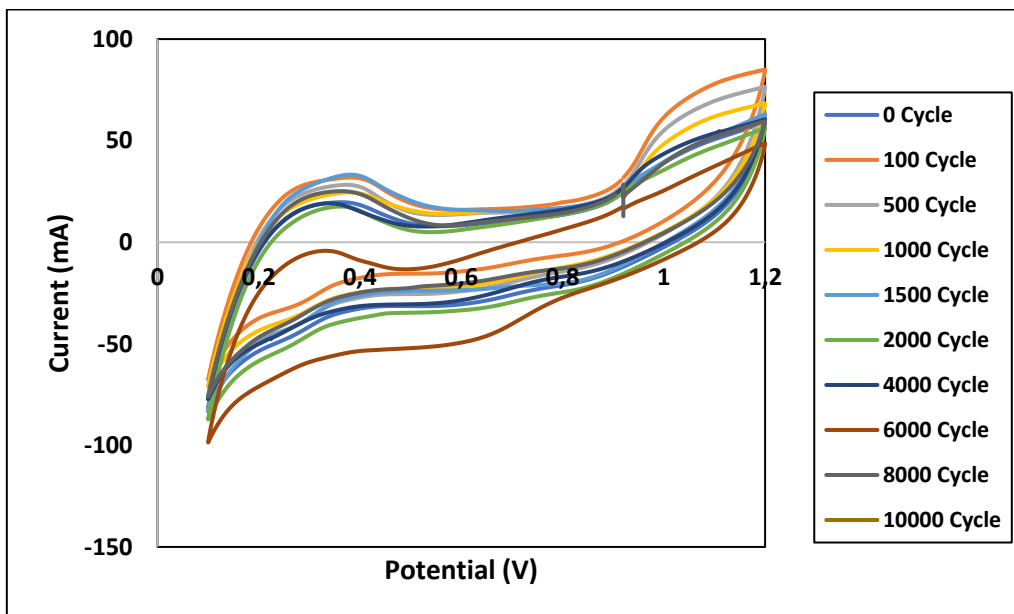
Figure B.4: Cyclic voltammograms of V40 NDM half-MEA recorded after stress cycles in O₂.
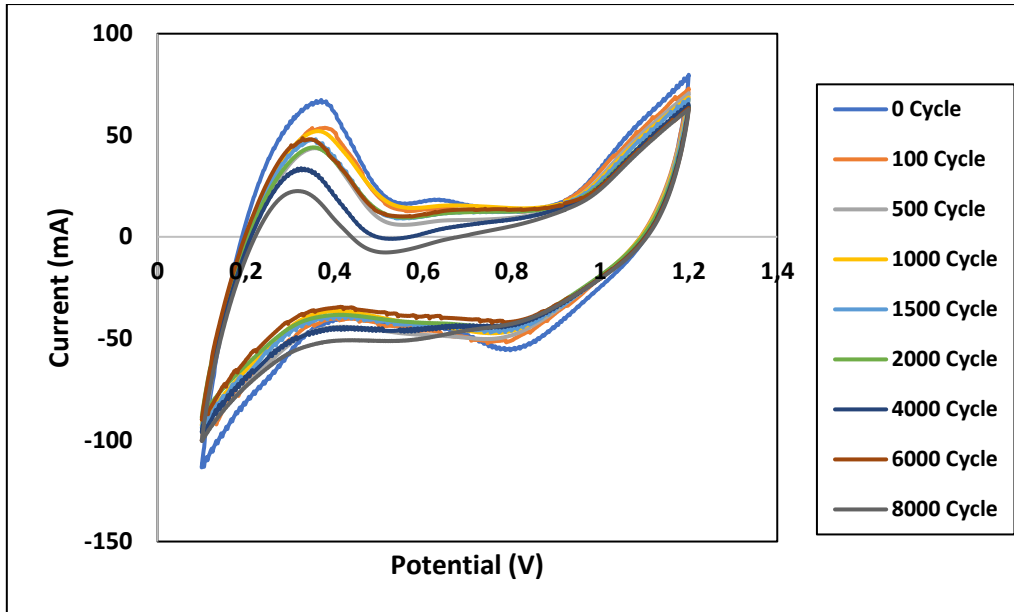
Figure B.5: Cyclic voltammograms of V40 ASDM half-MEA recorded after stress cycles in O₂.

B.2. Cyclic voltammetry during AST in nitrogen

The cyclic voltammograms of GV40 half-MEAs and V40 half-MEAs during AST in oxygen.
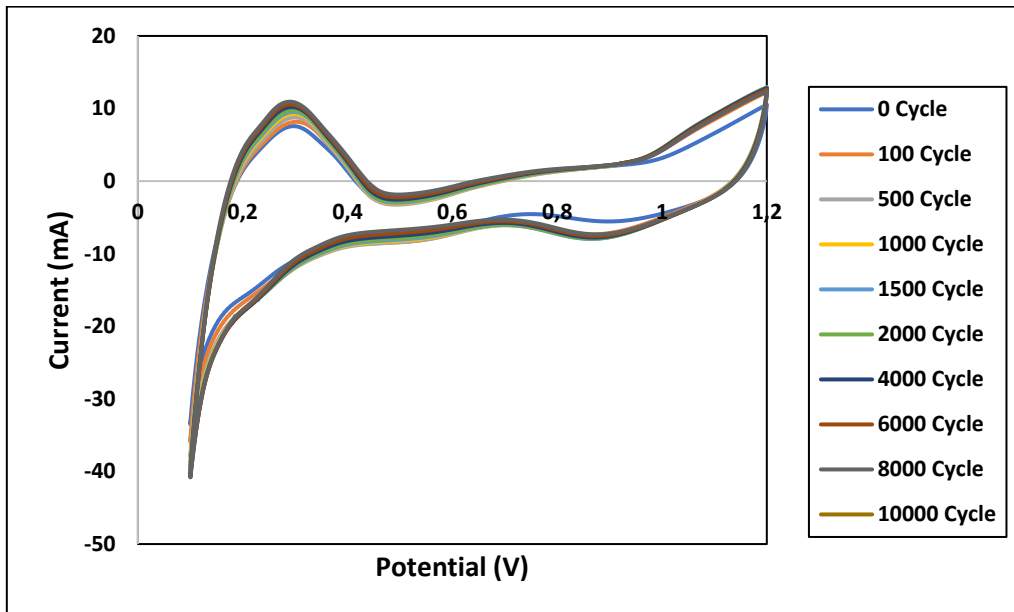
Figure B.6: Cyclic voltammograms of GV40 TDM half-MEA recorded after stress cycles in N₂.
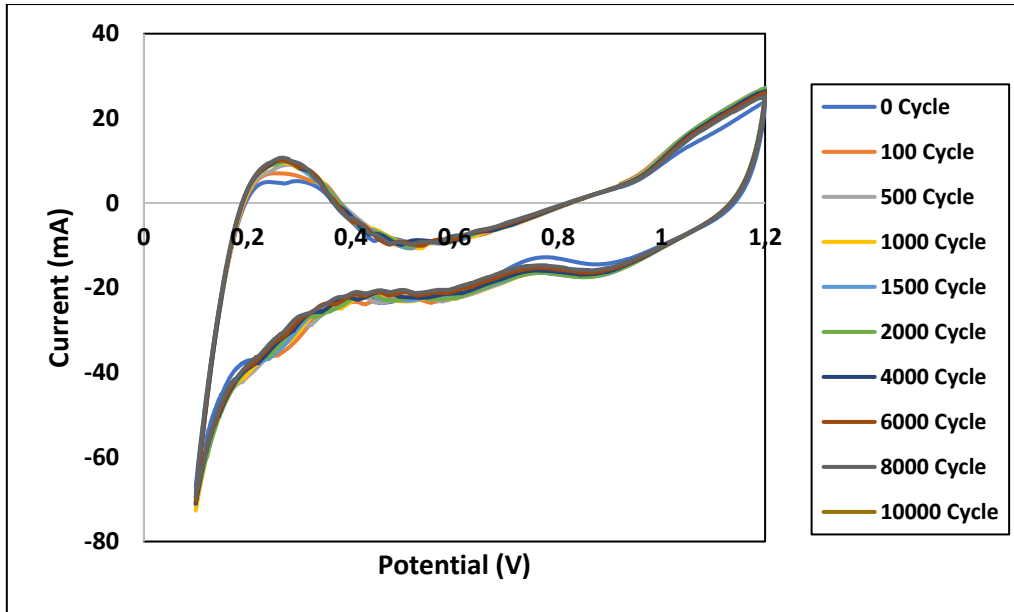
Figure B.7: Cyclic voltammograms of GV40 NDM half-MEA recorded after stress cycles in N$_2$.
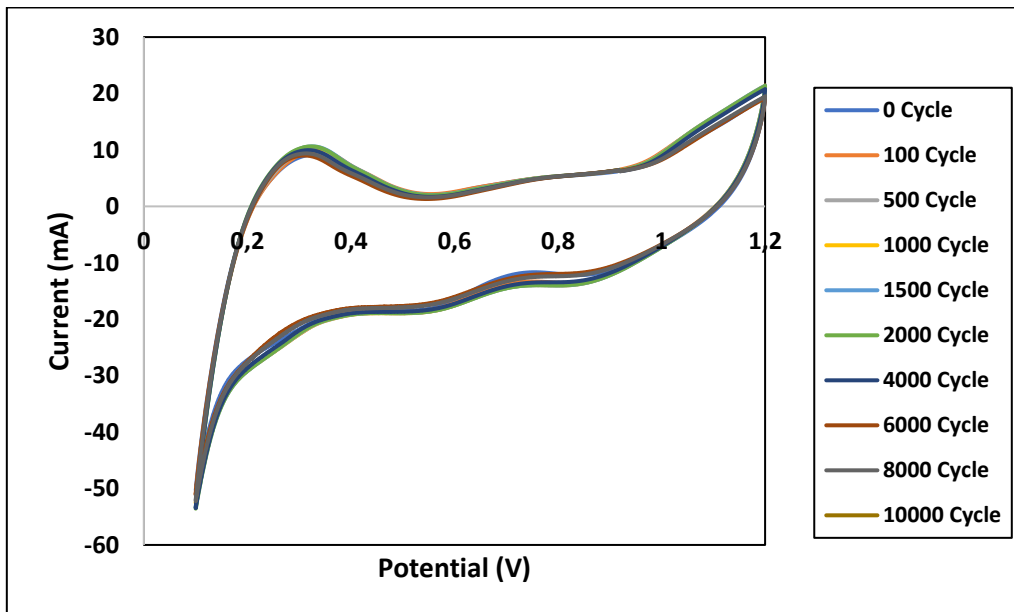
Figure B.8: Cyclic voltammograms of V40 TDM half-MEA recorded after stress cycles in N$_2$.
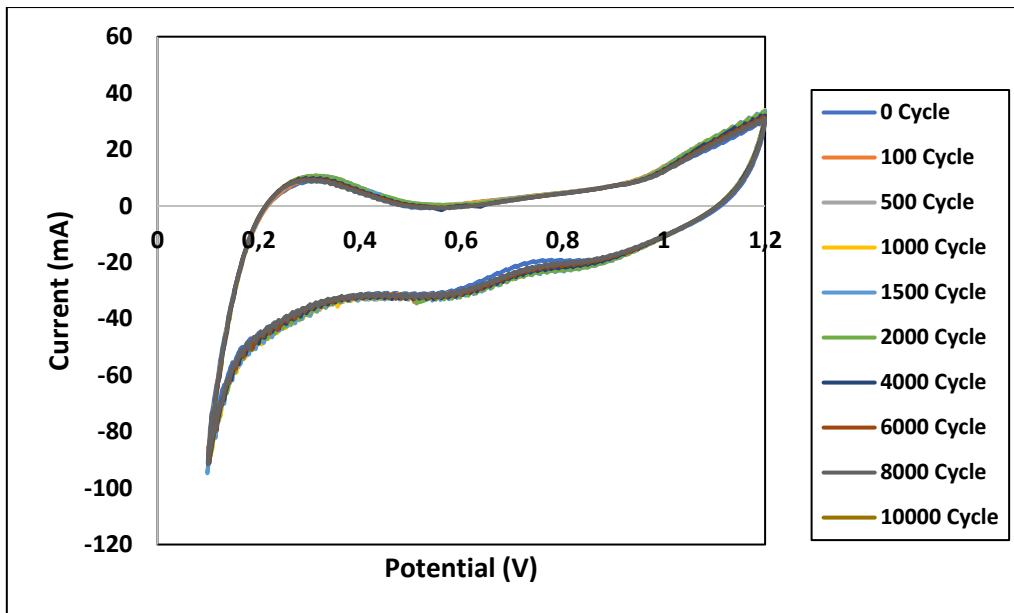
Figure B.9: Cyclic voltammograms of V40 NDM half-MEA recorded after stress cycles in N_2.
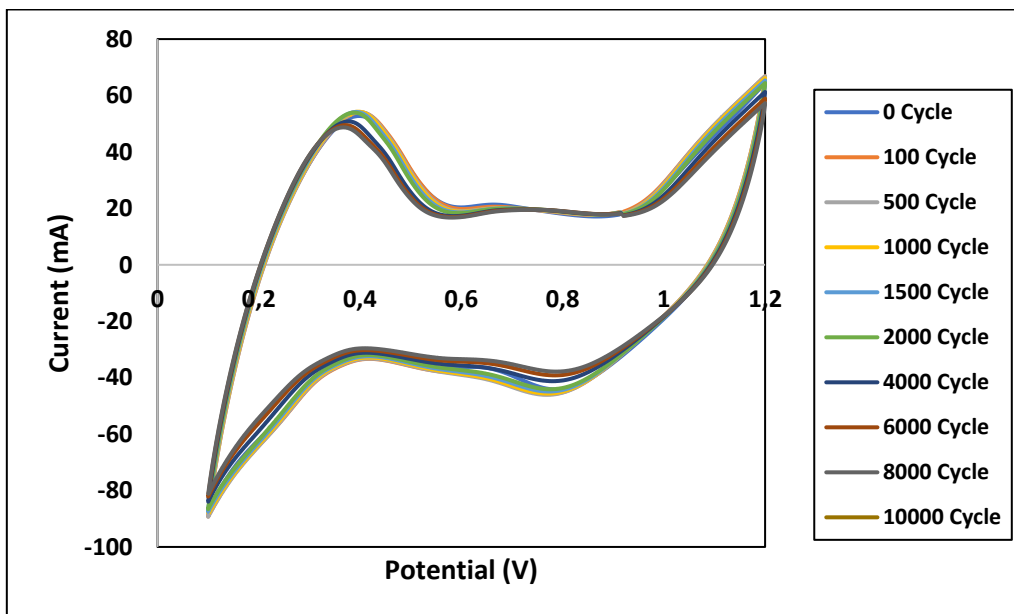
Figure B.10: Cyclic voltammograms of V40 ASDM half-MEA recorded after stress cycles in N_2.

B.3. Electrochemical impedance spectroscopy during AST in nitrogen

The Nyquist plots of GV40 and V40 half-MEAs as functions of stress cycle.
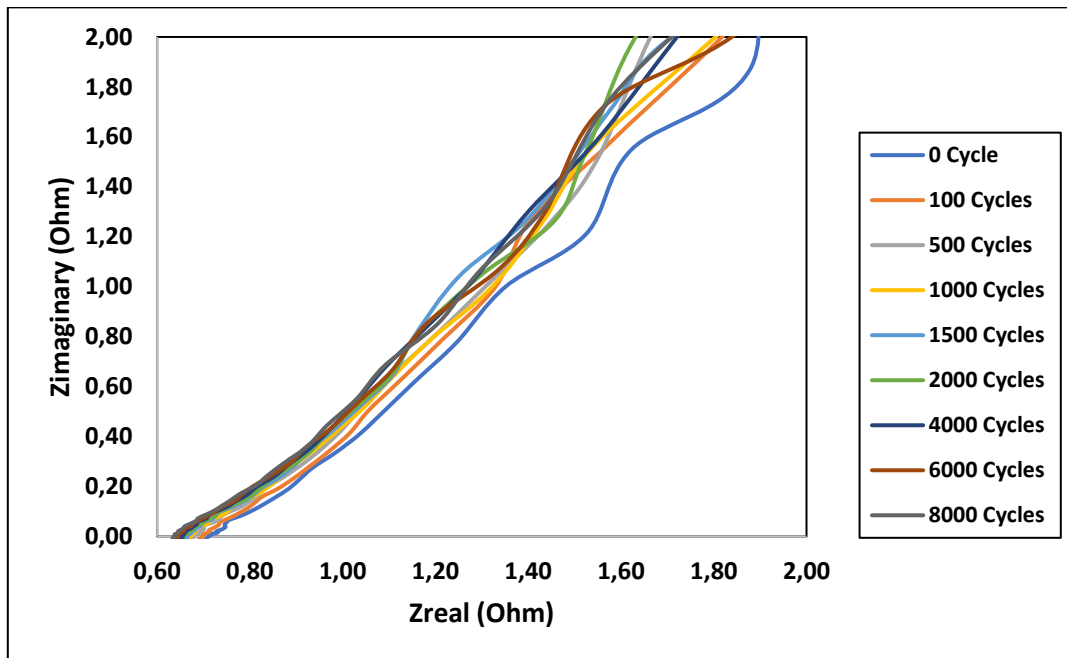
Figure B.11: Nyquist plots during AST of GV40 NDM half-MEA.
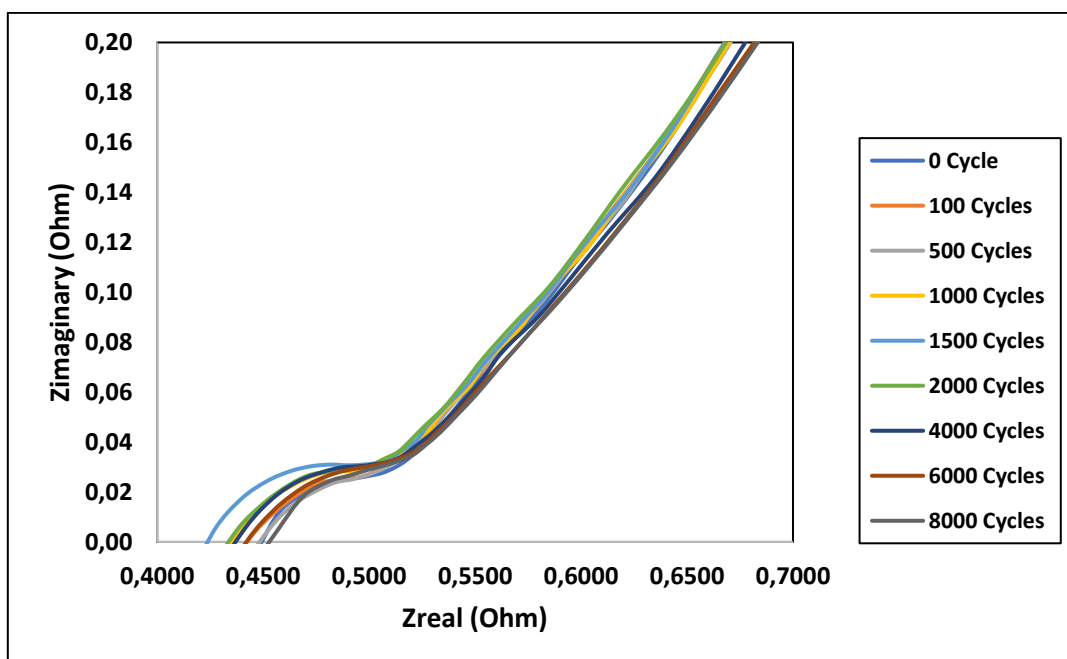
Figure B.12: Nyquist plots during AST of GV40 ASDM half-MEA.
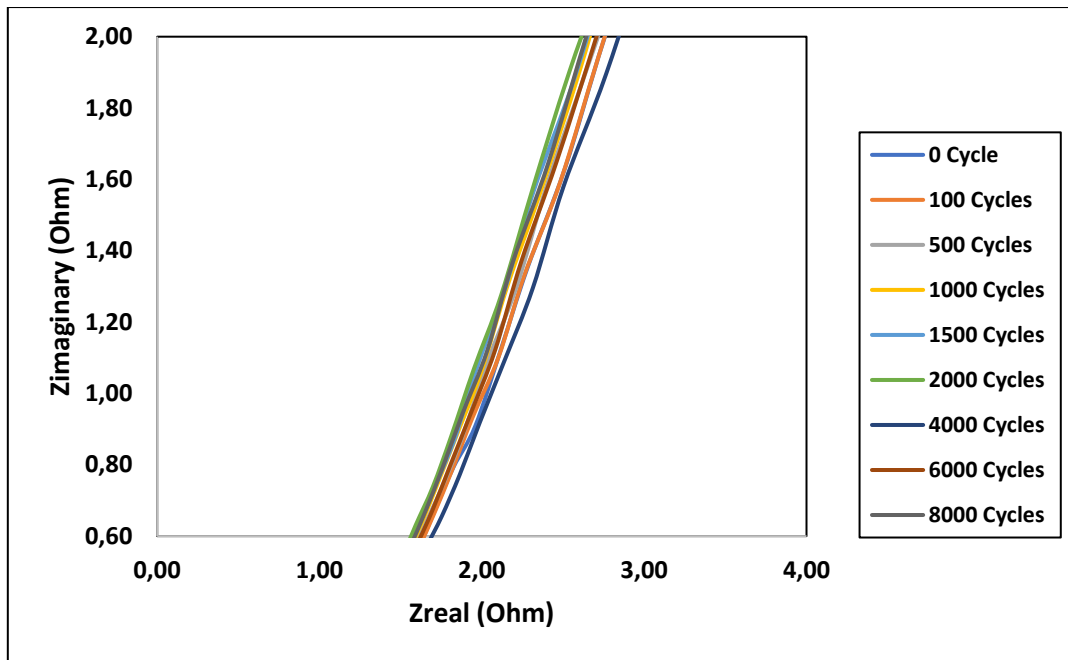
Figure B.13: Nyquist plots during AST of V40 TDM half-MEA.
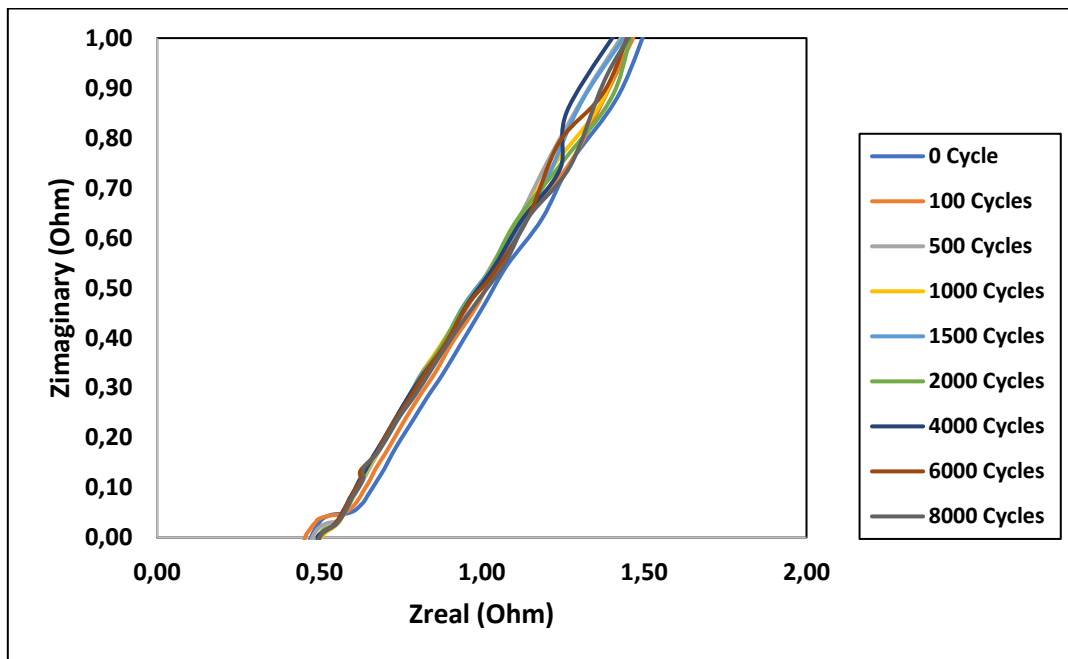
Figure B.14: Nyquist plots during AST of V40 NDM half-MEA.
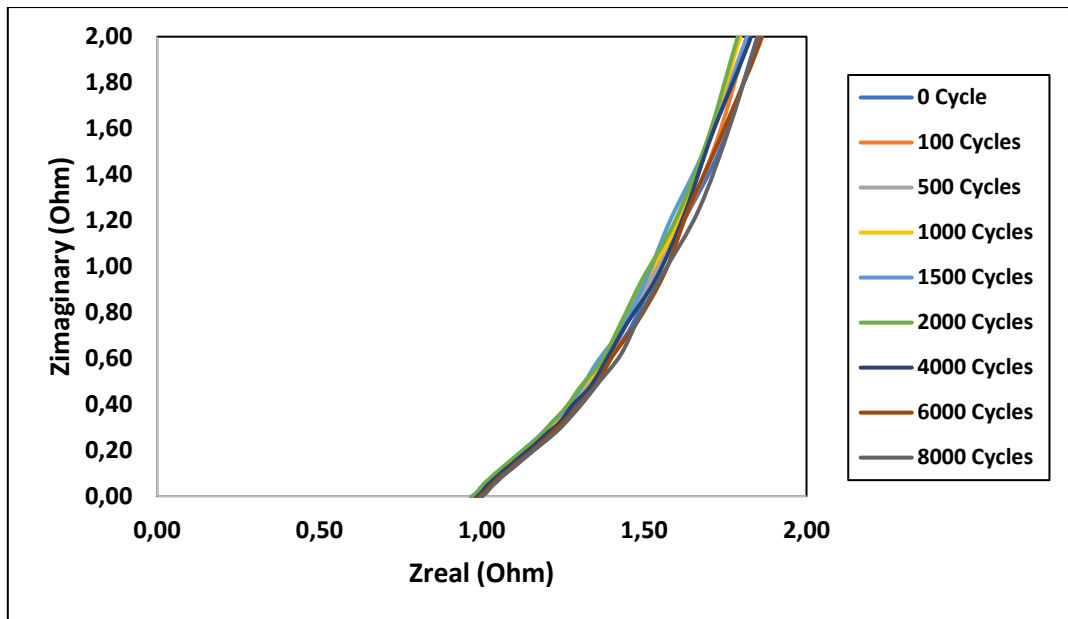
Figure B.15: Nyquist plots during AST of V40 ASDM half-MEA.

B.4. Capacitance plot
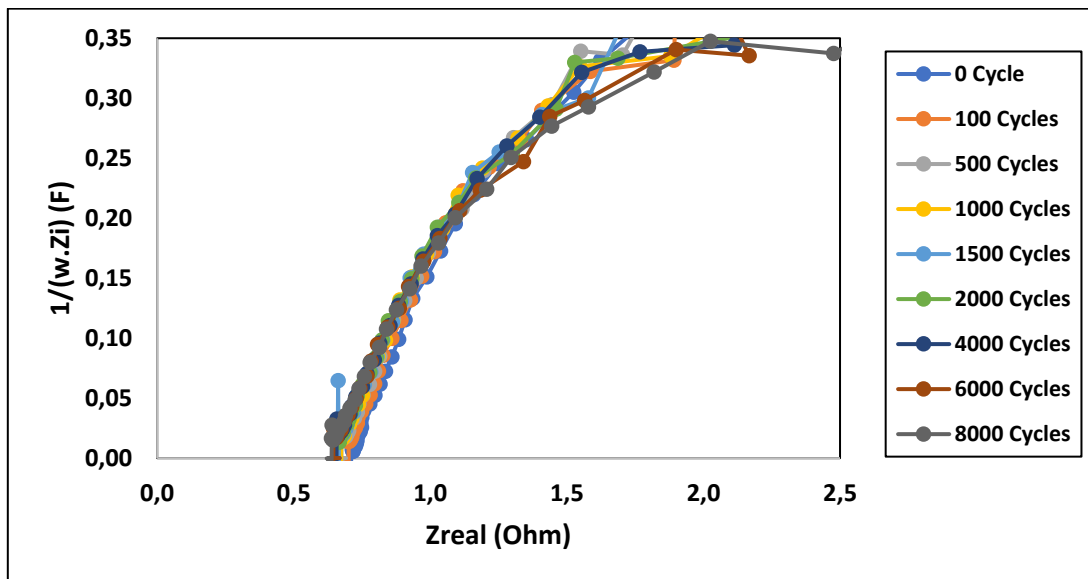
Figure B.16: Capacitance plots during AST in N_2 of GV40 NDM half-MEA.
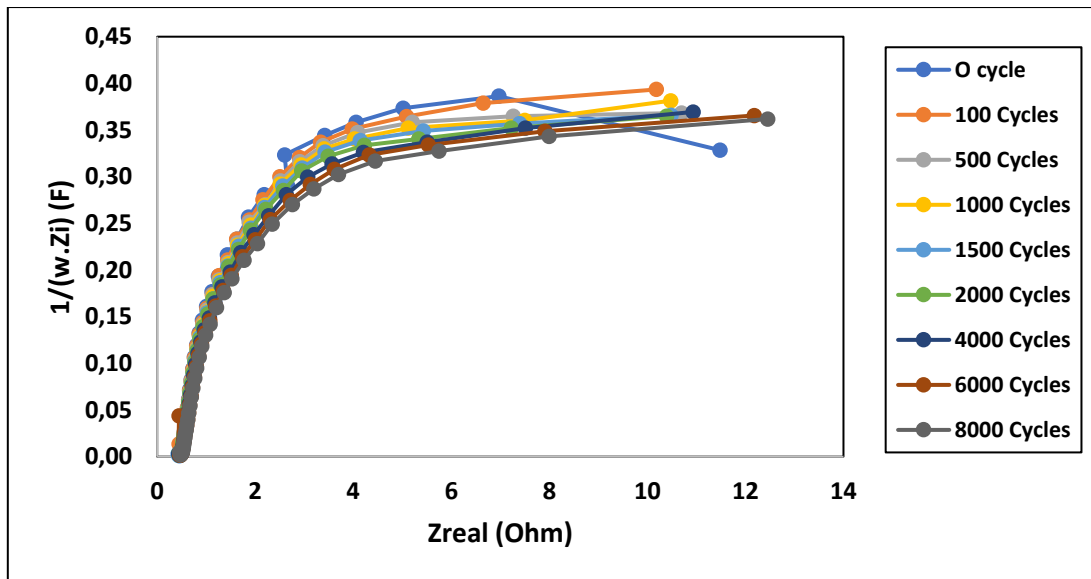
Figure B.17: Capacitance plots during AST in N$_2$ of GV40 ASDM half-MEA.
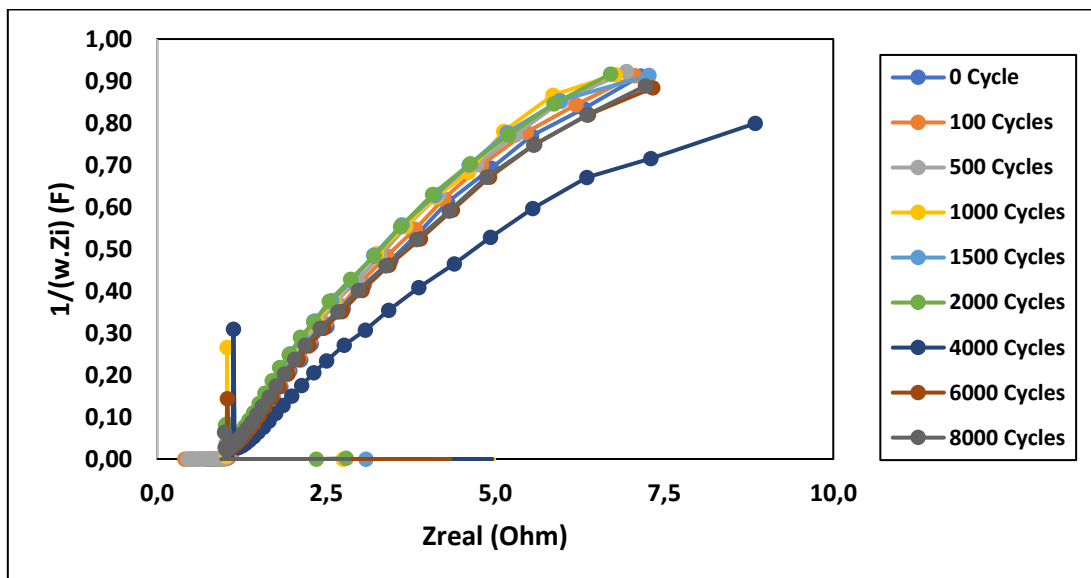
Figure B.18: Capacitance plots during AST in N$_2$ of V40 TDM half-MEA.
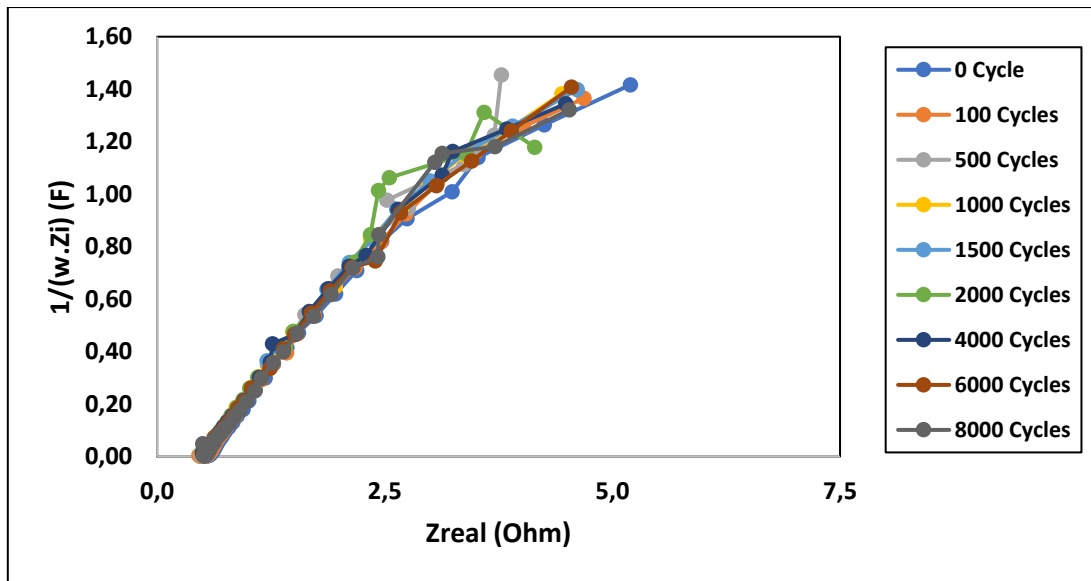
Figure B.19: Capacitance plots during AST in N$_2$ of V40 NDM half-MEA.
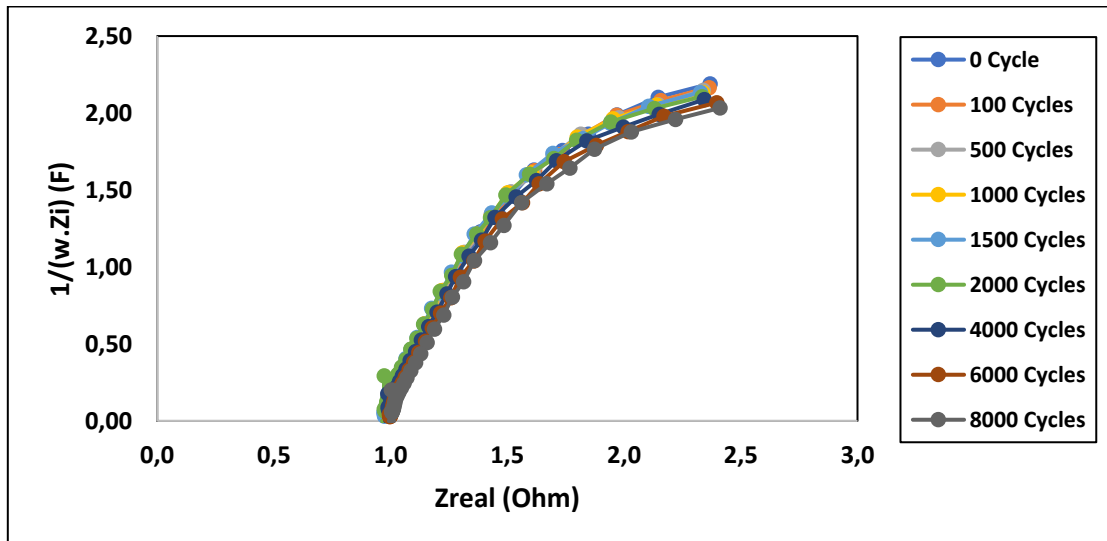
Figure B.20: Capacitance plots during AST in N$_2$ of V40 ASDM half-MEA.
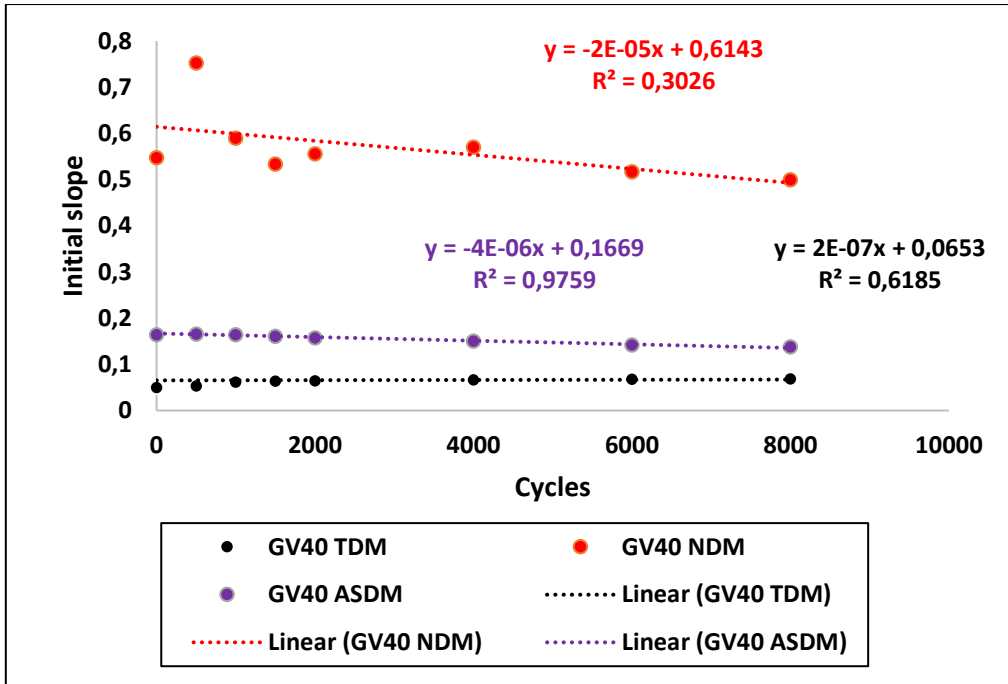
Figure B.21: Initial slopes of GV40 half-MEA capacitance plot as a function of stress cycles.
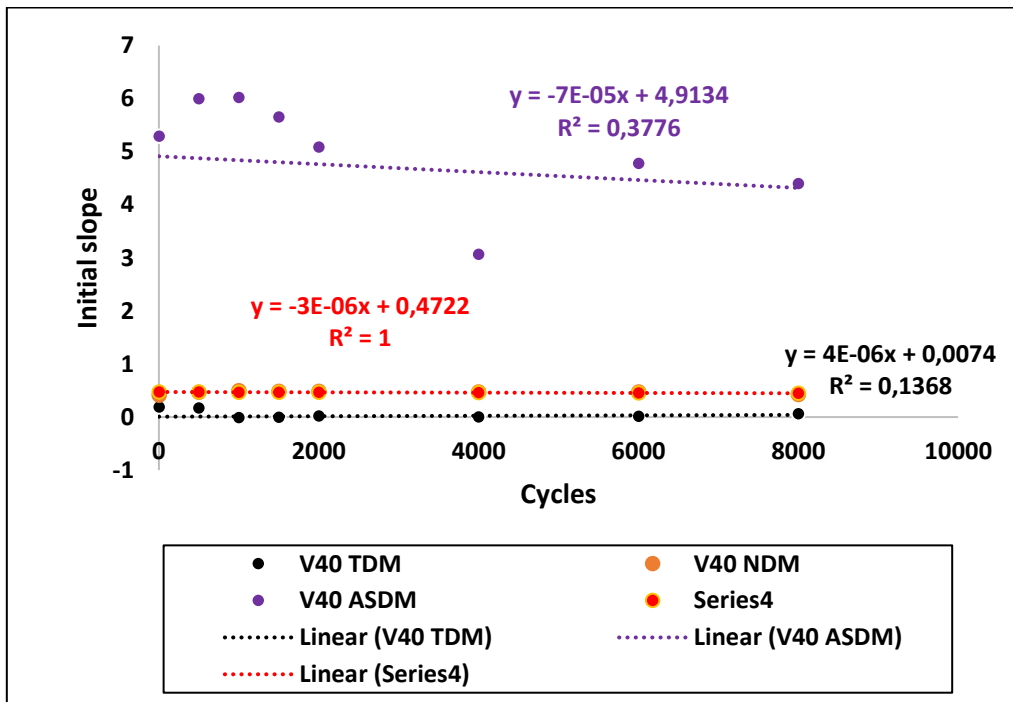
Figure B.22: Initial slopes of V40 half-MEA capacitance plot as a function of stress cycles.

C. Appendix C: Design of the half-MEA cell
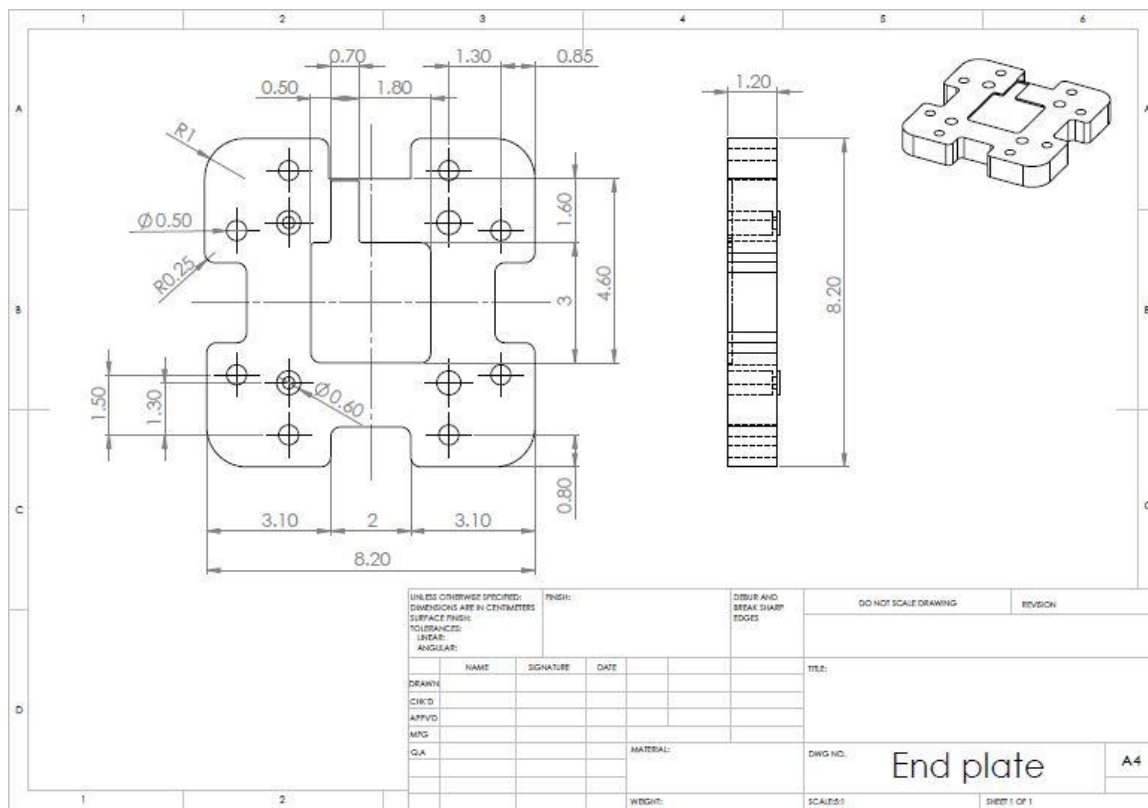
Figure C.1: End plate of the half-MEA cell.
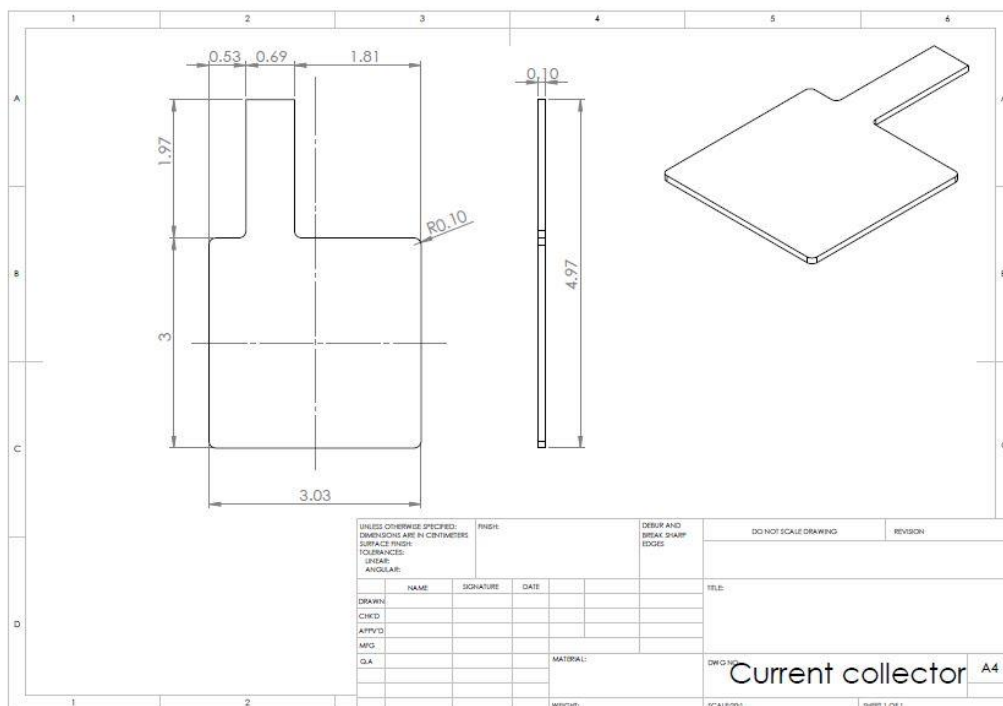
Figure C.2: Copper current collector.
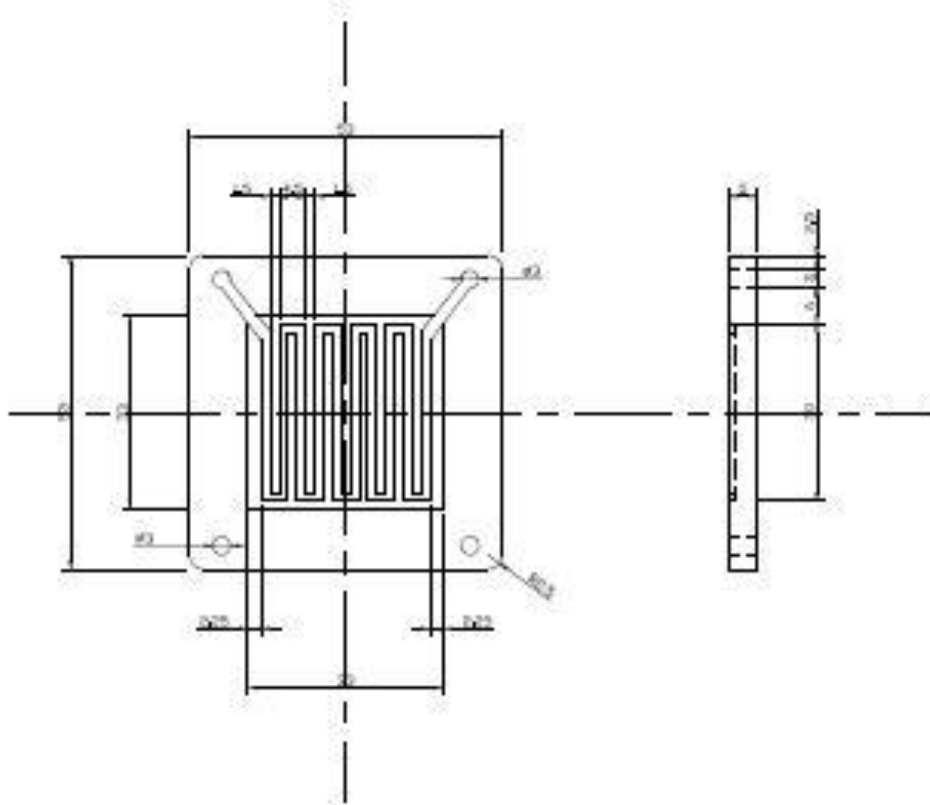
Figure C.3: Parallel flow field plate.
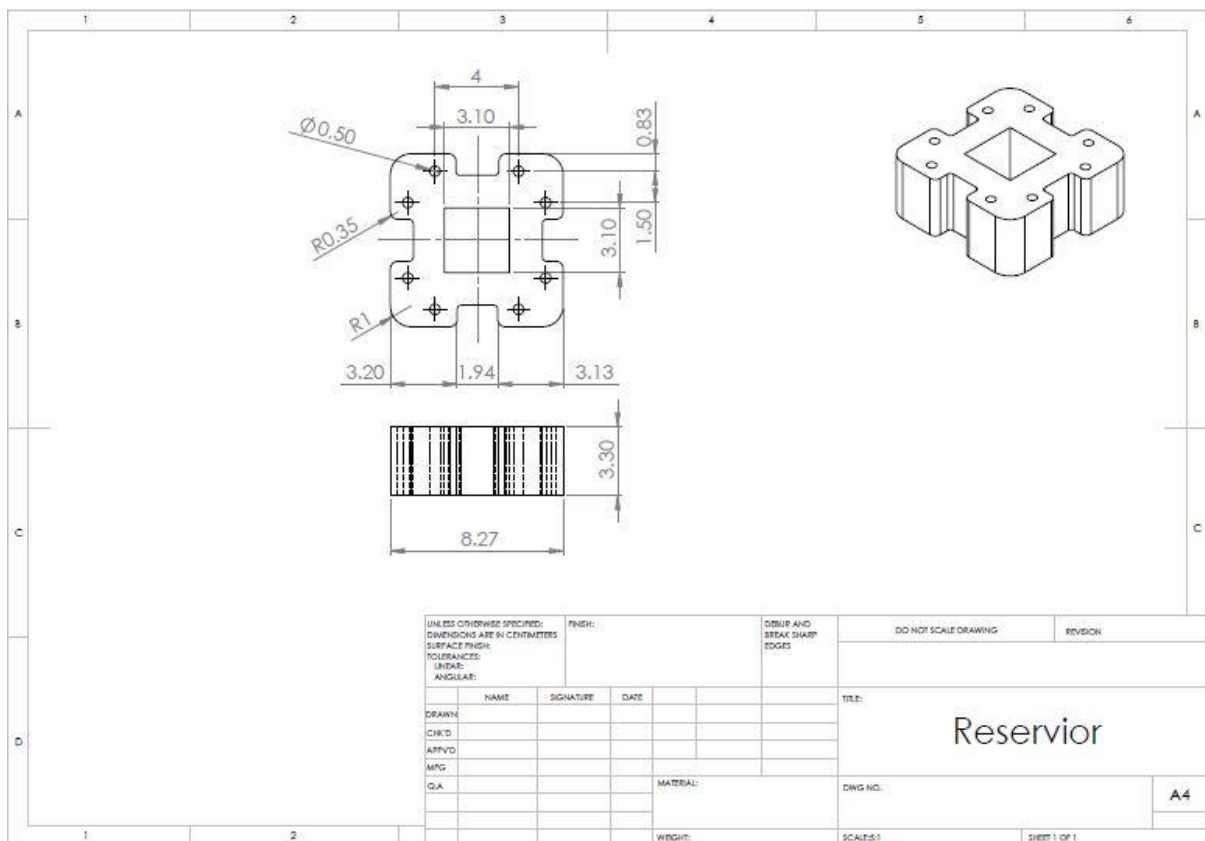
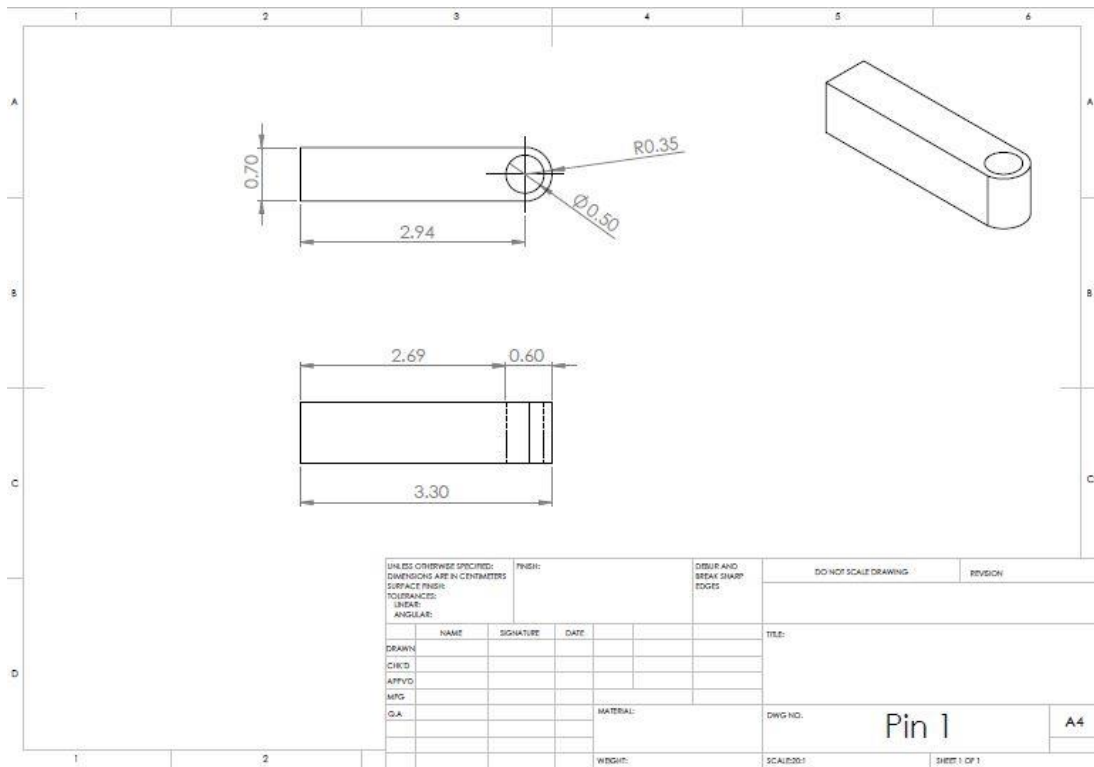*Figure C.4: Electrolyte pool or reservoir.*
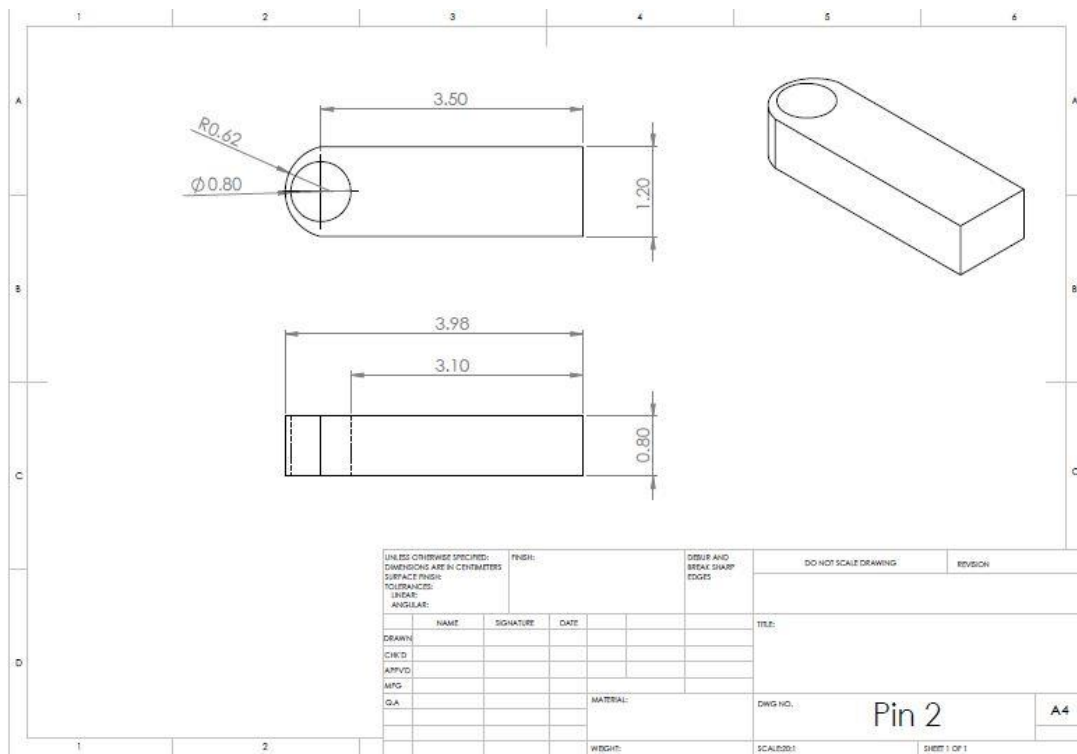
Figure C.5: Reference electrode holder.
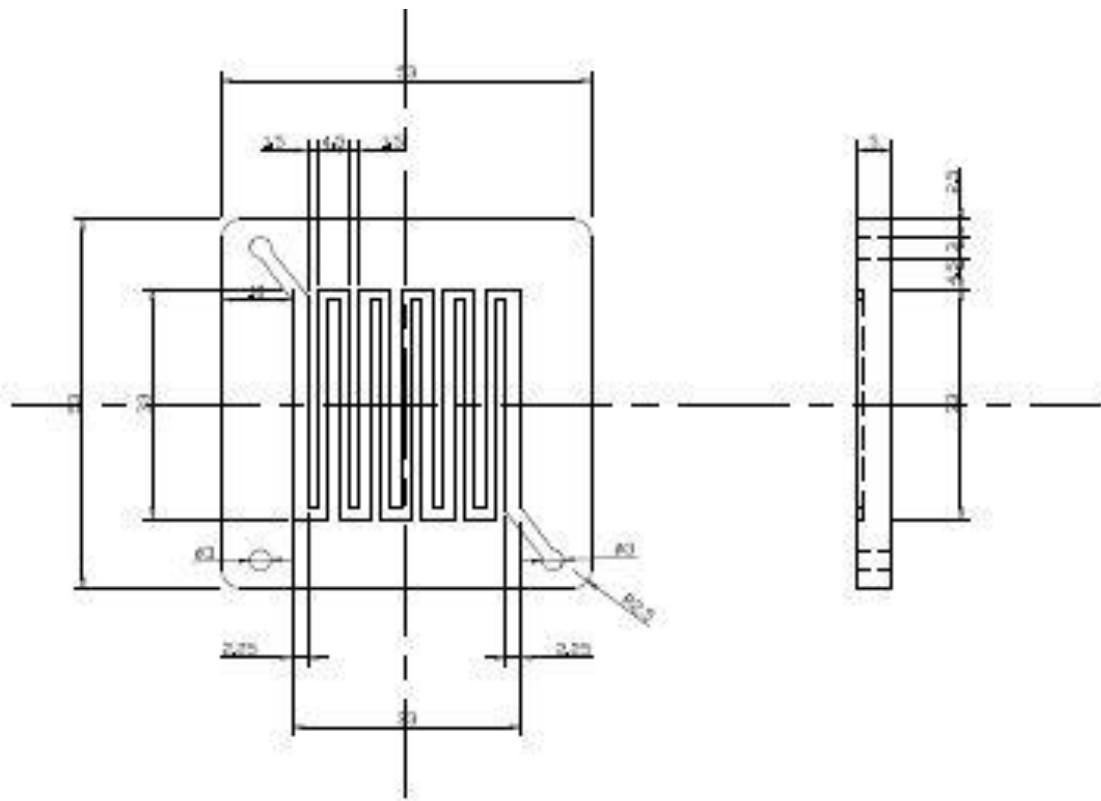

Figure C.6: Counter electrode holder.

Figure C.7: Recommended serpentine flow field plate.